# WAVE-EQUATION MIGRATION Q ANALYSIS

A DISSERTATION
SUBMITTED TO THE DEPARTMENT OF GEOPHYSICS
AND THE COMMITTEE ON GRADUATE STUDIES
OF STANFORD UNIVERSITY
IN PARTIAL FULFILLMENT OF THE REQUIREMENTS
FOR THE DEGREE OF
DOCTOR OF PHILOSOPHY

Yi Shen
December 2016

Printed as Stanford Exploration Project No. 166
by permission of the author

I certify that I have read this dissertation and that, in my opinion, it is fully adequate in scope and quality as a dissertation for the degree of Doctor of Philosophy.

(Biondo L. Biondi) Principal Adviser

I certify that I have read this dissertation and that, in my opinion, it is fully adequate in scope and quality as a dissertation for the degree of Doctor of Philosophy.

(Jon F. Claerbout)

I certify that I have read this dissertation and that, in my opinion, it is fully adequate in scope and quality as a dissertation for the degree of Doctor of Philosophy.

(Gary Mavko)

I certify that I have read this dissertation and that, in my opinion, it is fully adequate in scope and quality as a dissertation for the degree of Doctor of Philosophy.

(Robert Clapp)

Approved for the University Committee on Graduate Studies.

# Abstract

Quantitative estimates of quality factor Q are useful for a variety of applications, ranging from seismic-acquisition design, to seismic processing, amplitude analysis, and reservoir characterization. In my thesis, I mainly target to the attenuation caused by gas clouds/pockets, which is a notoriously challenging problem for reservoir identification and interpretation. The goal of my thesis is to understand and quantify the attenuation effects to create an accurate laterally- and vertically- varying attenuation model. Such estimates will be used to improve the image quality and provide greater confidence for hydrocarbon exploration.

Q model building, which is traditionally done in the data space using ray-based tomography, is a challenging problem due to issues like spectral interference, low signal-to-noise ratio, diffraction, and complex subsurface structure. I present an inversion based method, wave-equation migration Q analysis, to produce reliable Q models with two major features. First, this method will be performed in the image-space to stack out noise, focus and simplify events, and provide a direct link between the model perturbation and the image perturbation. Second, this method uses wave-equation-based Q tomography to handle the complex wave propagation. I develop both the Q migration and the Q tomographic operator using frequency-domain and time-domain visco-acoustic wave equations. Its numerical synthetic examples show that it works well for models with Q anomalies.

To improve the resolution of the Q model estimated by wave-equation migration Q analysis, I add a regularization term to the objective function based on the provided compressional velocity model. I derive an approximate closed-form solution relating the compressional velocity to compressional quality factor using rock physics modeling. This solution is validated using well data in which the elastic properties were measured and Q was derived numerically. I apply this relation between velocity and

Q to both synthetic and field seismic data, which produced an improved Q estimated model. I show that this improved Q model leads to a better seismic migration image.

Such developed methods require highly accurate velocity models. Therefore, I also develop a multi-parameter inversion of velocity and Q models using wave-equation migration analysis. This method poses the estimation problem as an optimization problem that seeks optimum velocity and Q models by minimizing user-defined image residuals. The numerical tests on a modified SEAM model with two gas clouds demonstrate the benefit of using such multi-parameter inversion, when the existing velocity and Q models are inaccurate. The results show that this inversion method is able to retrieve both velocity and Q models, and to correct and compensate the distorted migrated image caused by inaccurate velocity and Q models. I apply this joint inversion of velocity and Q models to the 3D Dolphin's multi-client field data acquired in the North Sea, which have attenuation and velocity problems due to shallow subsurface gas chimneys and channels that are correlated with strong attenuation and low-interval velocity. The updated velocity shows low velocity regions around the gas and channel features. The inverted Q model detects the shape and location of the gas and channel areas, which align with Dolphin's interpretation. Consequently, the migration with the updated velocity model and the estimated Q anomalies flattens the events in the subsurface angle gathers, enhances the damped amplitudes and the frequency content of the migrated events, corrects the distorted phase of the migrated events and makes them more coherent.

# Preface

The electronic version of this report[1] makes the included programs and applications available to the reader. The markings **ER**, **CR**, and **NR** are promises by the author about the reproducibility of each figure result. Reproducibility is a way of organizing computational research that allows both the author and the reader of a publication to verify the reported results. Reproducibility facilitates the transfer of knowledge within SEP and between SEP and its sponsors.

**ER** denotes Easily Reproducible and are the results of processing described in the paper. The author claims that you can reproduce such a figure from the programs, parameters, and makefiles included in the electronic document. The data must either be included in the electronic distribution, be easily available to all researchers (e.g., SEG-EAGE data sets), or be available in the SEP data library[2]. We assume you have a UNIX workstation with Fortran, Fortran90, C, X-Windows system and the software downloadable from our website (SEP makerules, SEPScons, SEPlib, and the SEP latex package), or other free software such as SU. Before the publication of the electronic document, someone other than the author tests the author's claim by destroying and rebuilding all ER figures. Some ER figures may not be reproducible by outsiders because they depend on data sets that are too large to distribute, or data that we do not have permission to redistribute but are in the SEP data library, or that the rules depend on commercial packages such as Matlab or Mathematica.

**CR** denotes Conditional Reproducibility. The author certifies that the commands are in place to reproduce the figure if certain resources are available. The primary reasons for the CR designation is that the processing requires 20 minutes

---

[1] http://sepwww.stanford.edu/public/docs/sep154

[2] http://sepwww.stanford.edu/public/docs/sepdatalib/toc_html/

or more.

**NR** denotes Non-Reproducible figures. SEP discourages authors from flagging their figures as NR except for figures that are used solely for motivation, comparison, or illustration of the theory, such as: artist drawings, scannings, or figures taken from SEP reports not by the authors or from non-SEP publications.

Our testing is currently limited to LINUX 2.6 (using the Intel Fortran90 compiler) and the SEPlib-6.4.6 distribution, but the code should be portable to other architectures. Reader's suggestions are welcome. For more information on reproducing SEP's electronic documents, please visit *http://sepwww.stanford.edu/research/redoc/*.

# Acknowledgments

It takes great efforts and many people's help for me during my 6 years at Stanford.

I am most grateful to Biondo Biondi, my adviser, not only for giving me the opportunity to be part of the unique research group, but also for giving me complete freedom to explore the research areas, and to try, to fail and eventually to be able to stand on my own feet. I appreciate his guidance, patience, and encouragement throughout the years. I am deeply grateful to Jon Claerbout. It was a privilege to work with him and learn from his genius mind. I thank Bob Clapp for his help with any difficulties and guidance through my own blindness to my problems. I thank Jack Dvorkin for being always available for discussions and for being supportive with his rock physics expertise. I thank my thesis committee member Gary Mavko for his well-taught lectures. I also thank Lexing Yin for chairing my defense.

I thank Sergio Grion, Gareth Williams, Shuki Ronen for their helps with the permission of using and publishing Dolphin's SHarp seismic data. I thank Dave Nichols for his discussion and suggestions on finding my PhD project. I thank my mentors during my internship Ali Tura, Bertram Nolte, Qie Zhang, Christopher Willacy and Vanessa Goh for their helps with my intern project. I especially thank Christopher Willacy and Vanessa Goh for their helps with the permission of publishing the GOM data.

Many aspects of my research were built on previous work by Yaxun Tang, Yunyue Li, Ali Almomin, Tieyuan Zhu. They are my mentors at Stanford. I thank Stewart A. Levin for his software tutoring and helps on the field data format conversion.

I am very fortunate to have shared office with some of the finest SEPers: Qiang Fu, Gboyega Ayeni, Adam Halpert, Yang Zhang, Guillaume Barnier and Alejandro Cabrales. I thank all the students arrived before and after me,Ohad Barak, Taylor

Dahlke, Huy Le, Eileen Martin, Guillaume Barnier,Gustavo Alves,Ettore Biondi,Alejandro Cabrales,Yinbin Ma, Joseph Jennings, Fantine Huot, Rahul Sarkar, Jason Chang, Stuart Farris, Musa Maharramov, Ali Almomin, Chris Leader, Zhang Yang, Xukai Shen, Mandy Wong, Yunyue Li,Adam Halpert, Sjoerd de Ridder, Qiang Fu, Gboyega Ayeni, Yaxun Tang, Kittinat Taweesintananon, Kaixi Ruan, Noha Farghal and Daniel Blatter for their discussion on the research and for being great friends and companions.

I owe special thanks to Alejandro Cabrales and Eileen Martin who did a great job proof-reading my dissertation and improving it significantly.

I am grateful to the geophysics staff for their excellent support. Specifically, Diane Lau, Claudia Baroni and Liliane Pereira ensured SEP meetings, travels, and research needs are taken care of promptly. Tara Ilich, Nancy Massarweh and Rachael Madison, the Student Services Manager, made sure all my questions about departmental requirements answered timely. Dennis Michael, Manager of CEES HPTC, provided superb technical support and HPC training during my use of the clusters.

I thank my undergraduate thesis advisers, Xinlong Wang for supporting and encouraging me to learning and researching seismic exploration.

I thank my dear friends at Stanford: Xiaochen Wang, Yi Wu, Jingyi Chen, Crystal Shi, Shang Deng, Yixuan Wang, Yu Xia, Yao Tong, Cheng Cheng, Likang Sun, Yi Yang, Shaoyu Lv, Tianze Liu, Chao Liang, Dongzhuo Li, Shaochuan Xu, Yixiao Sheng, Weiqiang Zhu, Yunfei Yang, Zhipeng Qin, Xin Liu, Wenyue Sun, Guang Yang, Senyuan Jiang, Chuan Tian, Beibei Wang, Peipei Li, Yueru Hao, Wenhuan Kuang, Lei Jin, Yihe Huang, Yongxin Gao, Yujie Zheng, Yao Li, Xirui Xiao, Shengtong Chen, Yanyang Kong, Daisy You for spending our most beautiful youth together.

I thank my long time dear friends: Lan Bao, Liyuan He, Siliang Kang, Tiantian Xu, Yi Wang, Wanyan Sun, Xiangyi Feng, Jianghong Shi, Chencheng Sun, Min Xu, Ailing Song, Jun Qang, Fang Dong, Yin Liu for constantly nurturing me from my roots and reminding me that there is home to return.

Finally, I would like to thank my parents Xiaohong Xu and Guoliang Shen for their unconditional support and love throughout my time at Stanford. I am utterly lucky to have found my husband, Xukai Shen, for his caring and love. The man showed me the real happiness in life.

# Contents

# List of Tables

# List of Figures

# Chapter 1

# Introduction

Seismic attenuation, parametrized by the seismic quality factor, Q, has considerable impacts on surface seismic reflection data. Attenuation decreases the amplitude of a traveling wave, as well as lowing its resolution, distorting its phase and dispersing its velocity. Figure 1.1(a) compares a nonattenuated wave (blue) and an attenuated wave (red) propagating though an medium with Q = 30. Both waves are recorded at the same time. Figure 1.1(a) shows the amplitudes dropped in the attenuated wave are significant. Because the attenuation causes velocity dispersion, the higher frequency travels faster than the lower frequency. Therefore, these two wavelets have different arrival times, and the attenuated wave has a phase change to which the shape of wavelet changes and becomes nonsymmetric. Their spectra are plotted in Figure 2.1(b). The red and blue curves in Figure 2.1(b) are the amplitude spectra of the waves shown by red and blue in Figure 1.1(a), respectively. Figure 2.1(b) shows that attenuation largely dampens the higher frequencies of a wave more than its lower frequencies. In fact, the large amplitude decay at the higher frequencies results in such significant drops in amplitude in Figure 1.1(a).

Migrating seismic data without Q compensation produces a seismic image distorted by attenuation in a same way. Attenuation degrades the seismic image quality by decaying the higher frequency of the image and distorting the phase of events. Figure 1.2(a) is the migrated image with a correct Q compensation. The image shows the events are imaged at an 800 m depth with symmetric wavelets. Figure 1.2(b) is the migrated image without Q compensation. The image shows the events are

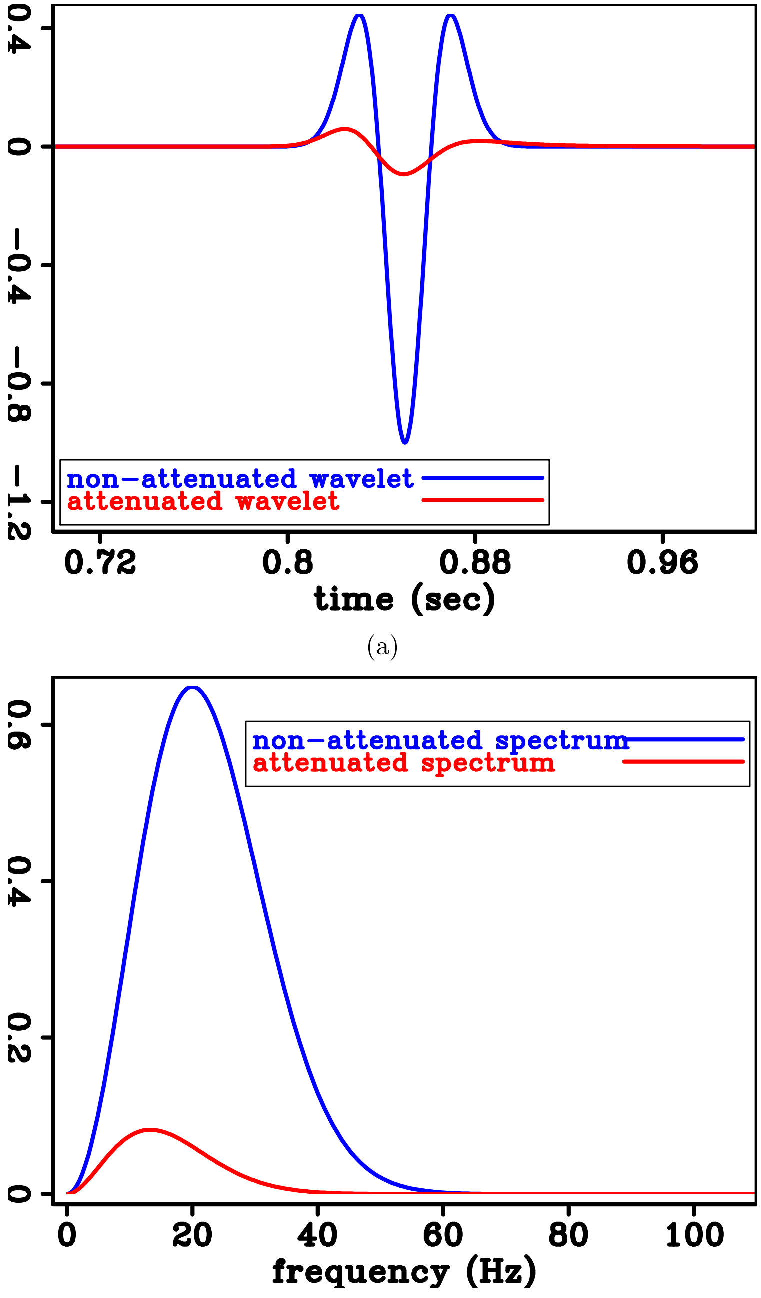

(a)

(b)

Figure 1.1: 1D example to numerically illustrate the attenuation impacts on the amplitudes spectra and phase of a propagating wave: (a) the blue curve shows a non-attenuated wave and the red curve shows a wave propagating through an attenuating medium with $Q = 30$. Both waves are recorded at the same time. The reference frequency is 15 Hz.(b) The amplitude spectra of the waves in Figure 1.1(a). [**ER**] chap1/. Intro.wave,Intro.spex

imaged shallower than an 800 m depth with nonsymmetric wavelets, because attenuation makes the velocity at the higher frequencies travel faster, and such dispersed velocity has not been corrected. Also the amplitudes of the higher frequencies are attenuated for the wavelets in Figure 1.2(b) to be stretched thereby making their root mean square amplitudes 11 times smaller than the wavelets in Figure 1.2(a). These problems impede accurate image interpretation for hydrocarbon production and well positioning.

In my thesis, I mainly target to the attenuation caused by clouds/pockets, which is a notoriously challenging problem for reservoir identification and interpretation. Gas clouds/pockets usually have attenuation with extremely low Q value. Such strong attenuation reduces the amplitude and phase of deeper events, and essentially creates a shadow zone over the reservoirs, which limits accurate reservoir interpretation. For example, the brightness of the events in the seismic image are well correlated with the fluid content in the reservoir sand. However, the attenuated amplitude brings ambiguity to the fluid identification and causes errors in mapping the reservoir region. Therefore it is valuable to understand and quantify the attenuation effects to create an accurate laterally- and vertically- varying attenuation model.

Such estimates could be used to improve the image quality, and to better interpret the effects of amplitude versus offset (AVO) and anisotropy that have offset-dependent signatures. Such improvements provide greater confidence for hydrocarbon exploration. In addition, the estimated Q model could be a useful parameter for characterizing rock and fluid properties because of its high sensitivity to some of these properties (e.g. Best et al. (1994)). For example, the estimated Q model can serve as a lithology discriminator in a frontier area with sparse well control (Dasgupta and Clark, 1998). Furthermore, because the magnitude of the attenuation is directly related to petrophysical parameters, the Q analysis provides a potential tool for reservoir characterization; it can help determine the contents (e.g., gas saturation) of a reservoir (Winkler and Nur, 1982), map fracture azimuth to target reservoir development (Clark et al., 2001; Maultzsch et al., 2007; Clark et al., 2009), and monitor the mobility of reservoir fluids to optimize the injection process (Macrides and Kanasewich, 1987).

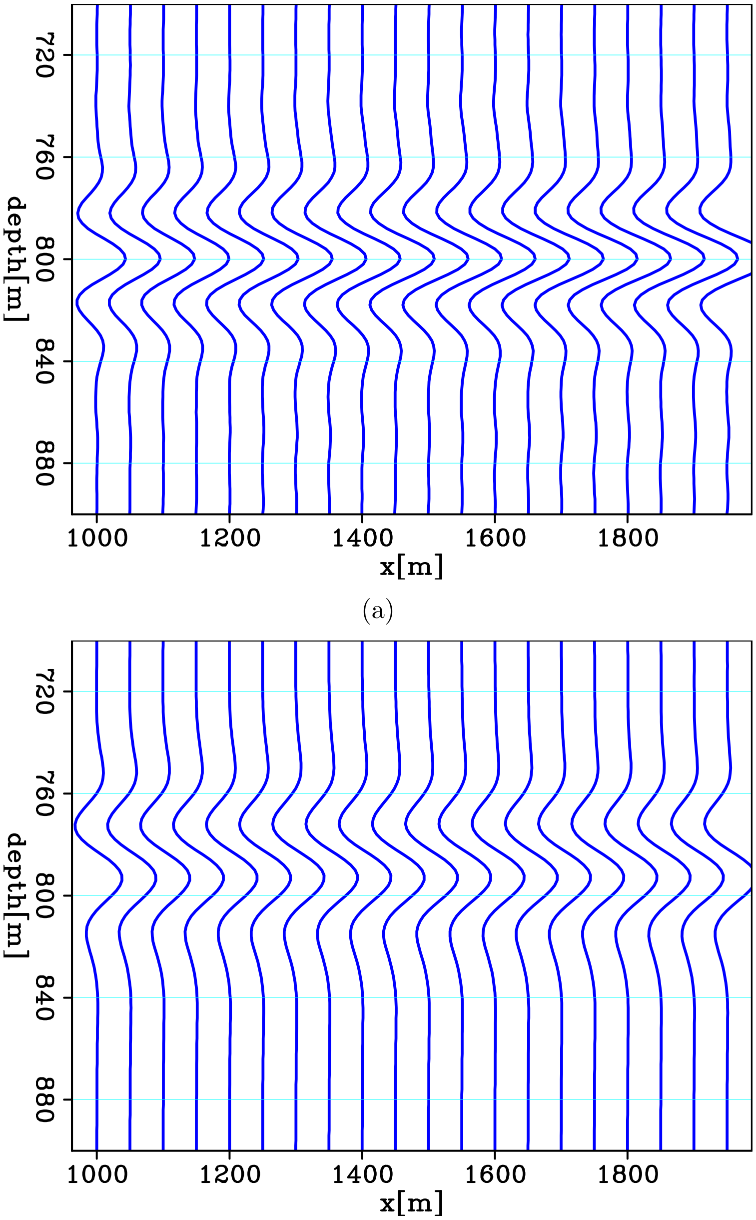

(a)

(b)

Figure 1.2: (a) The migrated image with a correct Q compensation. (b) The migrated image without Q compensation. The source wavelet is a Ricker wavelet with frequency band of 0-50 Hz. The reference frequency is 15 Hz. [**ER**] chap1/. syn.bimg.ref,syn.bimg.att

### Intrinsic attenuation and scattering attenuation

Seismic attenuation includes intrinsic attenuation and the scattering attenuation. Both can cause wave dispersion and amplitude decay. Intrinsic attenuation is caused by anelastic processes or internal friction, which transfer wave energy to heat and results to energy loss of a propagating wave. The intensity of intrinsic attenuation is given by the frictional energy loss per cycle as follows:

$$\frac{1}{Q_i} = -\frac{\Delta E}{2\pi E}, \tag{1.1}$$

where $E$ is the total energy, $\Delta E$ is the energy loss per cycle, and $Q_i$ is the intrinsic quality factor.

Scattering attenuation is caused by heterogeneties distributed in the earth and transfer wave energy to later arrivals or other directions. Scattering attenuation depends on the scale of heterogeneties. If the scale of the heterogeneties is much larger than the wavelength, the ray theory is valid in wave propagation, and the reflected wave by the interface in the subsurface can be recorded by the receivers; while if the scale of the heterogeneties is small and comparable to the wavelength, the waves are scattered around and not necessarily recorded by the receiver. Therefore, the high-frequency components are lost because of destructive interference. Such scattering by the small-scale heterogeneties is parametrized by the quality factor $Q_s$. However, scattering attenuation still makes the integrated energy in the whole wavefield constant.

In my thesis, the estimated attenuation is a combination of the intrinsic attenuation and the scattering attenuation caused by small-scale heterogeneties. The quality factor quantifying the total attenuation Q is expressed as follows:

$$\frac{1}{Q} = \frac{1}{Q_i} + \frac{1}{Q_s} \tag{1.2}$$

## Q MODEL BUILDING

Studies estimating attenuation tomographically have a long history. Brzostowski and McMechan (1992), and Leggett et al. (1992) used the change in seismic amplitude as observed data for attenuation tomography. Kjartansson (1979), and Zucca et al. (1994) measured the rise time of the broadened wavelets caused by attenuation for the Q tomography. Tonn (1991), Quan and Harris (1997), Dasgupta and Clark (1998), Leaney (1999), Mateeva (2003), Plessix (2006), Rickett (2006), Rickett (2007), Reine et al. (2012a), and Reine et al. (2012b) performed the estimation based on the attenuation-induced spectral changes. The Q estimation schemes in these works have two major features: primarily ray-based tomography and measuring Q effects in the data domain. However, these two features have their limitations in an accurate Q estimation subsequently described. Therefore, I propose a new technique using image-space wave-equation tomography to produce a reliable Q model. I call this method wave-equation migration Q analysis (WEMQA), of which the idea is similar to wave-equation migration velocity analysis (WEMVA) (Sava and Biondi, 2004; Biondi, 2006) that relates image perturbation with velocity perturbation.

## Image domain or data domain

The measurements conducted in the data domain have a number of issues that can affect the accuracy of Q model building. First, diffractions and a poor signal-to-noise ratio introduce large errors in the Q estimation. Second, spectral analysis is in the Q estimation methods for Q effects measurements. However, it is difficult to compute the spectra of the individual/multiple events in prestack data, because the events are close or even crossed at far offsets. Even the events in the data domain generated by a simple model with three reflectors are crossed (Figure 1.3(a)), which introduces spectral interference.

However, the image-space method is less prone to the issues mentioned previously. First, stacking employed by migration suppresses the noise and makes a cleaner event for spectral analysis. Also, migration focuses and simplifies the events. For example, the crossing events in the data space (Figure 1.3(a)) are separated in the image space (Figure 1.3(b)), which avoids spectral interference and improves the accuracy of computing the events spectra. In addition, the migration-based technique could be more efficient than the data-based one, because it can be implemented in a target-oriented fashion (Tang, 2011) and therefore focus on the region of interests.

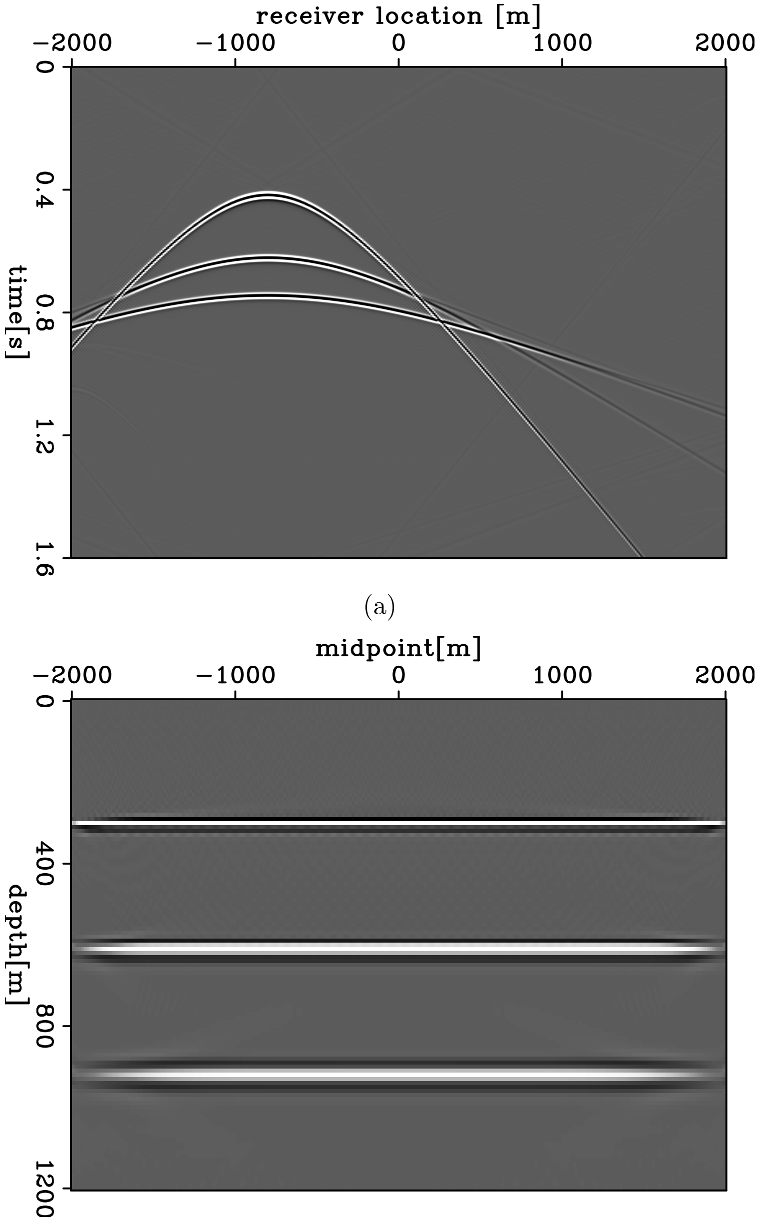

(a)

(b)

Figure 1.3: a) The events around t=0.8s are crossed in the prestack data domain; and (b) the crossing events shown in Figure 1.3(a) are separated. The x-axis is the midpoints. [**ER**] chap1/. crs.trec,crs.img

## Ray-based or wave-equation-based tomography

Ray-based tomography used in the Q work (Kjartansson, 1979; Tonn, 1991; Brzostowski and McMechan, 1992; Leggett et al., 1992; Zucca et al., 1994; Quan and Harris, 1997; Dasgupta and Clark, 1998; Leaney, 1999; Mateeva, 2003; Plessix, 2006; Rickett, 2006, 2007; Reine et al., 2012a,b) relates the Q model perturbation to the attenuation-induced spectral change of the recorded events. A ray-based method has its advantages of computational efficiency, and works well in simple geology settings with gentle horizontal variations in the subsurface. However, a ray-based method is prone to errors and unrealistic results when multi-pathing exists in areas of complex overburden. The wave-equation-based tomography is able to handle multi-pathing. Figure 1.4(a) displays a snapshot of the traced rays and Figure 1.4(b) displays a snapshot of the wavefields. The figures show that the ray-tracing method over-simplifies the wavefront of the wave reflected by the complicated salt boundary; while the wave-equation-based method well represents the wave propagation and captures the multi-pathing.

Therefore, I propose the WEMQA method to overcome the limitations of the previous work. This method computes the effect of attenuation from a migrated image. Then WEMQA provides a direct mapping between the change in the image space and the change in the Q model using wave-equation based tomography. These works have been already presented in (Shen et al., 2013, 2014; Shen and Zhu, 2015; Shen et al., 2015; Shen* et al., 2015; Li et al., 2015; Shen and Dvorkin, 2015, 2016).

# OVERVIEW OF THESIS

## Wave-equation migration Q analysis

In Chapter 2, I present an inversion-based method, wave-equation migration Q analysis (WEMQA), to estimate Q models from migrated images by a wave-equation tomographic operator. I first introduced its objective function that requires computing a migrated image with Q compensation. Then I derived the gradient of the objective. I developed both the Q migration and the Q tomographic operator using one-way and two-way visco-acoustic wave equations. Finally, I applied WEMQA to three synthetic examples to demonstrate the capability of this method to estimate

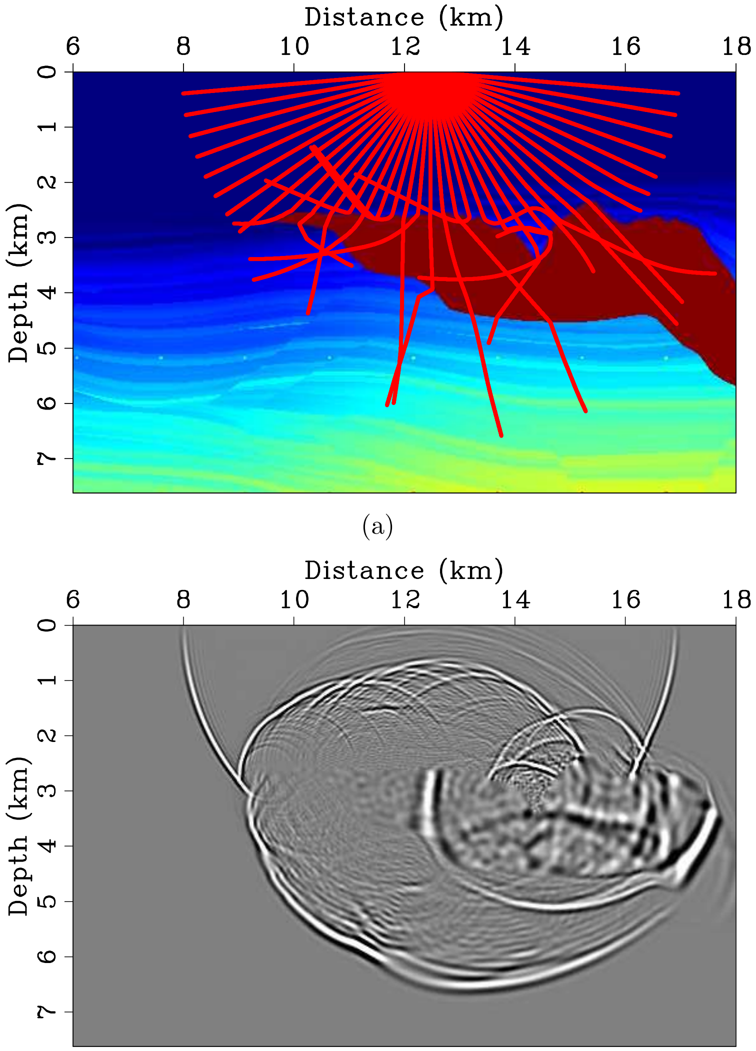

(a)

(b)

Figure 1.4: (a) A snapshot of the traced rays overlaid by the Sigsbee2A velocity model; and (b) a snapshot of the wavefields. Courtesy of Tang (2011). [**NR**] chap1/. crs.ray,crs.wave

subsurface models with Q anomalies.

## Rock physics constrained WEMQA

Chapter 2 shows that WEMQA is able to estimate compressional attenuation anomalies, but the inversion results have a low resolution. In Chapter 3, I improved the resolution of the inverted Q model by adding a regularization term to the objective function based on the provided compressional velocity model ($V_p$). I defined $Q_p$ as the compressional quality factor in this chapter, which is the same as the variable $Q$ defined in Chapter 2.

It has been observed from field data (He and Cai, 2012; Zhou et al., 2014) that strong compressional attenuation often accompanies low compressional velocity. However, very few studies have analytically linked these two properties. Rock physics has built several models (Dvorkin et al., 2014; Muller et al., 2010) of $V_p$ and $Q_p$ based on other rock properties (e.g., porosity, saturation, and mineralogy), which may implicitly quantify the relation between these two parameters. However, these existing models for $V_p$ and $Q_p$, based on rock physics properties, only provide an estimate of these two parameters at the well. A model that provides an analytic relation between $V_p$ and $Q_p$ would allow us to approximately relate $Q_p$ to $V_p$ without going through direct rock physics modeling, which would not be constrained by location. Such a relation can be used as the constraint/regularization term in the seismic inversion and in turn would improve the accuracy of the seismic inversion of $V_p$ and $Q_p$.

In Chapter 3 , I first derived an approximate closed-form solution directly relating $V_p$ to $Q_p$ using rock physics modeling. Next, I validated this relation using field well data. Finally, I applied this new $Q_p$-$V_p$ equation to synthetic seismic data, resulting in an improved $Q_p$ model. I used this approach to improve the $Q_p$ model as well as seismic imaging using field seismic data.

## Multi-parameter inversion of velocity and Q using wave-equation migration analysis

In Chapter 2 I develop wave-equation migration Q analysis (WEMQA), to produce a reliable Q model. This method analyzes attenuation effects from the seismic image migrated with the current velocity and Q models. In Chapter 3 I present an approximate closed-form solution directly relating velocity to Q for compressional wave that can be used as a constraint term in WEMQA to improve the accuracy of the seismic inversion of the Q model. Both methods require highly accurate velocity models. An inaccurate velocity model used by WEMQA distorts the spectra of the migrated events and causes errors in spectral analysis for estimating the attenuation effects. In addition, the seismic inversion constrained by an inaccurate velocity model degrades the accuracy of the inverted Q model. Therefore, joint inversion of both velocity and Q models becomes mandatory if neither of these models is correct.

In Chapter 4, I developed a method for multi-parameter inversion of velocity and Q models using wave-equation migration analysis. Then I tested this method on a synthetic dataset to demonstrate its benefit and effectiveness. I applied this method to the field data examples in Chapter 5.

## Field data application

The Dolphin Geophysicals (Dolphin) multi-client field data acquired in the North Sea (CNS data) used in this study has attenuation problems. The area was under the influence of salt tectonics, producing two diapirs. Dolphin interpreted a gas chimney above one diapir, and a channel above the other. The gas chimney forms a migration pathway for the gas to leak and then accumulate at the shallow position. The shallow gas gives rise to strong attenuation and low interval velocities in the the area where it is present. The channel also has low interval velocities, and is a strongly attenuating region. These complexities reduce the amplitudes and distort the phases of deeper events, and essentially create a shadow zone over the salt body and over the potential reservoir target area, thus hampering accurate reservoir interpretation. Therefore, it is important to build a velocity model as accurately as possible. It is also valuable to understand and quantify the effects of the attenuation anomalies to create an accurate laterally- and vertically- varying attenuation model.

Using the velocity model provided by Dolphin, I migrated the data. As a quality control measure I calculated angle domain common image gathers. These gathers showed downward curving events, indicating that the initial velocity model was too fast. Furthermore, both the migrated image and the angle gathers show that the events below the interpreted shallow gas and channel regions are wiped out because of attenuation, which will be described in more detail later in chapter. The objective of my study is to update the provided velocity model, especially in the gas and channel regions, and invert for the Q model to recover these two anomalies. In this way, the improvements in image quality using the derived model provide greater confidence for hydrocarbon exploration.

In Chapter 5, I first gave an overview of these field data. Second, I present my preprocessing workflow including coordinates manipulation, the removal the noise, multiples, bubbles and ghosts. Third, I applied wave-equation migration Q analysis (WEMQA) as described in Chapter 2 combined with wave-equation migration velocity analysis (WEMVA) (Biondi and Sava, 1999; Clapp and Biondi, 2000; Biondi and Symes, 2004) to update the current velocity model and invert for the Q model to recover the Q anomalies. In the third part, I used the workflow proposed in Chapter 4 to sequentially estimate a 3D velocity and Q models, and used the estimates in 3D migration with compensation to improve the image quality.

# Chapter 2

# Wave-equation migration Q analysis

In this chapter, I present an inversion-based method, wave-equation migration Q analysis (WEMQA), to estimate the seismic quality factor, Q, from migrated images by a wave-equation tomographic operator. I first introduce its objective function that requires computing a migrated image with Q compensation. Then I derive the gradient of the objective function. I developed both the Q migration and the Q tomographic operator using one-way and two-way visco-acoustic wave equations. Finally, I apply WEMQA to three synthetic examples to demonstrate the capability of this method to estimate subsurface models with Q anomalies.

## PROBLEM SETUP

Seismic waves are attenuated as they travel through the Earth. Migrating seismic data without Q compensation produces a seismic image distorted by attenuation. Attenuation damps the amplitudes of the events in the migrated image, especially at higher frequencies, and causes phase dispersion. Theoretically, migration with an accurate Q model is able to compensate for the effect of attenuation (i.e., effect of Q) on seismic images. On the contrary, migration using an inaccurate Q model cannot adequately correct such distortions. In order to evaluate the accuracy of a Q model I use a parameter $\rho$ to quantify its effect on the resulting migrated image. I will fully describe the definition and calculation of $\rho$ later in this section. I will show later that this parameter $\rho$ is a good indicator of the accuracy of the current Q model in the sense that the larger the absolute value of $\rho$ is, the larger the Q effects are measured from the seismic image, and thus the farther the current Q model is from the accurate Q model (and vice-versa). Therefore, we seek to minimize the L2-norm of the following objective function

$$J = \frac{1}{2} \sum_{\mathbf{x}} \left| \rho\left(\mathbf{x}; Q\right) \right|^2, \tag{2.1}$$

where $\mathbf{x}$ is each a spatial location in the image space, and $Q$ is the current model for quality factor.

It takes two steps to calculate the objective function in Equation 2.1. The first step is to generate a seismic image by migration with the current Q model. The second step is to compute the parameter $\rho$ from this seismic image. In the following part of this section, I will first present the algorithm for Q compensation through migration. Then I will describe the definition of parameter $\rho$ and illustrate the way to compute it.

## Step 1: migration with Q compensation

Migration with Q compensation aims to recover the attenuated amplitudes and to correct the distorted phases in the migrated image. In order to appropriately handle complex structures, e.g., salt bodies, I use wavefield continuation migration based on the visco-acoustic wave equation to compensate for these Q effects.

In general, wavefield continuation can be implemented using one-way downward continuation or time-domain wavefield propagation (i.e. reverse time migration). The one-way method has the advantage of cheap computational cost when compared with the time-domain method. However, the one-way method has limited ability to represent the actual wave propagation around steep structures, because propagating the wavefield along only one direction of the depth axis cannot properly deal with overturned events (e.g. salt flanks and prismatic waves). In principle, time-domain wavefield propagation is capable of modeling these overturned events. In the following, I will describe how to perform migration with Q compensation using these two different types of wavefield continuation. I show their implementation in numerical examples of both synthetic data and field data in this chapter and chapter 5.

### One-way migration with Q compensation

In an attenuating medium, one-way migration propagates the wave either upward or downward using the one-way frequency-domain visco-acoustic equation. Different Q models (Kolsky, 1953; Zener, 1948; Kjartansson, 1979) assume different trends in the variation of Q over a range of frequencies., and hence lead to the formulation of different visco-acoustic equations. Attenuation is considered to be almost linear with frequency - meaning Q is constant - in seismic frequency bands (Aki and Richards, 1990; McDonal et al., 1958). Therefore, I use a nearly constant-Q model (Futterman, 1962) in my study to approximate seismic attenuation in seismic migration, which assumes Q is almost independent of frequency. The one-way visco-acoustic equation based on this assumption proposed by (Futterman, 1962) has the same form as the one-way acoustic equation. However, the slowness (inverse of phase velocity) in the visco-acoustic equation becomes a complex number, as follows:

$$\tilde{s}(\omega) = s_{\omega r}\left(1 - \frac{1}{\pi Q}\ln(\omega/\omega_r)\right)\left(1 + \frac{i}{2Q}\right), \tag{2.2}$$

where $s_{\omega r}$ is the slowness at a reference frequency $\omega_r$, which is equivalent to the acoustic slowness in a non-attenuating media. Industrial practice has different criteria for selecting $\omega_r$. The most common practices are choosing the central frequency or the high frequency (Nyquist frequency). I chose the central frequency in my study, because it dominates the frequency band of interest for the surveys I am interested in.

In Equation 2.2, the imaginary part of the visco-acoustic slowness is the multiplication of the acoustic slowness by a factor of $\frac{i}{2Q}$. This factor represents a decay in the amplitude of the wave. The real part of the visco-acoustic slowness $s_{\omega r}\left(1 - \frac{1}{\pi Q}\ln(\omega/\omega_r)\right)$ becomes a dispersive term effectively causing low frequencies of a wave to travel slower than its high frequencies.

To forward model the wavefield in an attenuating medium, I downward continue the wavefield based on the following recursive solution:

$$P_{z+\Delta z}\left(\omega, k_x, k_y\right) = P_z\left(\omega, k_x, k_y\right) e^{\pm i k_z \Delta z}, \tag{2.3}$$

where $P$ is the pressure, $\omega$ is the temporal frequency, $k_x$ and $k_y$ are the horizontal wavenumbers. The plus and minus signs in the phase-shift operator represent downgoing and upgoing waves, respectively. $k_z$ is the vertical wavenumber, often referred to as the Single Square Root (SSR) operator, and can be expressed as follows:

$$k_z = \sqrt{(\omega \tilde{s})^2 - |\mathbf{k}|^2}, \tag{2.4}$$

where $|\mathbf{k}| = \sqrt{k_x^2 + k_y^2}$. In Equation 2.4, the multiplication of the visco-acoustic slowness with the temporal frequencies increases the attenuation-induced amplitude decaying effect at high frequency, and hence attenuates the higher frequencies of a wave more than its lower frequencies. Being part of the argument of the complex exponential function in Equation 2.3, the imaginary part of the SSR damps the wave amplitude exponentially along its wavepath.

The backwards propagation in migration is the adjoint of the forward propagation. By definition, the adjoint operator is the conjugate transpose of the forward operator, as a result, it reverses the sign of the real part of the forward operator, but keeps the sign of the imaginary part unchanged. Therefore, the backwards propagation in migration reverses the sign of the real part of the SSR in Equation 2.3, but keeps the sign of the imaginary part unchanged, as shown here:

$$P_{z+\Delta z}\left(\omega, k_x, k_y\right) = P_z\left(\omega, k_x, k_y\right) e^{\pm i(-\mathrm{Re}(k_z))\Delta z} e^{\pm i(\mathrm{Im}(k_z))\Delta z}. \tag{2.5}$$

As before, the plus and minus signs in Equation 2.5 represent downgoing and upgoing waves. Forward modeling the wavefield using Equation 2.3 in an attenuating medium distorts the phase and attenuates the amplitude of a propagating wave. The reverse sign of the real part of the SSR corrects the distorted phase, while the unchanged sign in the imaginary part further decays the amplitudes of the attenuated wavefield. In order to compensate for the amplitude loss, the sign of the amplitude decaying term in Equation 2.5 has to be reversed as follows:

$$P_{z+\Delta z}\left(\omega, k_x, k_y\right) = P_z\left(\omega, k_x, k_y\right) e^{\pm i(-\mathrm{Re}(k_z))\Delta z} e^{\pm i(-\mathrm{Im}(k_z))\Delta z}. \tag{2.6}$$

Note that the imaginary part of SSR in Equation 2.6 contains both attenuation and evanescent waves. Evanescent waves attenuate naturally. It is important to attenuate the evanescent waves, as oppose to compensate for them. Therefore, I remove the evanescent waves, $k_{\text{eva}}$, from the amplitude compensation, and make them decay following wave physics, yielding:

$$P_{z+\Delta z}\left(\omega, k_x, k_y\right) = P_z\left(\omega, k_x, k_y\right) e^{\pm i(\operatorname{Re}(-k_z))\Delta z} e^{\pm i(-\operatorname{Im}(k_z)+\operatorname{Im}(k_{\text{eva}}))\Delta z} e^{\pm i(\operatorname{Im}(k_{\text{eva}}))\Delta z}, \tag{2.7}$$

where

$$k_{\text{eva}} = \sqrt{\left(\omega s_{wr}\right)^2 - |\mathbf{k}|^2}. \tag{2.8}$$

Attenuation decreases the higher frequencies more than the lower frequencies of the propagating wave. Therefore, compensation through Q migration preferentially enhances higher frequencies. Such amplification may gain high frequency noise and make these frequencies dominate the image. Therefore, I add a low-pass filter to help mitigate high-frequency noise artifacts in migration.

To numerically implement the downward continuation scheme, well-established methods (Gazdag and Sguazzero, 1984; Stoffa et al., 1990; Kessinger, 1992; Ristow and Ruhl, 1994) approximate SSR in different ways to handle laterally varying earth models. Among these methods, I extend the explicit split-step (ESS) algorithm (Kessinger, 1992) for downward continuation wavefield in an attenuating medium with a Q anomaly. The benefits of this method are two-folded. First, ESS is capable of handling heterogeneity of both velocity and Q. Second, although other methods (e.g. Fourier Finite-Difference migration introduced by Ristow and Ruhl (1994) and Valenciano et al. (2011)) are able to image more accurately the laterally varying subsurface model, ESS has more reasonable computational cost and less numerical frequency dispersion that provides a relatively clean image for the later spectral analysis of Q effects. In ESS migration, multiple reference wavefields are generated using the following SSR approximated by Taylor expansion around the reference slowness $\tilde{s}_0$:

$$k_z(\tilde{s}) = k_{z0}(\tilde{s}_0) + \omega\left(\tilde{s} - \tilde{s}_0\right). \tag{2.9}$$

A single wavefield is then estimated at each depth step by an interpolation in the space domain. Because $\tilde{s}$ is the function of $s_{\omega r}$ and Q, the interpolation weights are computed according to the difference between the actual medium slowness/Q and the respective reference slowness/Q at each spatial location.

### Reverse-time migration with Q compensation

I refer to the migration using time-domain wavefield propagation as two-way migration. To be consistent with one-way migration with Q compensation, I assume Q is constant with respect to frequency for two-way migration with Q compensation. Based on this assumption, I use the time-domain viscoacoustic wave equation proposed by (Zhu et al., 2014; Zhu and Harris, 2014) to represent wave propagation in attenuating media. This equation keeps the same form as the acoustic wave equation, but has the following two changes. First, the Laplacian operator $-\nabla^2$ in the original acoustic wave equation becomes fractional $\left(-\nabla^2\right)^{\gamma+1}$, where the variable $\gamma$ is defined as $\gamma = 1/\pi \tan^{-1}(1/Q)$. This fractional Laplacian, defined by an operator $\mathbf{L}$, represents the wave dispersion caused by attenuation. Second, a new term with a time derivative of the wavefield followed by another fractional Laplacian operator $\mathbf{H} = \left(-\nabla^2\right)^{\gamma+1/2}$ is introduced to represent the frequency-dependent amplitude attenuation. The following equation shows the visco-acoustic equation with these two modifications.

$$\left(\eta\mathbf{L} + \tau\mathbf{H}\frac{d}{dt} - v^{-2}\frac{\partial^2}{\partial t^2}\right) P(t) = f(t), \tag{2.10}$$

where $t$ is time, $P$ is the propagated wavefield, $f$ is the source wavefield, and $v$ is the acoustic velocity at the reference frequency $\omega_r$. The absorption and dispersion coefficients are given by $\eta = -v^{2\gamma}\omega_r^{-2\gamma}\cos\pi\gamma$ and $\tau = -v^{2\gamma-1}\omega_r^{-2\gamma}\sin\pi\gamma$. Considering a non-attenuating medium, with $1/Q = 0$, the variable $\gamma = 0$ and $\tau = 0$. The wave is non-dispersive because fractional Laplacian $\mathbf{L} = -\nabla^2$. The amplitude attenuation term has no contribution to the wave propagation. Therefore, Equation 2.10 simplifies to the acoustic wave equation.

Similarly to one-way migration, the backwards propagation in the reverse time migration scheme using Equation 2.10 simply corrects the phase dispersion caused by attenuation, but further attenuates the wave amplitudes. To compensate for both amplitude and phase distortions, I reverse the sign of the amplitude-loss operator and leave the sign of the dispersion operator unchanged. This solution is also proposed by (Zhu et al., 2014; Zhu and Harris, 2014):

$$\left(\eta\mathbf{L} - \tau\mathbf{H}\frac{d}{dt} - v^{-2}\frac{\partial^2}{\partial t^2}\right) P(t) = f(t). \tag{2.11}$$

Attenuation damps the higher frequencies more than the lower frequencies of the propagating wave. Therefore, compensation through Q migration, i.e. the inverse of forward wave propagation preferentially boosts higher frequencies. Such amplification may gain high frequency noise and make these frequencies dominate the image. Therefore, I add a low-pass filter to help mitigate high-frequency noise artifacts in migration:

$$\left(\nabla^2 + \mathbf{N}(\eta\mathbf{L} - \nabla^2) - \mathbf{N}\tau\mathbf{H}\frac{d}{dt} - v^{-2}\frac{\partial^2}{\partial t^2}\right) P(t) = f(t), \tag{2.12}$$

where $\mathbf{N}$ is the low-pass filter in the spatial frequency domain. The cutoff wavenumber is calculated by dividing the cutoff frequency by the maximum velocity of media, as proposed by (Zhu et al., 2014; Zhu and Harris, 2014).

To numerically implement Equation 2.11 for migration, I compute the wavefield in spatial frequency domain to calculate the fractional Laplacian operator $\mathbf{L}$ and $\mathbf{H}$ using the pseudo-spectral method (Kreiss and Oliger, 1972; Orszag, 1972; Fornberg, 1975; Gottlieb and Orszag, 1977). I propagate the wavefield in the time domain using finite-differences with second-order accuracy for the time derivative, and using an absorbing boundary that removes waves coming back from the boundaries as described by Israeli and Orszag (1981).

## Step 2: calculation of parameter $\rho$

### Defining $\rho$ in the migrated image space

Attenuation distorts the propagating wave by decaying its amplitudes and by making the phase velocity change with frequency. In other words, attenuation change the amplitude frequency spectra and phase of a wave. Because the amplitude change of a wave caused by attenuation is easier to observe and measure than attenuation-induced phase dispersion, I use the change of amplitude frequency spectra by attenuation for Q estimation. In this following, I use the term 'spectra' to refer to amplitude frequency spectra.

I use one 1D example to numerically illustrate the impact attenuation has on the amplitude spectra and phase of a propagating wave. Figure 2.1(a) shows two wavelets: the blue curve shows a non-attenuated wave and the red curve shows a wave propagating through an attenuating medium with $Q = 30$. Both waves are recorded at the same time. The traveltime difference between these two waves caused by attenuation-induced velocity dispersion is small from Figure 2.1(a). However, the amplitudes drop in Figure 2.1(a) are significant. The red and blue curves in Figure 2.1(b) are the amplitude spectra of the waves shown by red and blue in Figure 2.1(a), respectively. Figure 2.1(b) shows that attenuation largely damps the higher frequencies of a wave more than its lower frequencies. In fact, the large amplitude decay at the higher frequencies results to such significant drops in amplitude in Figure 2.1(a).

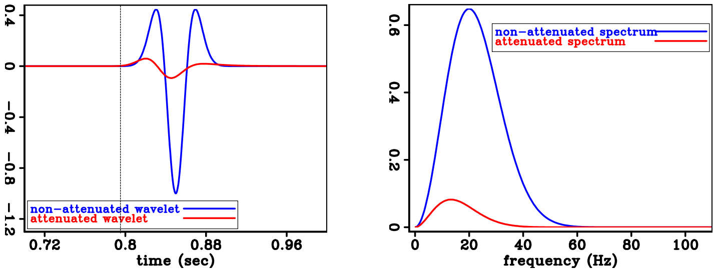

(a) (b)

Figure 2.1: 1D example to numerically illustrate the attenuation impacts on the amplitudes spectra and phase of a propagating wave: (a) the blue curve shows a non-attenuated wave and the red curve shows a wave propagating through an attenuating medium with $Q = 30$. Both waves are recorded at the same time. The dash line indicates the onset of the attenuated wavelet. (b) The amplitude spectra of the waves in Figure 2.1(a). chap2/. Intro.wave.ann,Intro.spex

Besides attenuation, other factors have amplitude impacts on a propagating wave: such as geometrical spreading, instrument response, source/receiver coupling, radiation pattern, geometry settings, reflection/transmission coefficients. To distinguish the amplitude changes caused by attenuation from those caused by other factors, I assume that attenuation is the only frequency-dependent factor on the amplitudes of a wave that attenuates higher frequency more than the lower frequency; while other factors identically scale the amplitudes of different frequencies. This assumption is widely employed in most of the Q estimation literature (Tonn, 1991; Quan and Harris, 1997; Rickett, 2006, 2007). Tonn (1991) developed the `spectral ratio` method that quantifies how much more of a recorded wave's higher frequencies are lost than its lower frequencies by a parameter $\rho$ and contributes attenuation to such frequency loss.

In the same way, I define a parameter $\rho$ to quantify the effect of Q on a compensated seismic. If the migrated image is under–compensated, the higher frequencies of the migrated events are attenuated more than their lower frequencies. On the contrary, if the image is over–compensated, the higher frequencies of the migrated events are over gained compared with their lower frequencies. I show later in this section how this parameter $\rho$ quantifies such spectral change caused by an inaccurate Q compensation.

### Computing $\rho$ from a migrated event

I extend the `spectral ratio` method to compute $\rho$ from a migrated image, which requires spectral analysis of a migrated event. Both the one-way and two-way migration with Q compensation developed in this chapter are depth migrations that map the data from the time domain to the depth domain. As a result, the spectra of a migrated event after depth migration are computed in the spatial frequency (wavenumber) domain, as opposed to the temporal frequency $f$ domain used in `spectral ratio` method. Three major factors have to be considered for the spectral analysis in the wavenumber domain: local velocity, dipping angle of the migrated event and the reflection angle.

I define $\mathbf{k}$ as the local wavenumber of a migrated event, and $|\mathbf{k}| = 2\pi f/v_{\text{int}}$. The interval velocity $v_{\text{int}}$ varies over image location, and thus the absolute value of the wavenumber is dependent on the spatial location at constant frequency. An increase in the interval velocity $v_{\text{int}}$ downshifts the wavenumber, and hence stretches the wavelet in depth. Such a stretch effect is known as the velocity stretching effect. To make the spectra consistently stretched by the velocity over the space, I choose a desired location as a reference location, and record its interval velocity as $v_{\text{ref}}$ and its wavenumber as $\mathbf{k}'$. I map the spectra from the $\mathbf{k}$ domain to $\mathbf{k}'$ by $|\mathbf{k}'| = |\mathbf{k}|v_{\text{int}}/v_{\text{ref}}$.

In addition, the migrated event has a dipping angle $\alpha$ with respect to the horizontal direction. The wavenumber $\mathbf{k}$ of a dipping event is a vector of which the direction is perpendicular to the event. In practice, it is difficult to window a migrated event with a directional window which is perpendicular to the event. Thus, I window the migrated event along its depth direction and compute its spectra in the vertical component $\mathbf{k_z}$ of the wavenumber $\mathbf{k}$. Then I map the spectra from $\mathbf{k_z}$ to $\mathbf{k}$ by $|\mathbf{k}| = |\mathbf{k_z}|/\cos\alpha$. If the event represents a flat layer so $\alpha = 0$, $\mathbf{k}$ equals its vertical component $\mathbf{k_z}$. I assume the event at the selected reference location for $\mathbf{k}'$ is flat, so

$\alpha = 0$. Therefore, mapping from the $\mathbf{k_z}$ to the $\mathbf{k}'$ becomes $|\mathbf{k}'| = (|\mathbf{k_z}| v_{\text{int}}) \,/\, (v_{\text{ref}} \cos\alpha)$.

Moreover, considering that a migrated event from angle-domain common image gather (ADCIG) at a selected reflection angle, $\gamma$, its vertical wavenumber $|\mathbf{k_z}| = |\mathbf{k}| \cos\gamma$, and thus decreases and is downshifted at large angles. As a result, the migrated event at a far angle is more stretched in depth than at a near angle. Such a stretch effect is the same as the well-known normal moveout stretch (NMO) in the angle gathers. This phenomenon is also addressed by Sava et al. (2005) that the true amplitudes in ADCIGs are not preserved and thereby a Jacobian weighting function is required to correct the amplitudes. If the reflectors have gentle dips and the horizontal velocity has gentle variation, the Jacobian weighting function can be approximated to $1/\cos\gamma$. Thus, mapping the spectra from the $\mathbf{k_z}$ to the $\mathbf{k}$ domain introduces an additional $\cos\gamma$ term in the angle gathers. If the event for $\mathbf{k}'$ is chosen at zero angle, then the mapping from $\mathbf{k_z}$ to $\mathbf{k}'$ in the angle gathers is given by $|\mathbf{k}'| = (|\mathbf{k_z}| v_{\text{int}}) \,/\, (v_{\text{ref}} \cos\alpha \cos\gamma)$. In this following numerical examples, I assume the dips of the reflectors and the horizontal variation of the velocity are gentle. If not, a more sophisticated Jacobian weighting function (Sava et al., 2005) needs to be considered, which depends on the reflection angle $\gamma$, the dipping angle $\alpha$ and the local velocity $v_{\text{int}}$.

Therefore, before performing the spectral analysis in the wavenumber domain, I first compute the spectra in a local vertical wavenumber $\mathbf{k_z}$ domain. Then I map $\mathbf{k_z}$ to a reference wavenumber $\mathbf{k}'$ at a selected reference location. The equation used for this mapping is

$$|\mathbf{k}'| = \frac{|\mathbf{k_z}| v_{\text{inv}}}{v_{\text{ref}} \Theta}, \tag{2.13}$$

where $\Theta = \cos\gamma \cos\alpha$ if the migrated event for spectral analysis is in ADCIG; while $\Theta = \cos\alpha$ for the stacked image. In the following numerical examples, I assume the dipping angles of the migrated events are smaller than 30 degree and thus approximate $\cos\alpha$ to be zero. However, such an approximation is not valid for reflectors with a large dipping angle in which the term $\cos\alpha$ needs to be considered.

I consider two migrated images to compute $\rho$: one image, $I_1$, is migrated with Q compensation model, $Q_1$; the other is migrated using the same recorded data and same compensation methods but with a different Q model, $Q_2$. The model $Q_2$ equals the Q model of the actual attenuating media, but does not equal $Q_1$. In this derivation, I assume I know $Q_2$. However, $Q_2$ is unknown in reality, which situation will be discussed later in this section. Theoretically, $I_2$, known as the reference image, is exactly compensated and the effect of Q on $I_2$ is fully corrected. At the same image location, I define the spectrum of a migrated event in $I_1$ as $R_1(\mathbf{k}')$ and the spectrum of a migrated event in the reference image as the reference spectra $R_2(\mathbf{k}')$, where $\mathbf{k}'$ is the reference wavenumber. The higher wavenumber components of the spectrum $R_1(\mathbf{k}')$ are either attenuated or over–corrected; while the spectrum $R_2(\mathbf{k}')$ is exactly compensated and any effects of Q are fully corrected. Because these two images are migrated in exactly the same way aside from a different Q model, the ratio between $R_1(\mathbf{k}')$ and $R_2(\mathbf{k}')$ simplifies to be a function of only Q. I derive that ratio based on the `spectral ratio` method (See Appendix A) and show the logarithm of this ratio as follows:

$$\ln[R_1(\mathbf{k}')/R_2(\mathbf{k}')] = \rho|\mathbf{k}'| + G_0, \tag{2.14}$$

where $G_0$ is constant and equals zero. The logarithm of the ratio between $R_1(\mathbf{k}')$ and $R_2(\mathbf{k}')$ makes the ratio linear with a slope of $\rho$ with respect to $|\mathbf{k}'|$. In field applications, the spectra are contaminated with noise that is especially strong at low and high wavenumbers. I take a middle range of the spectra that still preserves the linearity and estimate its slope by linear least-squares regression. Specifically, I find the wavenumber at which the spectrum is maximized by an automatic picker, and set a desired range around this wavenumber. Equation 2.14 shows the parameter $\rho$ is independent of $\mathbf{k}'$ and can be derived to be (See Appendix A):

$$\rho = \int \frac{v_{\text{ref}}}{2v_{\text{int}}}(\frac{1}{Q_1} - \frac{1}{Q_2})dl, \tag{2.15}$$

where the integral is taken along the wave-path.

Equation 2.15 shows how a difference between $Q_1$ and the actual attenuating media $Q_2$ changes the value of $\rho$. Theoretically, if $Q_1 = Q_2$, image $I_1$ has no attenuation impacts and $\rho = 0$. If $Q_1$ does not equal $Q_2$, image $I_1$ is either under– or over–compensated, and $\rho$ becomes a non-zero value. Table 2.1 summarizes how the sign of $\rho$ points to the error in the current $Q$ model. If $\rho$ is positive, $I_1$ is over–compensated, indicating the current model $Q_1$ is smaller than the true model $Q_2$. If $\rho$ is negative, $I_1$ is under–compensated, indicating the current model $Q_1$ is larger than the true model $Q_2$.

Figure 2.2 shows the quantitative relation between the current model $Q_1$ and the

Table 2.1: The relation of the sign of $\rho$ and the accuracy of the current $Q$ model

| Value of $\rho$ | Image | Current model $Q_1$ vs true model $Q_2$ |
|---|---|---|
| $\rho > 0$ | over–compensation | $Q_1 < Q_2$ |
| $\rho < 0$ | under–compensation | $Q_1 > Q_2$ |
| $\rho = 0$ | adequately compensated | $Q_1 = Q_2$ |

$\rho$ value. Both Figure 2.2 and Equation 2.15 show that the smaller the absolute value of $\rho$ is, the closer the current model $Q_1$ is to the true model $Q_2$. That is, the value of $\rho$ also effectively indicates the accuracy of the current model $Q_1$. Therefore, Equation 2.1 can be used to evaluate capable of evaluating the accuracy of $Q_1$, and minimizing the objective defined in Equation 2.1 allows us to update $Q_1$ in the correct direction.

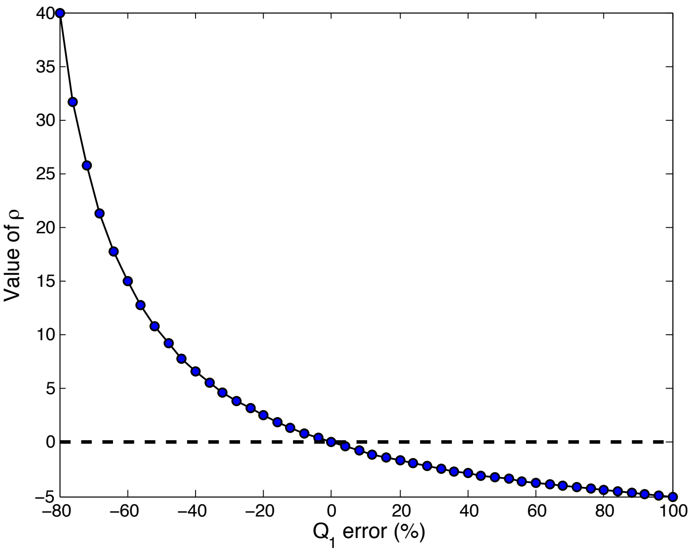

Figure 2.2: An example shows a quantitative relation between the current $Q_1$ model and the $\rho$ value measured from the image. The image is migrated with a flat reflector at a depth of 500 m in a spatially constant attenuating medium $Q = 50$. The Q error is calculated as $(Q_1 - Q_2)/Q * 100\%$. chap2/. Irho2pdf

Minimizing the objective defined in Equation 2.1 to estimate $Q_1$ requires a reference image. Generally, the model of the actual attenuating media $Q_2$ is unknown. It is impossible for us to obtain reference spectra from the reference image by the above way. An alternative to the reference image is $I_1$ itself. The focus of my study is Q anomalies in the subsurface that have a variety of effects on different subsets of an image. Prior information (e.g. well logs) or proper interpretation allows us to pick a reference location in a seismic image that has the least effect from these Q anomalies. In this location we calculate the reference spectra. In this way, the differences between $R_1(\mathbf{k}')$ at a target location and $R_2(\mathbf{k}')$ at a reference location in the same image are caused by not only the Q anomalies, but also other factors including different illumination caused by acquisition limitations, different reflection coefficients of different reflectors, and different geometrical spreading because of different wave-paths. I assume these factors are all frequency-independent. Consequently, they are independent of $\rho$ and fall into the intercept term $G_0$ in Equation 2.14. Moreover, computing the reference spectra from the same image $I_1$ allows us to remove the common factors by the spectral ratio $R_1(\mathbf{k}')/R_2(\mathbf{k}')$ in Equation 2.14. For instance, the injected source signature and the spectral change caused by the conventional imaging condition of migration are removed.

### Computing $\rho$ from a migrated image

The migration methods presented in this chapter produce a five-dimensional migrated cube: three of them are the coordinates of the physical space. The other two dimensions are the in-line and cross-line subsurface offset. I will use the term **stacked image** if the image cube is extracted at the zero subsurface offset in both in-line and cross-line and only has three spatial coordinates. The stacked image represents the geological structures in the subsurface. Knowing the geological setting helps interpret a reference location that is least influenced by the Q anomaly, which allows me to compute $\rho$ from the stacked image. However, the stacked image mixes the rays of different length. To perform amplitude analysis it is often useful to exploit the redundancy of seismic data and thus use the image with more dimensions. I use the entire five-dimensional cube to compute $\rho$. Alternatively, one can transform the in-line and cross-line subsurface offsets to the reflection opening angle ($\gamma$) and reflection azimuth angle ($\psi$) at each reflection point. These two dimensions constitute the subsets of the whole image with fixed surface location and are known as Angle domain Common Image Gathers (ADCIGs). I will refer to the five-dimensional image with ADCIGs as a **prestack image**. In this study, I investigate methods to compute $\rho$ from both the stacked image and prestack image.

To compute $\rho$ from a stacked image, I select one or more surface locations that appear to be least impacted by the interpreted Q anomalies. The traces corresponding to these subsets of the image are used as the reference traces. At each image point, I use a window of which the center is the image point and compute the target spectra of the windowed image with a correction using Equation 2.13. This target spectra are referenced to the spectra of the windowed reference traces. The windows for the reference image and the target image have the same size and their window center are at the same depth, because the geological structures in the subsurface generally have less horizontal variation than vertical variation. In this way, $\rho$ can be computed using Equation 2.14 for all image points. To choose the window size, I employ an elongated window. The window is narrow in the horizontal direction, which is able to extract a group of neighboring traces and enables us to average them to stack the noise and migration artifacts in the spectra. The window is wide along depth, which allows me to assume the spectral variations caused by structure differences in each window are statistically the same. However, a window that is wide along depth makes $\rho$ not able to represent the effect of Q on its image point, because the parameter $\rho$ averages the effect of Q of throughout the windowed image.

To compute $\rho$ from a prestack image, it is reasonable to select the near angles as the reference angles, and compare them to the far angles. Waves reflected by different angles are affected by Q anomalies differently. Equation 2.1 shows the longer the wave travels, the larger the absolute of $\rho$ value is, so we can tell the current Q model is inaccurate. In fact, pairing the near and far angles to compute their spectral variation also applies to attenuating media with Q values that are constant over space.

In field application, however, near angles are possibly missing, or there is not enough effective angle range for a strong spectral variation in near and far angles. In that case, I select one or multiple ADCIGs as the reference ADCIGs that are interpreted to be least affected by the anomalies. Such selection can be the same as in the stacked image. In a narrow azimuth acquisition survey, the reflection azimuth angle ($\psi$) has a little range, so I focus on angle gathers of which the axes are the reflection opening angle ($\gamma$) and depth. At each location of a target ADCIG, I use an elongated window with its center being at this location. The window size is selected by the same criteria as in the stacked image. To compute $\rho$, the target window is paired with the one in the reference ADCIG that is the same size and is in the same position. The migrated cube has five dimensions, and therefore its computation required more memory and time than the stacked image. Based on size of the model and the computational resources available, one can choose to compute $\rho$ for every point in each ADCIG or at some selected representative subset of ADCIG.

# DERIVATION OF GRADIENTS OF THE OBJECTIVE WITH RESPECT TO Q

To derive the gradients of the objective defined in Equation 2.1 with respect to Q, I take the first derivative of this objective function with respect to each point in the Q model. The resulting Q gradient is

$$\left(\frac{\partial J}{\partial Q}\right)^{*} = \sum_{x} \left(\frac{\partial \rho}{\partial Q}\right)^{*} \rho = \sum_{x} \left(\frac{\partial I}{\partial Q}\right)^{*} \left(\frac{\partial \rho}{\partial I}\right)^{*} \rho, \tag{2.16}$$

where $^{*}$ means adjoint, and both $I$ and $\rho$ are the function of the current Q model. Equation 2.16 has a clear physical interpretation and mathematically explains that two steps are required to derive the Q gradient. The term $\left(\frac{\partial \rho}{\partial I}\right)^{*} \rho$ is known as the image perturbation ($\Delta I$), and reflects the difference between the target image and the reference image. Such differences are only caused by attenuation. If the current Q model equals the true Q model, $\rho = 0$ and thus the image perturbation is zero. The term $\left(\frac{\partial I}{\partial Q}\right)$, known as the wave-equation tomographic operator, and its adjoint $\left(\frac{\partial I}{\partial Q}\right)^{*}$ back projects the image perturbation to a perturbation in the interval Q model. This perturbed Q model will be used as Q model updating direction. The two steps to compute the Q gradient are: 1) calculating the image perturbation ($\Delta I$), and 2) back projecting $\Delta I$ to a perturbation in the Q model.

## Image perturbation

The image perturbation ($\Delta I$) is a function of the current Q model and is shown by the derivation in Appendix B to be:

$$\Delta I\left(\mathbf{x}'; Q\right) = \mathtt{F}^{*}\left(p_1\left(\mathbf{k}, \mathbf{x}'; Q\right) \mathtt{Z}^{*}\left(\frac{1}{R_1\left(\mathbf{k}', \mathbf{x}'; Q\right)} \frac{1}{\left|\mathbf{k}'\right|} \rho\left(\mathbf{x}'; Q\right)\right)\right). \tag{2.17}$$

If $\rho$ is computed from the stacked image, $\mathbf{x}'$ in Equation 2.17 is the spatial location $(x, y, z)$ at the center of the window. At the given current Q model, the operator $\mathtt{F}$ is the windowed Fourier transform (Gabor, 1946) that transforms the windowed image into the vertical wavenumber domain, $R_1(\mathbf{k}, \mathbf{x}'; Q) p_1\left(\mathbf{k}, \mathbf{x}'; Q\right)$. Here $R_1\left(\mathbf{k}, \mathbf{x}'; Q\right)$ is the amplitude spectra and $p_1\left(\mathbf{k}, \mathbf{x}'; Q\right)$ is the phase as defined in Appendix B. The operator $\mathtt{F}^{*}$ is the inverse windowed Fourier transform. The operator $\mathtt{Z}$ maps the spectra $R_1(\mathbf{k}, \mathbf{x}'; Q)$ to $R_1(\mathbf{k}', \mathbf{x}'; Q)$ using Equation 2.13, where $\mathbf{k}'$ is the reference wavenumber . Its adjoint $\mathtt{Z}^*$ maps the spectra $R_1(\mathbf{k}', \mathbf{x}'; Q)$ back to $R_1(\mathbf{k}, \mathbf{x}'; Q)$. In Equation 2.17, the inverse of $R_1(\mathbf{k}', \mathbf{x}'; Q)$ acts to a weighting function that enhances the energy at the attenuated region of the image.

If $\rho$ is computed from the ADCIGs, $\mathbf{x}'$ in Equation 2.17 is the spatial location and the reflection opening angle $(x, y, z, \gamma)$. The definition of the other variables and operators in Equation 2.17 are the same as the ones in the stacked image. The operator $\mathtt{F}$ takes the Fourier transform of the windowed events in each ADCIG. Then I transform the computed image perturbation from the subsurface angle domain to the subsurface offset domain (Sava and Fomel, 2003; Biondi and Tisserant, 2004), to make it consistent with the input of the back propagation operator that I will illustrate next.

## Wave-equation Q tomographic operator

The term $\left(\frac{\partial I}{\partial Q}\right)$ is defined as the wave-equation Q tomographic operator in this study, that links a perturbation in Q model to a change in the image. Its adjoint $\left(\frac{\partial I}{\partial Q}\right)^*$ back projects the perturbed image from Equation 2.17 to a perturbed Q model. The derivative of the image with respect to the Q model can be derived (Appendix C) as the sum of the attenuation-induced perturbed source wavefield multiplied by the background receiver wavefield and the attenuation-induced perturbed receiver wavefield multiplied by the background source wavefield:

$$\frac{\partial I(\mathbf{x}, \mathbf{h})}{\partial Q(\mathbf{y})}|_{Q_0} = \sum_{\omega, \mathbf{x_s}, \mathbf{x_r}} \left(\frac{\partial G(\mathbf{x}-\mathbf{h}, \mathbf{x_s}, \omega; Q_0)}{\Delta Q(\mathbf{y})}\right)^* G^*(\mathbf{x}+\mathbf{h}, \mathbf{x_r}, \omega; Q_0) d(\mathbf{x_r}, \mathbf{x_s}, \omega)$$
$$+ \sum_{\omega, \mathbf{x_s}, \mathbf{x_r}} G^*(\mathbf{x}-\mathbf{h}, \mathbf{x_s}, \omega; Q_0) \left(\frac{\partial G(\mathbf{x}+\mathbf{h}, \mathbf{x_r}, \omega; Q_0)}{\Delta Q(\mathbf{y})}\right)^* d(\mathbf{x_r}, \mathbf{x_s}, \omega). \tag{2.18}$$

where $G$ is the Green's function of the wave equation; $d$ is the surface recorded data; $\mathbf{x}_s$ and $\mathbf{x}_r$ are the source and receiver coordinates; $\mathbf{x}$ is the Green's functions' spatial coordinate; $\mathbf{h}$ is the subsurface offset; $\mathbf{y}$ is the Q model's spatial coordinates, and $\omega$ is frequency.

I will express the formula of the Green's function and its derivative with respect to a Q model based on both one-way (Equation 2.2 and Equation 2.3) and two-way wave equations (Equation 2.10 and Equation 2.11) with Q. Their derivations are shown in Appendix C.

### One-way Green's function and its derivative with respect to a Q model

The Green's function of the one-way visco acoustic wave equation is expressed as follows:

$$\begin{cases} \left(\frac{\partial}{\partial z} + ik_z\right) G(\mathbf{x}, \mathbf{x}_s, \omega) = 0 \\ G(x, y, z = 0, \mathbf{x}_s, \omega) = \delta(\mathbf{x} - \mathbf{x}_s) \end{cases}, \tag{2.19}$$

and

$$\begin{cases} \left(\frac{\partial}{\partial z} - ik_z\right) G(\mathbf{x}, \mathbf{x}_r, \omega) = 0 \\ G(x, y, z = 0, \mathbf{x}_r, \omega) = \delta(\mathbf{x} - \mathbf{x}_r) \end{cases}, \tag{2.20}$$

where $G(\mathbf{x}, \mathbf{x}_s, \omega)$ is the source side Green's function at the image point $\mathbf{x}$ with the source located at $\mathbf{x}_s$; $G(\mathbf{x}, \mathbf{x}_r, \omega)$ is the receiver side Green's function at the image point $\mathbf{x}$ with the data recorded at $\mathbf{x}_r$; and $k_z$ is the vertical wavenumber in Equation 2.4.

I linearize the derivative of the Green's function with respect to Q at $\mathbf{y}$ using Equation 2.2 and 2.4 by a Taylor expansion as follows:

$$\begin{aligned} \frac{\partial G\left(\mathbf{x}, \mathbf{x_s}, \omega; Q_0\right)}{\partial Q\left(\mathbf{y}\right)} &= -\frac{i\partial k_z}{\partial Q}\,|_{Q_0}\, G\left(\mathbf{y}, \mathbf{x_s}, \omega; Q_0\right) G\left(\mathbf{x}, \mathbf{y}, \omega; Q_0\right) \\ \frac{\partial G\left(\mathbf{x}, \mathbf{x_r}, \omega; Q_0\right)}{\partial Q\left(\mathbf{y}\right)} &= \frac{i\partial k_z}{\partial Q}\,|_{Q_0}\, G\left(\mathbf{y}, \mathbf{x_r}, \omega; Q_0\right) G\left(\mathbf{x}, \mathbf{y}, \omega; Q_0\right), \end{aligned} \tag{2.21}$$

where

$$\frac{\partial k_z}{\partial Q} = \frac{\omega}{\sqrt{1 - \frac{|\mathbf{k}|^2}{\omega^2 \tilde{s}^2}}} \frac{-s_{\omega r}}{Q^2} \left(\frac{i}{2} - \frac{i}{\pi Q} \ln\left(\omega/\omega_r\right) - \frac{1}{\pi} \ln\left(\omega/\omega_r\right)\right) \tag{2.22}$$

### Two-way Green's function and its derivative with respect to a Q model

The Green's function in the two-way visco acoustic wave equation is expressed as follows:

$$\left\{ \begin{array}{l} \left(\eta \mathbf{L} - \tau \mathbf{H}\frac{d}{dt} - v^{-2}\frac{\partial^2}{\partial t^2}\right) G(\mathbf{x},\mathbf{x}_s,\omega) = 0 \\ G(x,y,z=0,\mathbf{x}_s,\omega) = \delta(\mathbf{x}-\mathbf{x}_s) \end{array} \right. , \tag{2.23}$$

and

$$\left\{ \begin{array}{l} \left(\eta \mathbf{L} - \tau \mathbf{H}\frac{d}{dt} - v^{-2}\frac{\partial^2}{\partial t^2}\right) G(\mathbf{x},\mathbf{x}_r,\omega) = 0 \\ G(x,y,z=0,\mathbf{x}_r,\omega) = \delta(\mathbf{x}-\mathbf{x}_r) \end{array} \right. . \tag{2.24}$$

Again, I linearize the derivative of the Green's function with respect to Q $\mathbf{y}$ using Equation 2.11 by a Taylor expansion as follows:

$$\begin{array}{l} \frac{\partial G\left(\mathbf{x},\mathbf{x_s},\omega;Q_0\right)}{\partial Q\left(\mathbf{y}\right)} = -\mathbf{A} G\left(\mathbf{y},\mathbf{x_s},\omega;Q_0\right) G\left(\mathbf{x},\mathbf{y},\omega;Q_0\right) - \mathbf{B}\frac{d}{dt} G\left(\mathbf{y},\mathbf{x_s},\omega;Q_0\right) G\left(\mathbf{x},\mathbf{y},\omega;Q_0\right) \\ \frac{\partial G\left(\mathbf{x},\mathbf{x_r},\omega;Q_0\right)}{\partial Q\left(\mathbf{y}\right)} = -\mathbf{A} G\left(\mathbf{y},\mathbf{x_r},\omega;Q_0\right) G\left(\mathbf{x},\mathbf{y},\omega;Q_0\right) - \mathbf{B}\frac{d}{dt} G\left(\mathbf{y},\mathbf{x_r},\omega;Q_0\right) G\left(\mathbf{x},\mathbf{y},\omega;Q_0\right) \end{array} \tag{2.25}$$

where $\mathbf{A}$ and $\mathbf{B}$ are the partial derivatives with respect to Q at the background $Q_0$:

$$\begin{array}{ll} \mathbf{A} = \frac{\partial(\eta\mathbf{L})}{\partial Q}\,|_{Q_0} & = -\frac{\left(2\eta\ln v - 2\eta\ln\omega_0 - \pi v\tau\right)\mathbf{L} + \eta\mathbf{L}\ln\left(-\nabla^2\right)}{\pi\left(Q_0^2+1\right)} \\ \mathbf{B} = \frac{\partial(\tau\mathbf{H})}{\partial Q}\,|_{Q_0} & = -\frac{\left(2\tau\ln v - 2\tau\ln\omega_0 + \pi v^{-1}\eta\right)\mathbf{H} + \tau\mathbf{H}\ln\left(-\nabla^2\right)}{\pi\left(Q_0^2+1\right)} . \end{array} \tag{2.26}$$

## INVERSION SCHEME

The inversion of this WEMQA method minimizes the objective function in Equation 2.1. Figure 2.3 presents the workflow of this inversion method. At each iteration, I first migrate the attenuated data with the current Q model to compensate for attenuation in the seismic image. Second, I compute the parameter $\rho$, which quantifies Q effects in the migrated image. Third, I use the wave-equation tomographic operator to calculate the gradient based on Equation 2.16, and update the search direction based on the current gradient using the Polak-Ribire conjugate-gradient algorithm (Polak, 1969). Finally, I perform a line search to obtain a step length by minimizing the objective defined in Equation 2.1, and update the current Q model by adding search direction scaled by the step length. The method continues iterating until convergence criteria is reached.

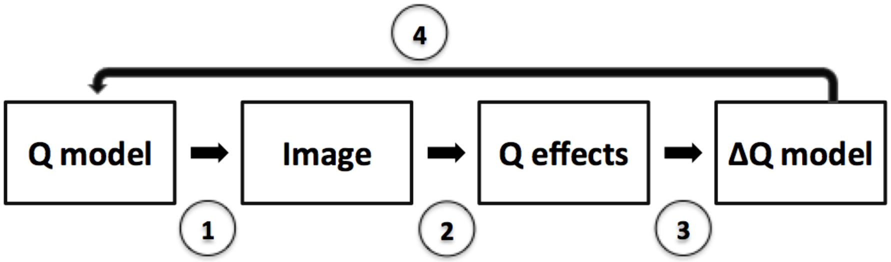

Figure 2.3: The workflow of the WEMQA inversion scheme chap2/. workflow

## NUMERICAL EXAMPLE

In the following three numerical examples, I refer to WEMQA that employs one-way wavefield continuation in the migration and tomography as the **one-way method**; I refer to WEMQA that employs time-domain wavefield propagation as the **two-way method**. Also, I refer to WEMQA that computes $\rho$ from the stacked image as the **stacked method** and from ADCIGs as the **prestack method**.

First, I test the proposed WEMQA method on a simple 2D synthetic example. With enough iterations, the WEMQA methods, from either stacked image or ADCIGs using either one-way or two-way method, have the same performance in this simple example. I applied one-way prestack method to this simple example. As for the Q inversion, I assume I know the velocity model.

Figure 2.4 is the true Q model for inversion. This model has a rectangular Q anomaly ($Q = 20$) in an almost non-attenuating medium ($Q = 10,000$). The Q model is shown on a logarithm scale for a convenient display and will be the same in all the following examples. I generated synthetic seismic data using this Q model, a spatial constant velocity model ($4,000$ m/s), and a reflectivity model with a horizontal reflector at $z = 900$ m, with 401 receivers and 101 shots uniformly distributed along the surface. The source wavelet is a Ricker wavelet with its central frequency of 50Hz. I migrated the attenuated data using the initial Q model ($Q = 10,000$) and the correct velocity (4000 m/s), and computed the angle gathers. Figure 2.5(a) and Figure 2.5(b) are the angle gathers at $x = 0$ m and $x = 1,000$ m, respectively. The near angles are more attenuated than the far angles when the reflection occurs right

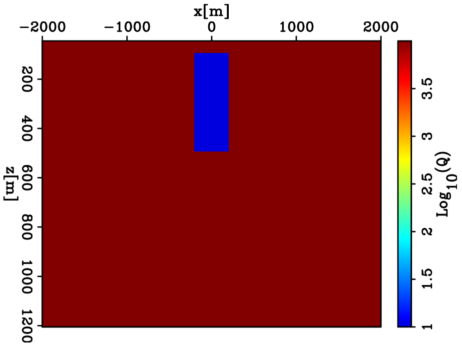

Figure 2.4: True Q model with a rectangular Q anomaly ($Q = 20$) and almost non-attenuating medium ($Q = 10,000$). chap2/. errlogqQ

below the Q anomaly. Therefore, the image in Figure 2.5(a) has weaker event at the near angles than at the far angles. The opposite result is true for angle gathers at $x = 1,000$ m in Figure 2.5(b).

I compute the slope maps for each angle gather using Equation 2.14. Figure 2.5(b) shows that the near angle at $x = 1000$ m has little influence by the Q anomaly. Because this model only contains one reflector, the choice of window size is flexible. The length of my window is 200 m to include the reflector and the width includes 3 traces. I take the angle gather at $x = 1,000$ m as the reference. The slope represents the average absorption for each angle at the window center. Figures 2.5(c) and 2.5(d) are the slope value of Figure 2.5(a) and 2.5(b), with the blue color indicating the attenuated region. Figures 2.5(c) and 2.5(d) accurately show attenuated angle: near angles at $x = 0$ m and far angles at $x = 1000$ m.

Figures 2.6(a) and 2.6(b) are the corresponding image perturbations to Figures 2.5(c) and 2.5(d) calculated using Equation 2.17. Since the reference spectra are assumed to not be attenuated, the polarities are both negative, indicating that the images at those locations are under–compensated and smaller Q is need for the updates. Figure 2.6(c)and 2.6(d) are the image perturbation at near angle 0° and at a relatively far angle 25°, respectively. The results show that the near angles are only influenced by the Q anomaly in Figure 2.4 at the reflection image points that are very closely positioned in the horizontal direction to the anomaly; while the larger angles have the most attenuation influence at the reflection image points with certain horizontal distance from the anomaly.

Figure 2.7(a) is the search direction for the first iteration. Because WEMQA minimizes the objective function (Equation 2.1), therefore, the search direction is opposite of the gradient. The negative updates shown in blue lower the value of the

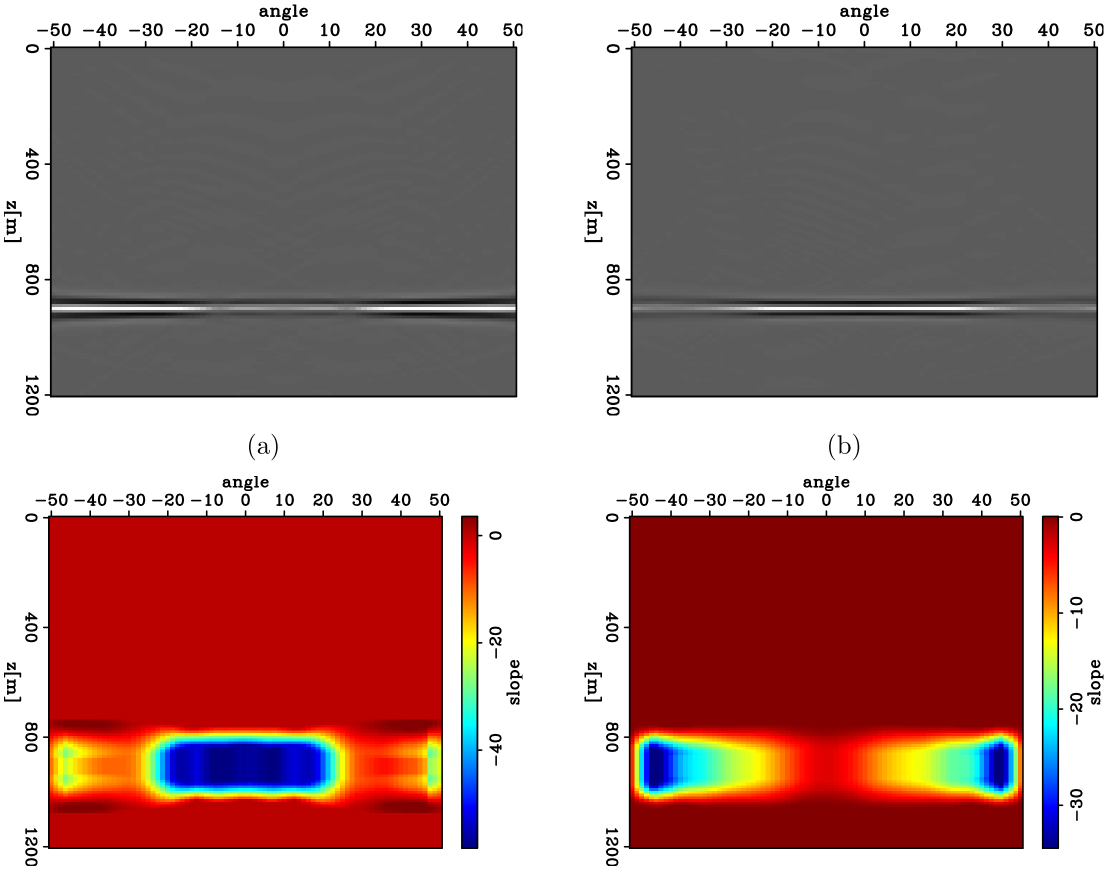

(a)

(b)

(c)

(d)

Figure 2.5: (a) Angle gather at $x = 0$ m. The near angles are more attenuated than the far angles. (b) Angle gather at $x = 1,000$ m. The far angles are more attenuated than the near angles. (c) The slope value of Figure 2.5(a) using the angle gather at $x = 1,000$ m as the reference. (d) The slope value of Figure 2.5(b) using the angle gather at $x = 1,000$ m as the reference. chap2/. errlogq.bangN,errlogq.bangF,errlogq.refNX.slop,errlogq.refFX.slop

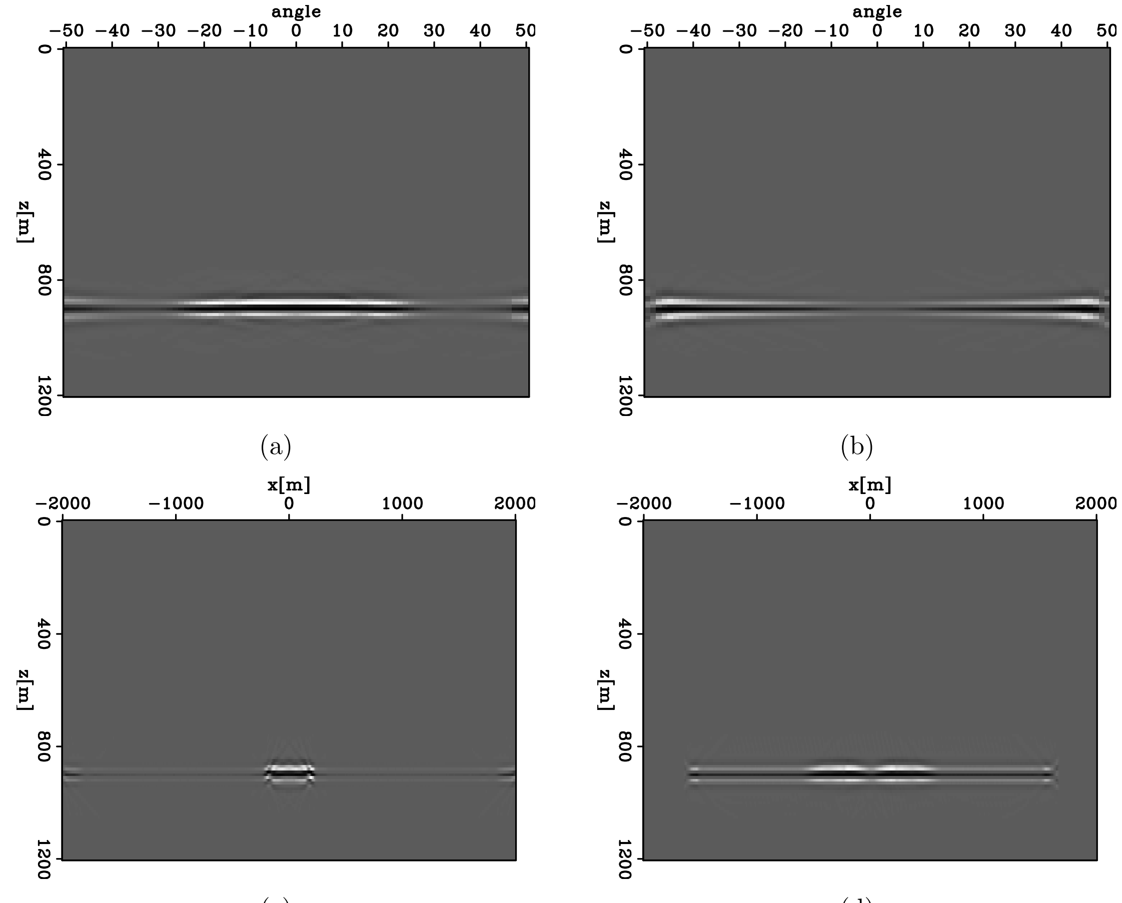

(a)

(b)

(c)

(d)

Figure 2.6: (a) Image perturbations corresponding to Figure 2.5(c); (b) Image perturbations corresponding to Figure 2.5(d). (c) The image perturbation at near angle 0°; (d) The image perturbation at near angle 25°. chap2/. errlogq.refNX.dang,errlogq.refFX.dang,errlogq.refNA.dang,errlogq.refFA.dang

current Q in the blue regions at this iteration's update. The energy in this update spreads out in the image space; while the expected result should have its energy focused around the Q anomaly area. After 20 iterations, the WEMQA method focuses the strongest parts of its update in the expected region, as shown in Figure 2.7(b). The results show that the estimates in Figure 2.7(b) well retrieve the shape, location and value of the Q anomaly.

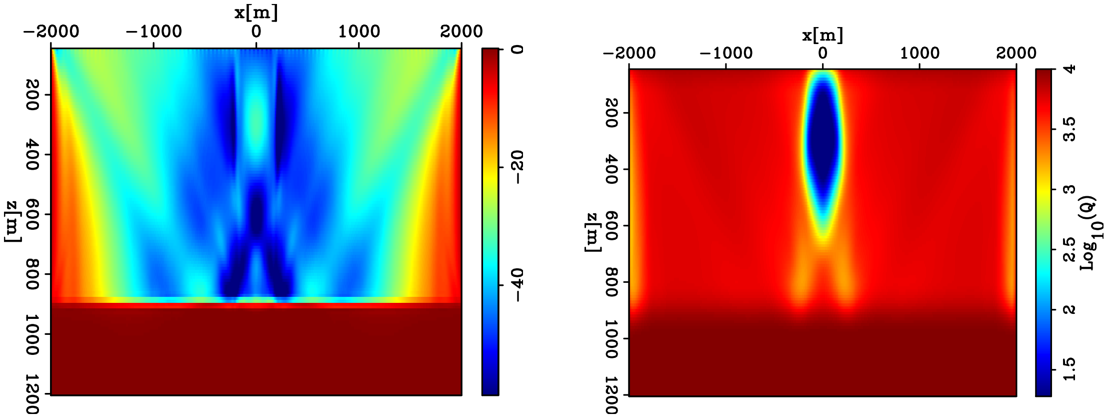

(a) (b)

Figure 2.7: (a) The search direction for the first iteration being back projected from the prestack image perturbation; (b) The inversion results. chap2/. errlogq.Dq.ref,errlogq-bq-inv

Figures 2.8(a) and 2.8(b) show the angle gathers at $x = 0$ m migrated using the inverted Q model in Figure 2.7(b) and the true Q model in Figure 2.4, respectively. Figure 2.8(a), comparable to Figure 2.8(b), adequately compensates for the attenuated near angles in Figure 2.5(a). Similarly, Figure 2.8(c), the angle gather at $x = 1000$ m migrated with the inverted Q model in Figure 2.7(b), compensates for the attenuated far angles in Figure 2.5(b), and shows similar results to Figure 2.8(d), which is obtained with the true Q model.

For a more complex synthetic test, I use a portion of the SEAM synthetic velocity to which I have added two gas clouds with lower velocity than the surrounding sediments (Figure 2.9(a)). The Q model (in logarithmic scale) shown in Figure 2.9(b) includes these two gas clouds as regions with high attenuation. I generate synthetic data with shots and receivers uniformly distributed along X direction at the surface, and a Ricker wavelet with 15 Hz central frequency as the source. The reference frequency for both forward modeling with Q attenuation and migration with Q compensation is 15 Hz, the same as the central frequency of the source wavelet. I assume

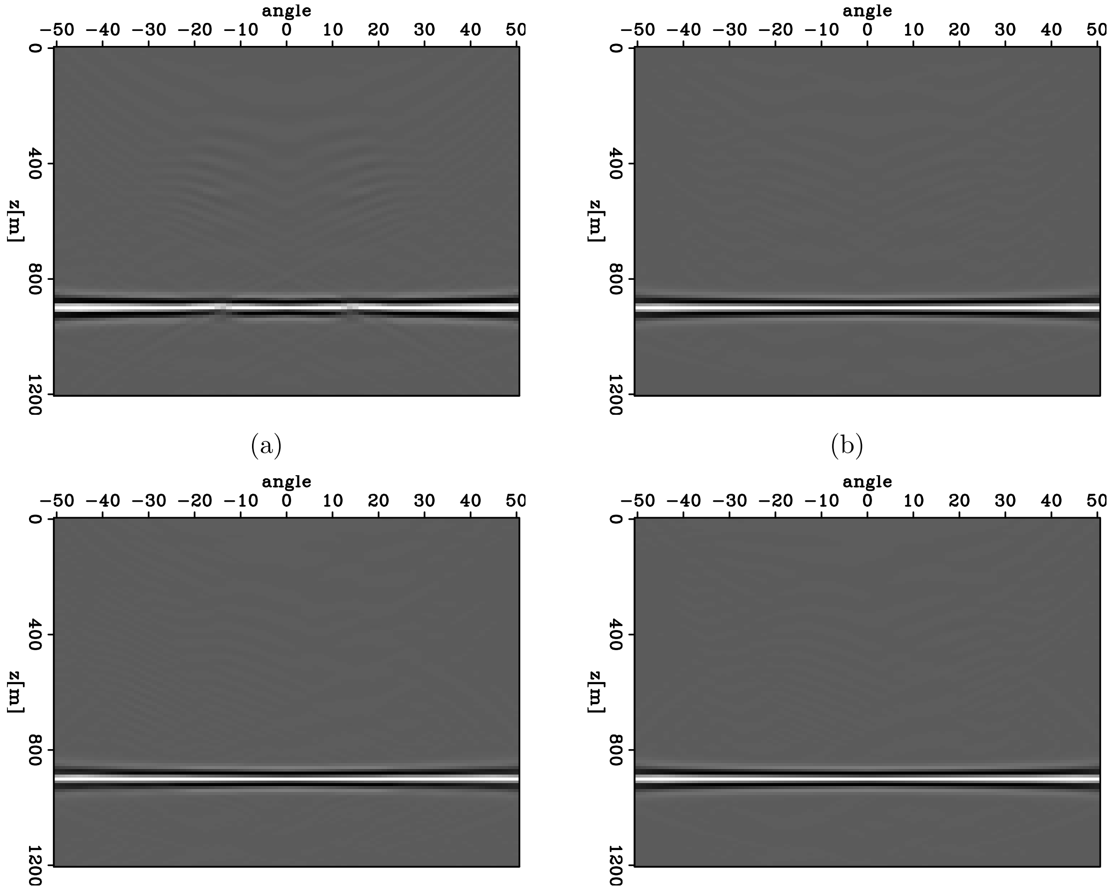

(a)

(b)

(c)

(d)

Figure 2.8: (a) Angle gather at $x = 0$ m migrated using the inverted Q model in Figure 2.7(b). (b) Angle gather at $x = 0$ m migrated using the true Q model in Figure 2.4. (c) Angle gather at $x = 1000$ m migrated using the inverted Q model in Figure 2.7(b). (d) Angle gather at $x = 1,000$ m migrated using the true Q model in Figure 2.4. [**ER**] chap2/. errlogq.angN,errlogq.rangN,errlogq.angF,errlogq.rangF

I know the velocity model but do not know the Q model. The initial Q model for the WEMQA inversion is spatially constant with Q=10,000. After migration on the attenuated data with the current Q model, we generate the image perturbation by calculating the slope of the logarithm of the spectral ratio between the windowed events of each trace and the events in the reference window. The window size is 500 m wide in Z and 50 m wide in X, and 50 sliding windows are used for each trace. The reference windows centered at x=3,000 m were selected because they appear to be the areas least influenced by these two shallow gas clouds. Because both the structures and velocities in this example do not have strong horizontal variation, I estimate the effective Q from the stacked image.

Figure 2.9(c) (in logarithmic scale) shows the inversion results after 20 iterations. The inversion scheme used in this example employs a weighting function that is multiplied by the updated gradient, in order to mute the updates above the water bottom and focus the updates below. The results recover the location of these two gas anomalies. These two inverted anomalies almost match the shape and value of the true anomalies.

Figure 2.10(a) is the uncompensated image with the initial Q model and shows strong attenuation zones (highlighted by a yellow box) within and under the two gas anomalies. These attenuated zones have dimmer amplitudes and stretched events due to the loss of high frequencies caused by attenuation. The migration used in this work tapers the events at the boundaries, so the events at 0 to 200 m and 5,800 m to 6,000 m are wiped out by this boundary condition. Figure 2.11(a) and Figure 2.11(b) are the uncompensated angle domain common image gathers at the left gas (x=1,500 m) and the right gas (x=3,800 m), respectively. As the near angles under the anomalies have more influence by the gas pockets than the far angles, the events at the near angles shown in both Figure 2.11(a) and Figure 2.11(b) are streched with low amplitudes. As attenuation disperses the velocities in a way that high frequencies of a wave travel faster than its low frequency, the events in the angles gathers as shown in Figure 2.11(a) and Figure 2.11(b) are uplifted at the near angles.

Figure 2.10(b) is the compensated image using inverted Q model as shown in Figure 2.9(c). Figure 2.11(c) and Figure 2.11(d) are compensated angle domain common image gathers at x=1,500 m and x=3,800 m, respectively. Migration with compensation using this inverted Q model compensates for the loss of the high frequencies and correct the distorted phase. Therefore, the dimming and stretched events highlighted in the attenuating region in Figure 2.10(a) and at the near angles as shown in Figure 2.11(a) and Figure 2.11(b) becomes bright and more coherent. The uplifted events at the near angles as shown in Figure 2.11(a) and Figure 2.11(b) are pushed down after phase correction by Q compensation, as a result, flattening the events in Figure 2.11(c) and Figure 2.11(d). Figure 2.12 is the windowed spectra (x=3,000 m to 4,000 m and z=500 m to 2,000 m) of the uncompensated image (blue) as shown in Figure 2.10(a) and the compensated image (red) as shown in Figure 2.10(b). Migration with Q compensation recovers the high frequencies loss of the attenuated image and broaden the spectra of the image.

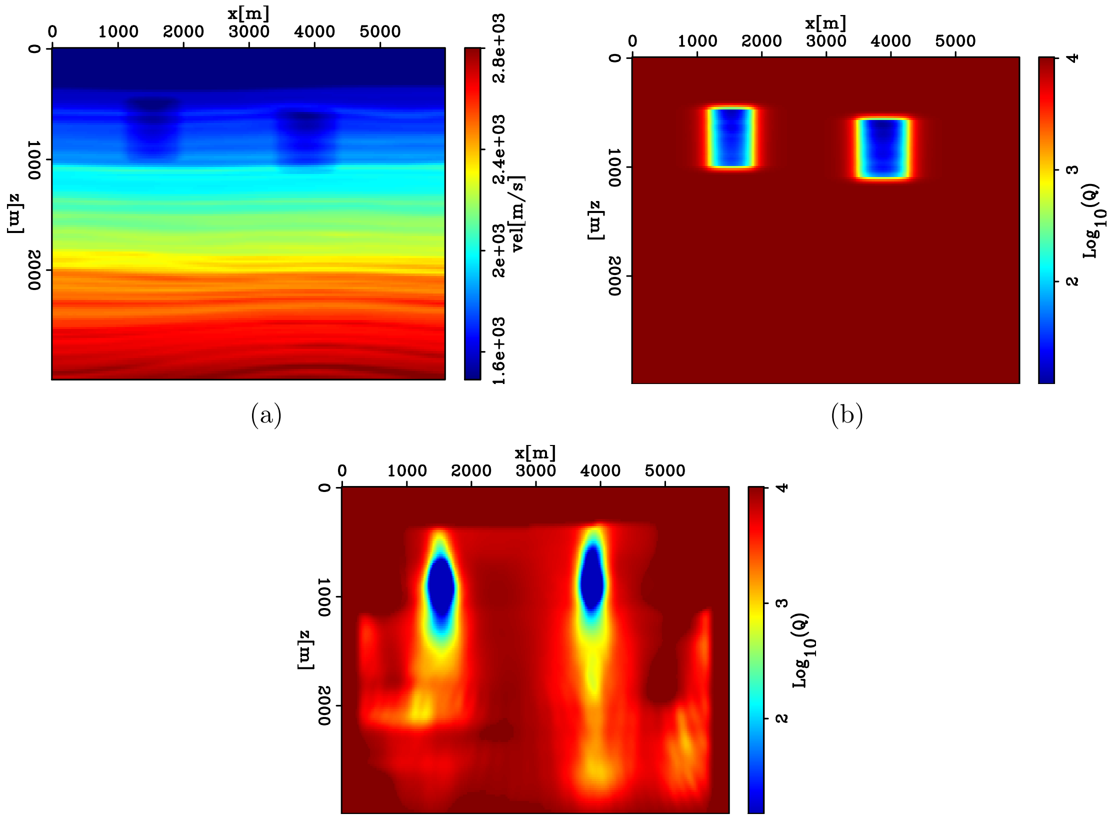

(a)

(b)

(c)

Figure 2.9: 2D SEAM model example:(a) A part of a modified SEAM velocity model with two gas clouds. (b) True Q model with two gas clouds. (c) Inverted Q model. chap2/. seam2D-vel-2gas,seam2D-Q,seam2D-tvbq-invQ

The data used in the third numerical example test is provided courtesy of Schlumberger. This example employs a dataset generated by Schlumberger (Cavalca et al., 2013) using a 2D visco-acoustic version of the 2004 BP benchmark model, courtesy

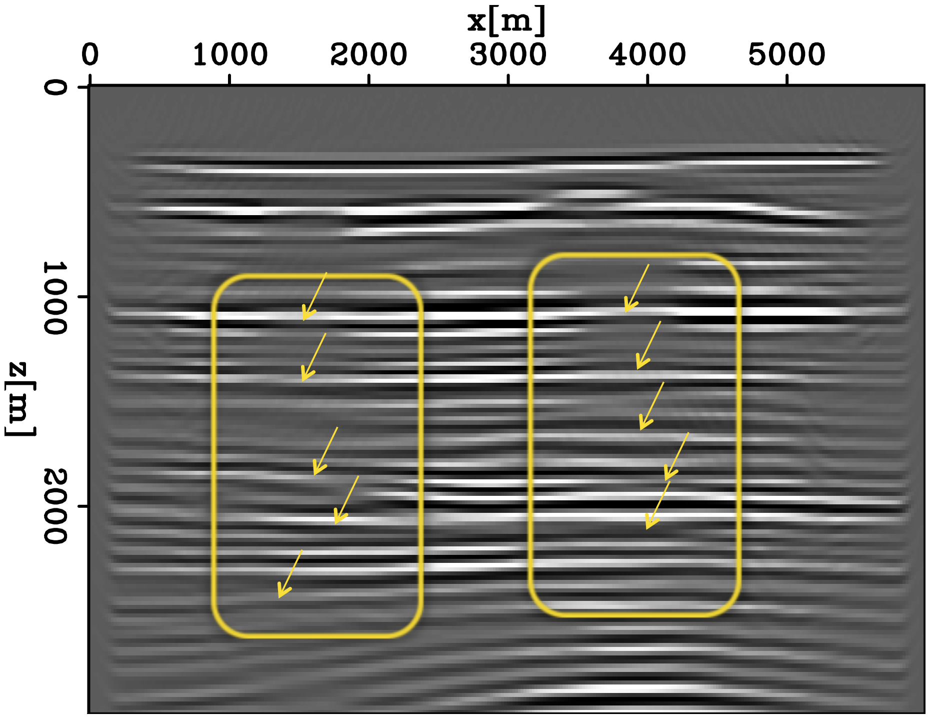

(a)

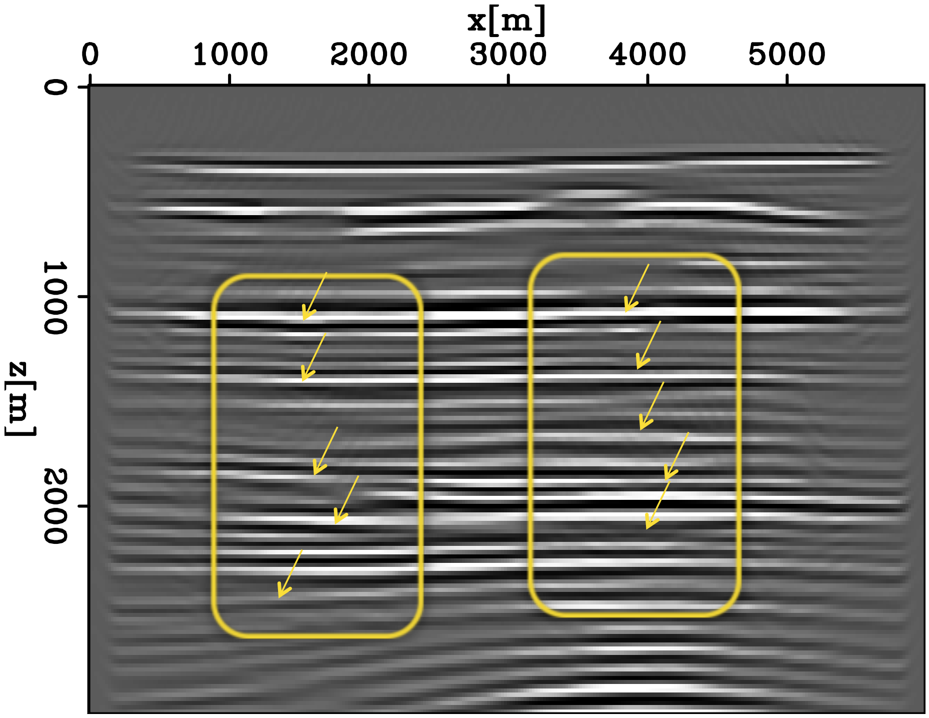

(b)

Figure 2.10: 2D SEAM model example: (a)uncompensated image using initial Q model; (b) compensated image using the inverted Q model in Figure 2.9(c). The improved events are highlighted. The improvements are especially noticeable in the boxed image. chap2/. seam2D-tvbq-bimg-ann,seam2D-tvbq-iimg-ann

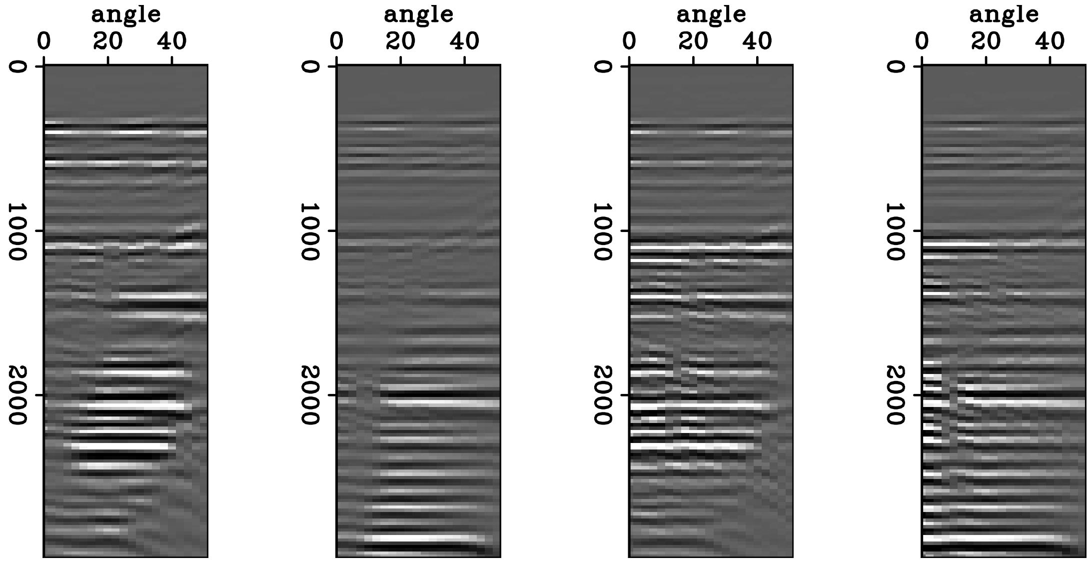

(a) (b) (c) (d)

Figure 2.11: 2D SEAM model example: (a)uncompensated angle-domain common image gather at x=1,500 m using initial Q model; (b)uncompensated angle-domain common image gather at x=3,800 m using initial Q model. (c)compensated angle-domain common image gather at x=1,500 m using the inverted Q model in Figure 2.9(c); (d)compensated angle-domain common image gather at x=3,800 m using the inverted Q model in Figure 2.9(c). chap2/. seam2D-tvbq-bang-lgas,seam2D-tvbq-bang-rgas,seam2D-tvbq-iang-lgas,seam2D-tvbq-iang-rg

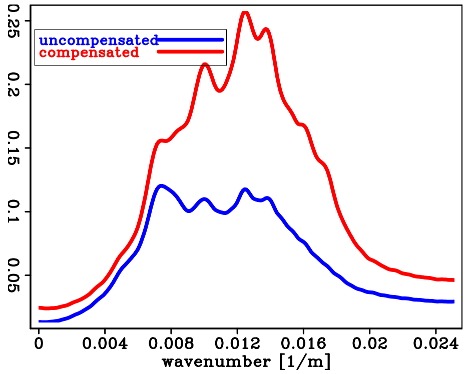

Figure 2.12: 2D SEAM model example: the windowed spectra (x=3,000 m - 4,000 m and z=500 m - 2,000 m) of the uncompensated image (blue) as shown in Figure 2.10(a) and the compensated image (red) as shown in Figure 2.10(b). chap2/. seam2D-spex

of BP (Billette and Brandsberg-Dahl, 2005). An attenuation model was added by Schlumberger to the original 2004 BP models, courtesy of Schlumberger (Cavalca et al., 2013). This Q model is not released, but its location and value has been shown by Schlumberger (Cavalca et al., 2013). The attenuation model is a space- and depth-variant absorption model made of several Q heterogeneities and a nonattenuative background (Q = 5,000). A large attenuative zone (Q = 50) is included near the left of the salt flank. In the shallow part of the model, some smaller but stronger Q heterogeneities are introduced (Q=[10, 20]). These coincide with the gas pockets associated with slow-velocity anomalies included in the original velocity model shown in Figure 2.13. The visco-acoustic surface seismic data generated by Schlumberger using a finite-difference modeling code based on Standard Linear Solid theory (Zener, 1948). In my example, 474 shots are used with 100 m spacing, and offsets ranging from -15,000 m to 15,000 m. Receivers are distributed on both sides of each shot at an increment of 25 m. As for the Q inversion, I assume I know the velocity model.

First, I use WEMQA with the one-way method to invert the Q model. The initial model for the inversion is without attenuation. Figure 2.15(a) is the migrated image at zero subsurface offset generated with the initial model. It shows the attenuated zone near the left side of the salt flank and under the gas pockets. Figures 2.14(a) and 2.14(b) show the inversion results using WEMQA from the stacked image and the prestack image, respectively. To invert for the model from the stacked gather, we analyze the attenuation effects by calculating the slope of the logarithm of the spectral ratio between the windowed events of each trace and the events in the reference window at the same depth. The window size is 1500 m wide in depth and 100 m wide in the horizontal direction, and 100 sliding windows are used for each trace. Two reference traces are selected. The image to the left side of the salt (x<41,025 m) is compared with the reference trace at x=20,450 m; while the image to the right of the salt (x>41,025 m) is compared with the reference trace at x=42,000 m. To analyze the prestack gather, we choose the angle gathers at $x = 20,450$ m as the reference to the angle gathers of which x<41,025 m, and choose the angle gathers x=42,000 m as the reference to the angle gathers of which x>41,025 m.

Figure 2.14(a) shows that the locations of the gas pockets and the attenuating zone beside the salt are well retrieved. However, the side lobes of the inverted gas pockets are very strong. With the help of the prestack gather, the inverted model in Figure 2.14(b) has slightly better resolution, and the side lobe problem around the gas pockets is mitigated. However, both results have low resolution. One main reason for the poor resolution is that tomography updates the low wavenumber components. Another explanation for the low resolution is that the effective Q is measured as an average effect within a large window, which may lower the vertical resolution of the inversion. Moreover, both methods yield significantly weaker updates for the gas between 45,000 m to 50,000 m than the bigger gas pockets on the right. Because the size of the gas pockets there is roughly the same as the wavelength, their attentuating effects are difficult to measure. In addition, the attenuating zone beside the salt is not as well retrieved as well as the gas pockets, especially for the prestack method shown in Figure 2.14(b). The steepness of the salt flank makes the one-way wave propagation fail in imaging, and it introduces artifacts and errors in the spectral analysis.

Figure 2.15(b) is the compensated image using the inverted Q model in Figure 2.14(b). The results show that the highlighted events under the well estimated shallow gas anomalies are properly compensated when compared with the attenuated image using the initial Q model shown in Figure 2.15(a). The image under the small gas has little compensation because of this region's weak updates in Q estimation. However, the image beside the salt has no compensation.

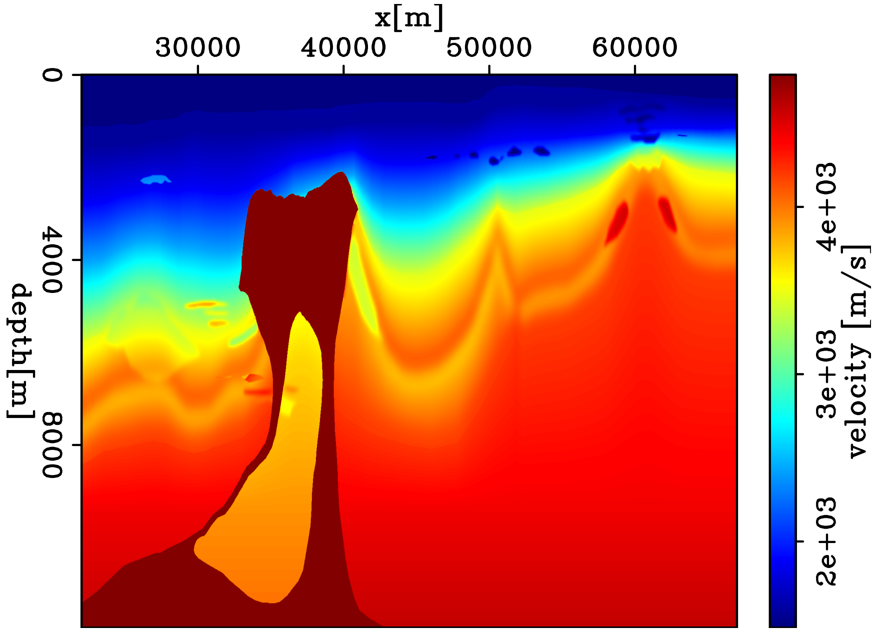

Figure 2.13: 2D BP model example: 2004 BP benchmark velocity model. chap2/. bp-vel

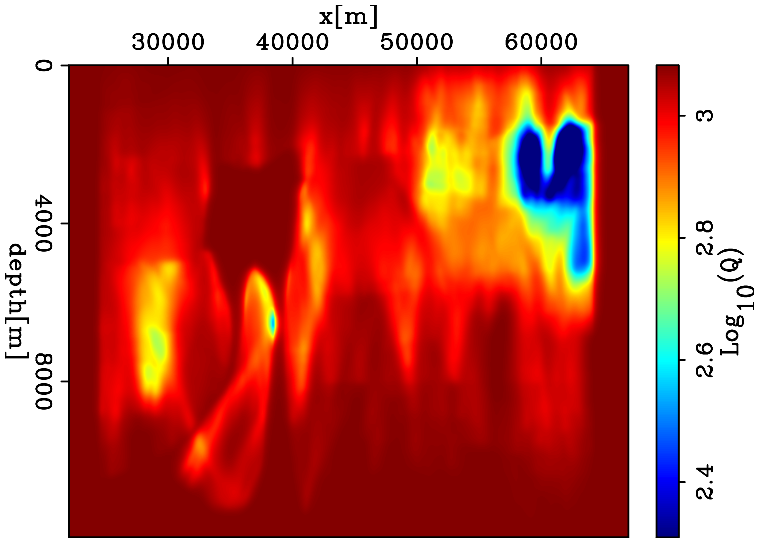

(a)

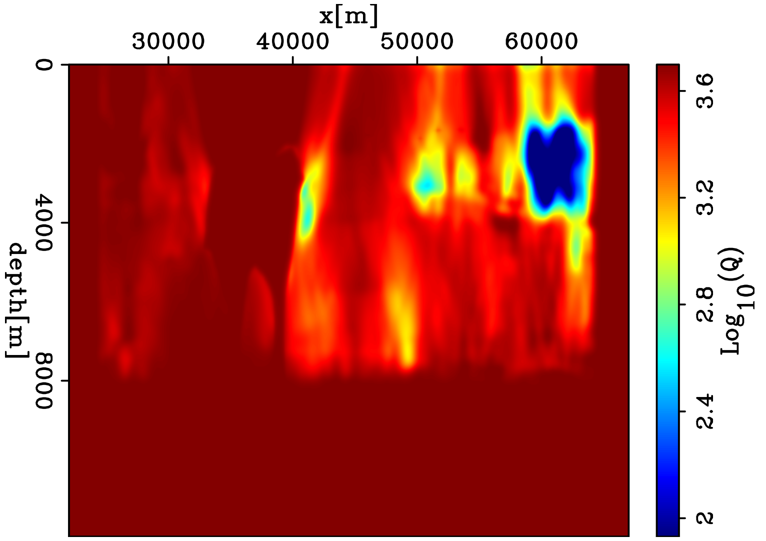

(b)

Figure 2.14: 2D BP model example: (a) the inversion results using WEMQA from the stacked image; (b) the inversion results using WEMQA from the prestack image. [**CR**] chap2/. bpNPre-bq-inv,bppstk-bq2-inv

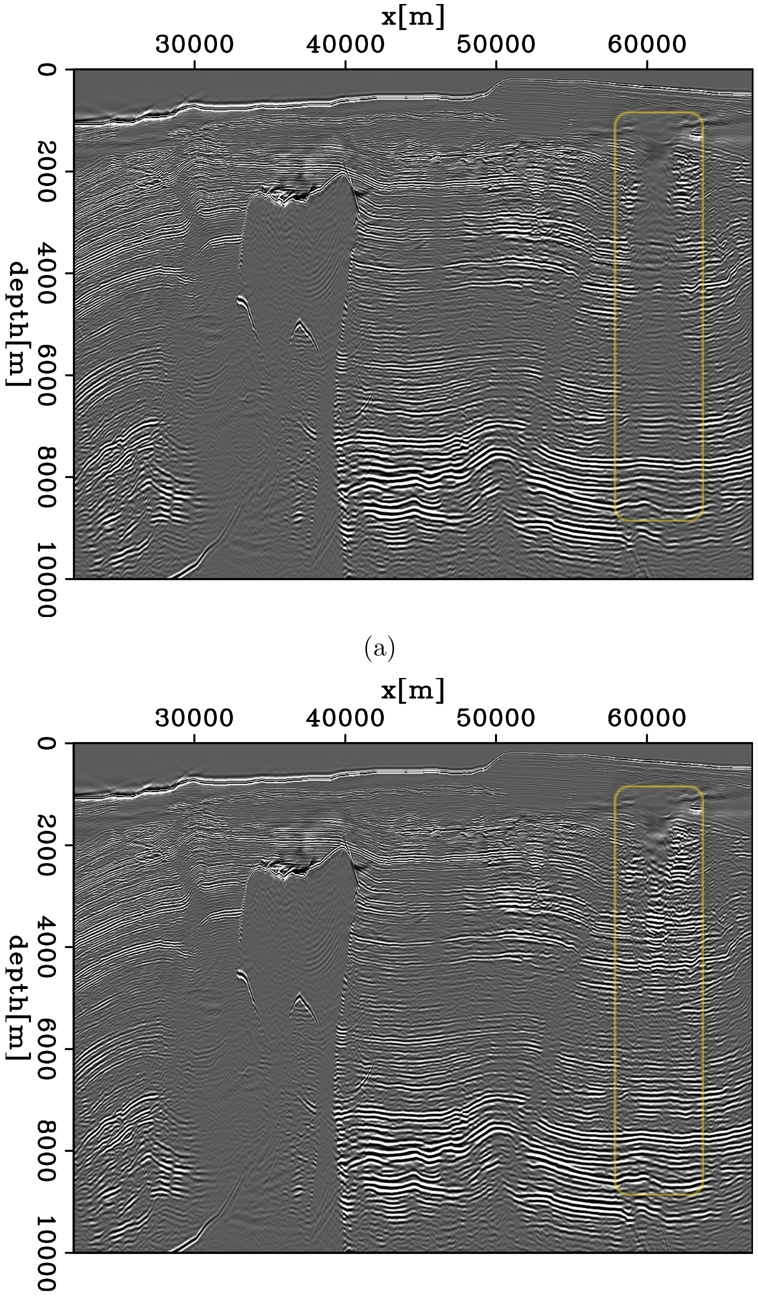

(a)

(b)

Figure 2.15: 2D BP model example: (a) the migration image at zero sub-surface offset generated with the initial model; (b) the migration image at zero sub-surface offset generated with the inverted Q model in Figure 2.14(b). [**CR**] chap2/. bp-bimg-iter0-ann,bppstk-bimg-iter10-ann

To overcome the limitation of one-way method on the steep structure (around the salt flank), I use WEMQA with the two-way method on the salt region, which has a large attenuative zone (Q = 50) near the left of the salt flank that is circled in the velocity model shown in Figure 2.16. In this example, 248 shots are used with 100 m spacing, and the offsets range from -15,000 m to 15,000 m. Receivers are distributed on both sides of each shot at an increment of 25 m. The cut-off frequency that we used to filter out the noise in the reverse-time migration was 30 Hz, which is 60% of the maximum useful frequency.

Figures 2.18(a) and 2.18(b) are the attenuated images from the viscoacoustic data using one-way and two-way Q migration with a non-attenuating model, respectively. The results show that the events beside the salt flank are attenuated in terms of the amplitude dimming, in coherency of the events, and stretching of the wavelets. Both migrations image the structure with gentle horizontal variation well. However, Figure 2.18(a) shows a poorer image around the salt flank when compared with Figure 2.18(b). The salt flank in Figure 2.18(a) is not focused. The regions beside the salt have discontinuous events and are contaminated with high-frequency noises. Figure 2.18(b) shows a sharper and clearer salt flank. The image around the salt is cleaner with less high-frequency noise and the events are more coherent. The images at the boundary of Figure 2.18(b) are tapered down by the boundary condition.

The initial model for the inversion has no attenuation. I analyze the attenuation effects by calculating the slope of the logarithm of the spectral ratio between the windowed events of each trace and the events in the reference window at the same depth. The window size is 1,500 m wide in X and 100 m wide in Z, and 100 sliding windows are used for each trace. The reference trace is the one at 24,000 m. Because the computational cost of the two-way migration is high, I compute the objective function from the stacked image to make a cost-efficient comparison between one-way and two-way methods. Both the one-way and two-way inversion used in this example use a weighting function that is multiplied by the updated gradient to prevent updates in the salt body. Figure 2.17(a) and Figure 2.17(b) are the inverted Q model using one-way and two-way WEMQA, respectively. Figure 2.17(a) fails to resolve the Q model in area beside the salt flank, because one-way propagation is not able to accurately image the reflections from the steeply dipping structure (salt flank). Figure 2.17(b) shows that a two-way method retrieves the Q model well in the reservoir region beside the salt. It is especially good in the upper part of the salt flank. However, the update has leaked into the base of the salt, because the image quality is poor there. In addition, the two-way method still fails to update the Q model adjacent to the salt flank because of the high-frequency image artifacts in that area.

Figure 2.19 is the image using two-way migration with the inverted Q model shown in Figure 2.17(b) for compensation. The results show that the image adjacent to the salt flank is not well compensated because of the weak updating of the Q model there. The events in the rest of that region are compensated. Their amplitudes are improved, they are more coherent, and their phases are corrected.

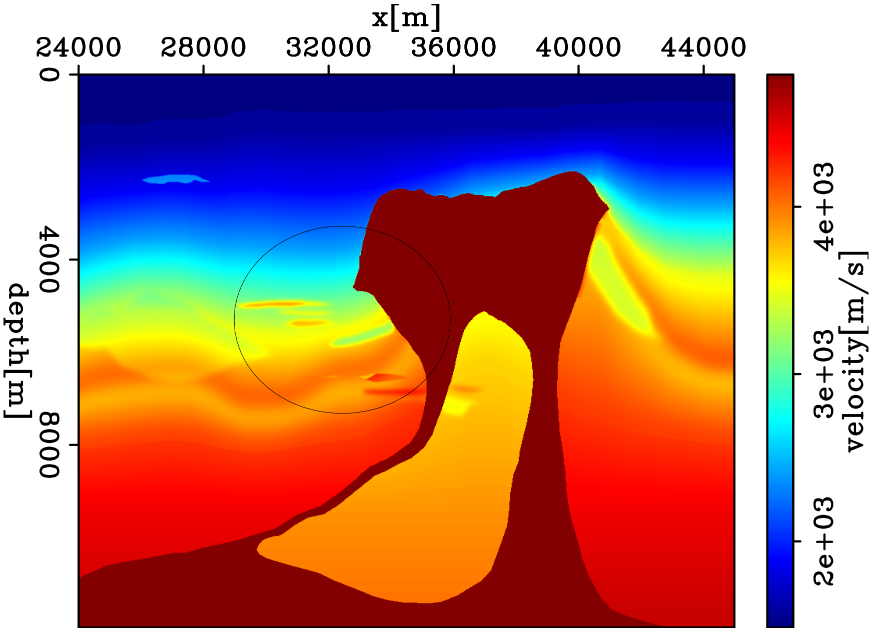

Figure 2.16: 2D BP model example: BP velocity model. The circles approximately show the location of the attenuation zone besides the salt flank, with the lowest Q value of $Q = 50$. [**ER**] chap2/. bp-vel-ann

## DISCUSSION

This chapter presents an inversion-based method –wave-equation migration Q analysis (WEMQA) – to estimate Q models from migrated images by a wave-equation tomographic operator. Its first two numerical synthetic examples show that it works well for models with gentle horizontal variation in the geological structure and for Q anomalies with simple shapes. Consequently, the migration with the estimated Q anomalies improves damped amplitudes, enhances frequency content, corrects the

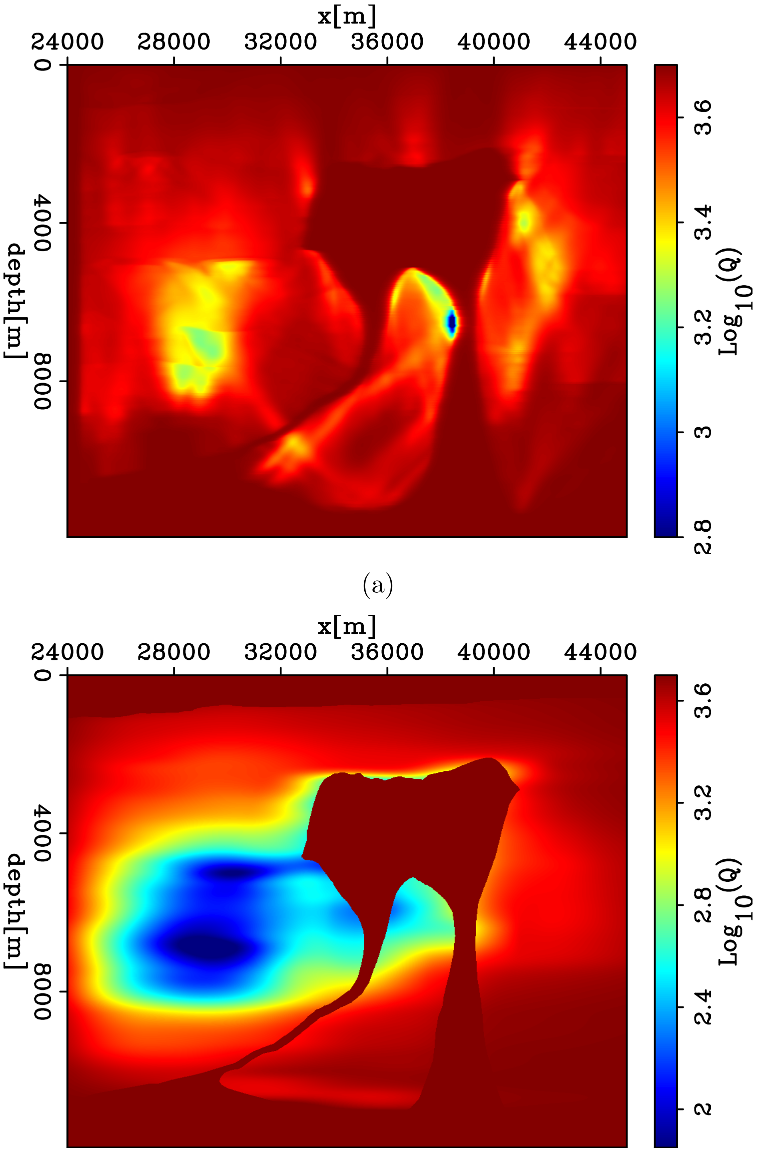

(a)

(b)

Figure 2.17: 2D BP model example: (a) the inverted Q model using one-way wave-equation migration Q analysis. The result fails to resolve the Q model in the area besides the salt flank, because one-way propagation is not able to accurately image the reflections from the steeply dipping structure (salt flank); (b) the inverted Q model using two-way wave-equation migration Q analysis. The result retrieves the Q model in the reservoir region beside the salt well. However, it still fails to update the Q model adjacent to the salt flank because of the high-frequency image artifacts in that area. [**CR**] chap2/. bp-q-one,bp-q-rtm

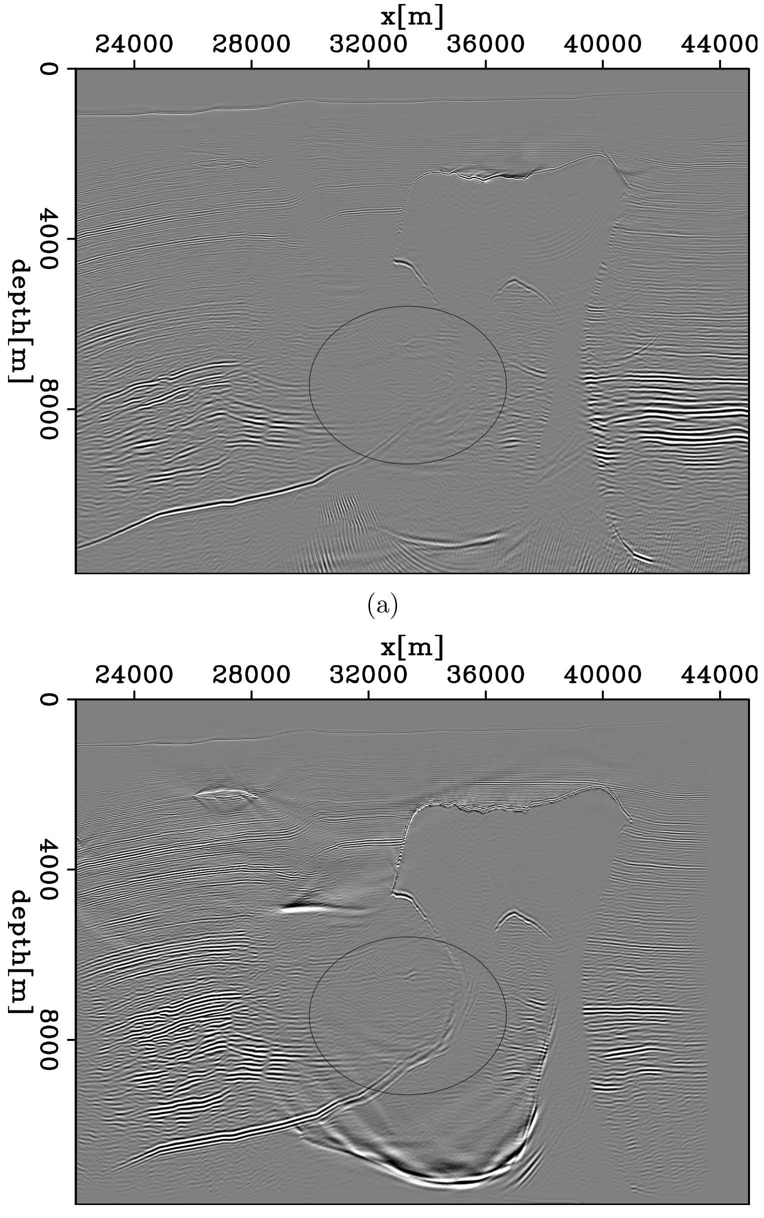

(a)

(b)

Figure 2.18: 2D BP model example: (a) 2D BP model example: attenuated images from the viscoacoustic data using one-way Q migration with a non-attenuating model. As shown in the circles, the salt flank is not focused, and the regions beside the salt have discontinued events and are contaminated with high-frequency noises; (b) attenuated images from the viscoacoustic data using two-way reverse-time Q migration with nonattenuating model. As shown in the circles, the salt flank is sharp and well-focused. The image around the salt is cleaner with less high-frequency noises, and the events becomes more coherent, when compared with Figure 2.18(a). [**CR**] chap2/. bp-img-one-ann,bp-img-rtm-ann

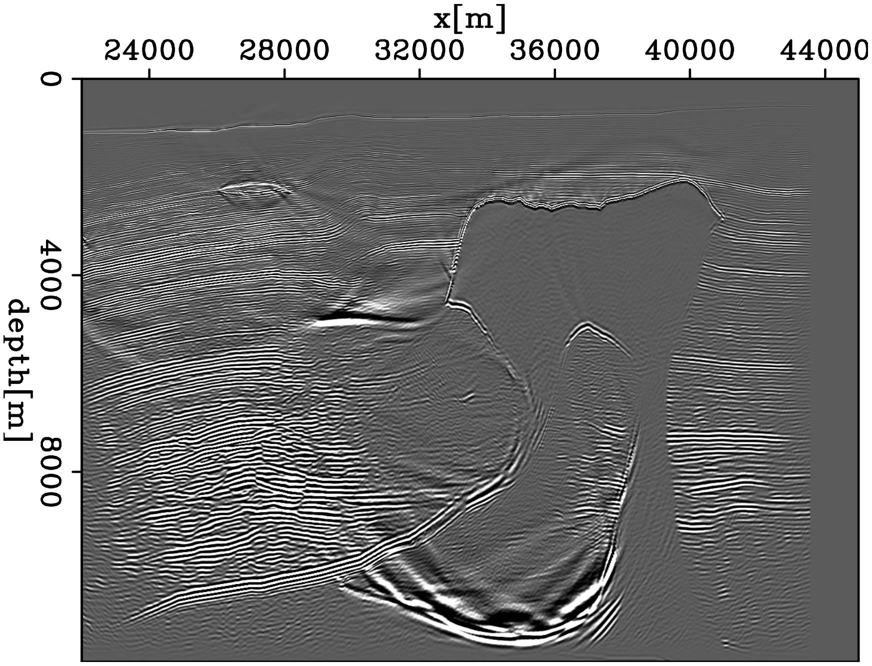

Figure 2.19: 2D BP model example: compensated image using two-way reverse-time Q migration. The result shows the image adjacent to the salt flank is not well compensated because of the weak updating of the Q model there. But the other events alongside the salt flank are compensated. [**CR**] chap2/. tst-img3

distorted phase and therefore makes events more coherent. If the Q anomalies have an irregular shape (e.g., the right Q anomaly in the third example), the prestack method results in higher resolution results than the stacked method. The prestack tomography exploits the redundancy of seismic data and better focuses the results by summing the back-projections from all angles. Once the geological structure becomes complicated, e.g., a salt body with steep salt flank exists, one must use the more computationally expensive two way method to obtain focused images, as can been seen in the third example.

However, some scenarios make WEMQA fail to yield a satisfactory Q estimation, and modifications and improvements of this methods are required. First, noise or migration artifacts introduced by the migration methods developed in this chapter (e.g., the artifacts besides the migrated salt flanks in the third example) can prevent an accurate spectral analysis for Q estimation. It is useful to apply a post-migration filter to remove the artifacts to produce a clean image. In addition, in this chapter, I assume velocity model is known and accurate. However, if the velocity is wrong, migration can not focus the image and hence distorts the image, which introduces ambiguity into the measurements of the effect of Q on the image. Also a wrong velocity model makes the correction for the velocity stretching using Equation 2.13 inaccurate. To address these issues, I present a method to both update the velocity model and Q model in a later chapter. Moreover, WEMQA is not able to recover a high-resolution Q anomaly if the anomaly has an irregular or small size. The reasons are that WEMQA uses a low wavenumber-promoting tomographic operator, and that it uses a window that is wide along depth to calculate $\rho$ (the effect of Q on the image). The window used to quantify the effect of Q on the image is wide along depth, which also lower the vertical resolution of the results. A regularization term based on the velocity model added to the objective function will be introduced in Chapter 3. The results shows that such regularization helps improve the resolution of the locations and shapes of the Q estimates.

## ACKNOWLEDGMENTS

I would like to thank Schlumberger and BP for providing the 2D synthetic dataset.

# Chapter 3

# Rock physics constrained WEMQA

## INTRODUCTION

Chapter 2 shows that WEMQA is able to estimate compressional attenuation anomalies, but the inversion results have a low resolution. In this chapter, I improve the resolution of the inverted Q model by adding a regularization term to the objective function (Equation 2.1) based on the provided compressional velocity model ($V_p$). I define $Q_p$ as the compressional quality factor in this chapter, which is the same as the variable $Q$ defined in Chapter 2.

It has been observed from field data (He and Cai, 2012; Zhou et al., 2014) that strong compressional attenuation often accompanies low compressional velocity. However, very few studies have analytically linked these two properties. Rock physics has built several models (Dvorkin et al., 2014; Muller et al., 2010) of $V_p$ and $Q_p$ based on other rock properties (e.g., porosity, saturation, and mineralogy), which may implicitly quantify the relation between these two parameters. However, these existing models for $V_p$ and $Q_p$, based on rock physics properties, only provide an estimate of these two parameters at the well. A model that provides an analytic relation between $V_p$ and $Q_p$ would allow us to approximately relate $Q_p$ to $V_p$ without going through direct rock physics modeling, which would not be constrained by location. Such a relation can be used as the constraint/regularization term in the seismic inversion and in turn would improve the accuracy of the seismic inversion of $V_p$ and $Q_p$.

In this study, I first derive an approximate closed-form solution directly relating $V_p$ to $Q_p$ using rock physics modeling. Next, I validated this relation using field well data. Finally, I applied this new $Q_p$-$V_p$ equation to synthetic seismic data, resulting in an improved $Q_p$ model. I used this approach to improve the $Q_p$ model as well as seismic imaging using field seismic data.

## DERIVING THE CLOSED-FORM SOLUTION TO RELATE $V_P$ TO $Q_P$ USING ROCK PHYSICS MODELING

**Modeling seismic attenuation.** Seismic attenuation primarily occurs either at a gas reservoir or in the presence of shallow gas pockets. Wave-induced variations of pore pressure in the partially saturated rock results in oscillatory fluid flow. The viscous losses during this oscillatory fluid flow cause elastic energy dissipation and wave attenuation. The frequency of measurements may span a broad range (e.g., ultrasonic pulse transmission experiments, sonic wellbore data, and seismic reflection data). This results in a wide range of the sampling scale, meaning that I can only detect a certain scale of heterogeneity depending on frequency. This range of scales can be categorized as macroscopic and microscopic based on the spatial resolution. Macroscopic wave-induced fluid flow, as opposed to microscopic fluid flow, is engaged at the seismic exploration frequency range, and is likely to be the main mechanism for the fluid-related seismic attenuation in seismic data.

Seismic attenuation for compressional wave, quantified by the quality factor $Q_p$, is a function of frequency. According to the standard linear solid model, I can relate $Q_p$ to the velocity-frequency (or modulus-frequency) dispersion. The resulting equation (Dvorkin et al., 2014) for the maximum inverse quality factor $Q_{p\max}^{-1}$ is

$$Q_{p\max}^{-1} = \frac{M_\infty - M_0}{2\sqrt{M_\infty M_0}}, \tag{3.1}$$

where $M_0$ is the compressional modulus at very low frequency and $M_\infty$ is the compressional modulus at very high frequency. The compressional modulus is the product of the bulk density and P-wave velocity squared. This equation provides the upper bound for attenuation without addressing its frequency dependence. In this work I will use $Q_{p\max}^{-1}$ by assuming that this is the inverse quality factor of interest, relevant to the seismic frequency.

According to Dvorkin et al. (2014), in partially saturated rock, viscoelastic effects and attenuation may arise from the oscillatory liquid cross-flow between fully liquid-saturated patches and the surrounding rock with partial gas saturation. The reaction of rock with patchy saturation to loading by the elastic wave depends on the frequency. If it is low and the loading is slow, the oscillations of the pore pressure in a fully liquid-saturated patch and partially saturated domains next to it are equilibrating. The patch is relaxed. For this case, to compute the low-frequency modulus $M_0$, I used the Vp-only approximation (Mavko et al., 1995) to fluid substitution equation (Gassmann, 1951) for the compressional modulus of the partially saturated rock as follows:

$$M_0 = M_S \frac{\phi M_{Dry} - (1+\phi) K_F M_{Dry}/M_S + K_F}{(1-\phi)K_F + \phi M_S - K_F M_{Dry}/M_S}, \tag{3.2}$$

where $M_S$ is the compressional modulus of the mineral phase, $M_{Dry}$ is the compressional modulus of the dry frame of the rock whose pore fluids have been fully evacuated, $\phi$ is the total porosity, and $K_F$ is the effective bulk modulus of the fluid in the rock computed as the harmonic average of those of water and gas.

Conversely, if the frequency is high and the loading is fast, the resulting oscillatory variations of pore pressure cannot equilibrate between the fully saturated patch and the domain outside it. The patch is unrelaxed. At high frequency, I can use the patchy saturation equation (Mavko et al., 2009), which expresses the unrelaxed compressional modulus as the harmonic average of the compressional moduli of the wet rock $M_W$ and rock with only gas $M_G$:

$$\frac{1}{M_\infty} = \frac{S_W}{M_W} + \frac{1-S_W}{M_G}, \tag{3.3}$$

where

$$\begin{aligned} M_W &= M_S \frac{\phi M_{Dry} - (1+\phi) K_W M_{Dry}/M_S + K_W}{(1-\phi)K_W + \phi M_S - K_W M_{Dry}/M_S}; \\ M_G &= M_S \frac{\phi M_{Dry} - (1+\phi) K_G M_{Dry}/M_S + K_G}{(1-\phi)K_G + \phi M_S - K_G M_{Dry}/M_S}, \end{aligned} \tag{3.4}$$

where $K_W$ and $K_G$ are the bulk modulus of water and gas, respectively, and $S_W$ is the water saturation.

**Modeling velocity.** Here I compute the compressional-wave velocity of rock from the low-frequency compressional modulus $M_0$ and the bulk density $\rho$ as

$$V_p = \sqrt{\frac{M_0}{\rho}}. \tag{3.5}$$

This assumption implies that the compressional modulus for compressional-wave velocity is independent of the frequency, while the compressional modulus in Equation 3.1 for $Q^{-1}_{p\,\max}$ is dependent of the frequency. In spite of this, I feel that this assumption is justified since small modulus versus frequency dispersion can produce substantial attenuation but produce minor changes of compressional-wave velocity. For example, if $M_0$ is 18 GPa and $M_\infty$ is 20 GPa, the inverse quality factor is about 0.05 and the quality factor itself is 20 with the realtive velocity dispersion only about 5%.

$M_0$ is a function of $M_{Dry}$. The previous studies, e.g. by Raymer et al. (1980); Dvorkin and Nur (1996), built rock physics models to compute $M_{Dry}$ from other parameters. However, these models do not provide a simple analytical equation suitable for our goal. Based on the idea that as the porosity increases, the rock becomes softer and its modulus decreases, and that the porosity-related changes in the elastic modulus should be proportional to $\phi$, I propose a new model in this study for $M_{Dry}$ using a simple equation:

$$\frac{M_{Dry}}{M_S - M_{Dry}} = \frac{\alpha_{Dry}}{\phi}, \tag{3.6}$$

where $\alpha_{Dry}$ is positive. Although $\alpha_{Dry}$ is not a directly measurable rock parameter, it can be computed by fitting Equation 3.6 to the porosity and dry modulus $M_{Dry}$. The combination of different values of $\alpha_{Dry}$ and porosity contributes to different results of dry modulus $M_{Dry}$. As shown in Figure 3.1, large $\alpha_{Dry}$ acts to gently increase the difference $M_S - M_{Dry}$ with increasing porosity. As a result, at fixed porosity, the dry-rock modulus for larger $\alpha_{Dry}$ is larger than that for a smaller $\alpha_{Dry}$.

This seemingly simplistic form was, in fact, used earlier by Geertsma and Smit (1961) to relate the dry-rock bulk modulus $K_{Dry}$ to that of the solid matrix $K_S$ and porosity $\phi$:

$$\frac{K_{Dry}}{K_S - K_{Dry}} = \frac{1}{50\phi}, \tag{3.7}$$

which gives $\alpha = 0.02$ for the bulk modulus. I do not plot this equation in Figure 3.1 as I am concerned with the compressional-wave velocity and, hence, the compressional modulus.

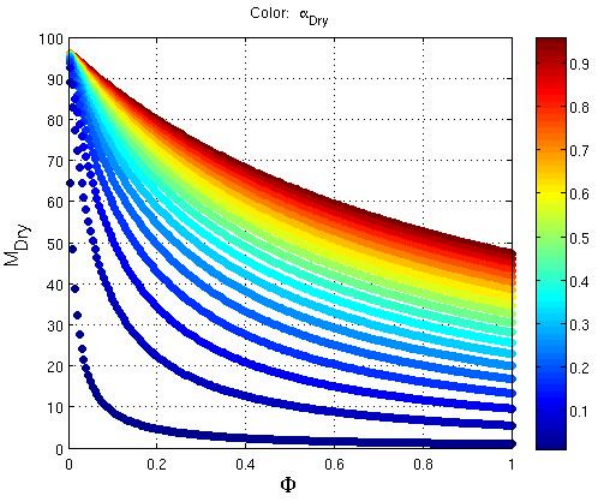

Figure 3.1: Equation 3.6 curves for $M_{Dry}$ as a function of $\phi$ and $\alpha_{Dry}$ with $M_S = 96.6$ GPa. [**NR**] $\boxed{\text{chap3/. P-Mdry}}$

**Linking seismic attenuation to velocity: A closed-form solution.** Both $V_p$ and $Q_p$ are functions of a number of rock properties: $M_{Dry}$, $M_S$, $S_W$, $\phi$, $K_W$, $K_G$, and $\rho$. Because I use Equation 3.6 to relate $M_{Dry}$ to $\phi$ and $M_S$, I only vary the remaining six variables $M_S$, $S_W$, $\phi$, $K_W$, $K_G$, and $\rho$.

The ranges of input variations are listed in Table 5.1. When testing the sensitivity of $V_p$ and $Q_p$ to these inputs, I vary one of them while assuming that the rest are constant, equal to their mean values as listed in Table 5.1.

Table 3.1: Ranges of the rock properties used in sensitivity analysis.

| Rock properties | Minimum value | Maximum value | Mean value |
|---|---|---|---|
| $K_W$ (GPa) | 2.20 | 2.80 | 2.50 |
| $K_G$ (GPa) | 0.015 | 0.035 | 0.025 |
| $M_S$ (Gpa) | 80.00 | 100.00 | 90.00 |
| $\rho$ (g/cc) | 1.80 | 2.60 | 2.20 |
| $\phi$ | 0.10 | 0.40 | 0.25 |
| $S_W$ | 0.10 | 0.50 | 0.30 |

Figure 3.2 shows the results of our sensitivity analysis. In this figure I plot sensitivity curves showing the influence of perturbations in the input rock properties on changes in $V_p$ and $Q_p$. Water saturation is the input that influences $Q_p$ the most.

However, because I only explore the rock behavior at partial saturation, $V_p$ is practically insensitive to $S_W$. The input that simultaneously influences $V_p$ and $Q_p$ the most is the porosity. Because in a clean thick reservoir $S_W$ arguably varies only in relatively thin zones at the top and bottom, I can assume $S_W$ constant thus eliminating it from the input list and concentrate solely on the effect of porosity.

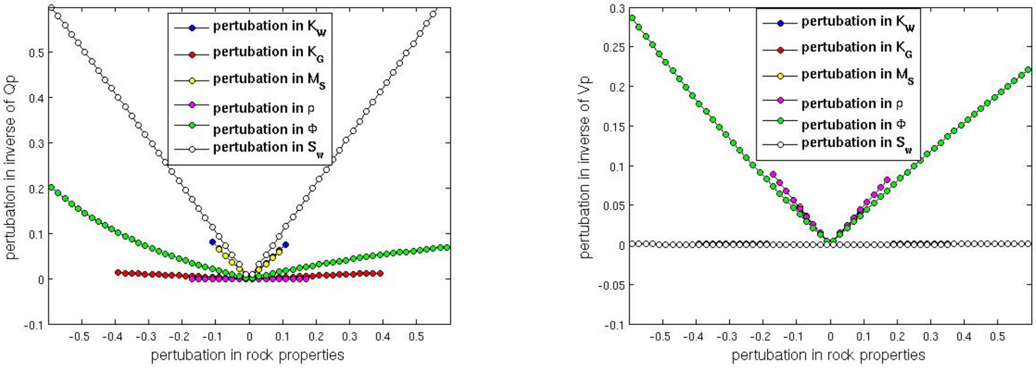

(a) (b)

Figure 3.2: The sensitivity of $Q_p$ (left) and $V_p$ (right) to changes in the rock properties ($M_S$, $S_W$, $\phi$, $K_W$, $K_G$, $\rho$). The ranges and mean values of these inputs are listed in Table 5.1. [**NR**] chap3/. P-sen-Qp-noMdry,P-sen-Vp-noMdry

In Figure 3.3, I plot $1/V_p$ and $1/Q_p$ versus porosity while keeping all other inputs constant (as listed in the caption to Figure 3.3). Porosity $\phi$ is the fraction of open space in the entire rock. Increasing this space acts to soften the rock and decrease its elastic moduli, which makes the compressional velocity, computed according to Equations 3.5 and 3.6, decrease as well (lower panel in Figure 3.3). The same is true for $Q_p$, as shown in Figure 3.3, top, computed according to Equations 3.1 and 3.6. Because of this strong effect of porosity on both velocity and attenuation, I link $V_p$ to $Q_p$ by way of $\phi$.

Specifically, I first use Equation 3.6 to express $M_{Dry}$ through $\phi$. Next, I use Equation 3.2 to express $M_0$ through $\phi$ and Equations 3.3 and 3.4 to express $M_\infty$ through $\phi$. Finally, I use Equation 3.5 to relate $V_p$ to $\phi$ and Equation 3.1 to directly relate $Q_{p\max}^{-1}$ to $V_p$. To further simplify this final equation, I assumed $M_\infty = M_0(1+\Delta)$ and use Taylor expansion to reduce the high order of $\Delta$. The final expression is

$$Q_p^{-1} = \frac{1}{2}\frac{c_1 V_p^{-2}}{c_2 V_p^{-2} + c_3} - \frac{1}{2}, \tag{3.8}$$

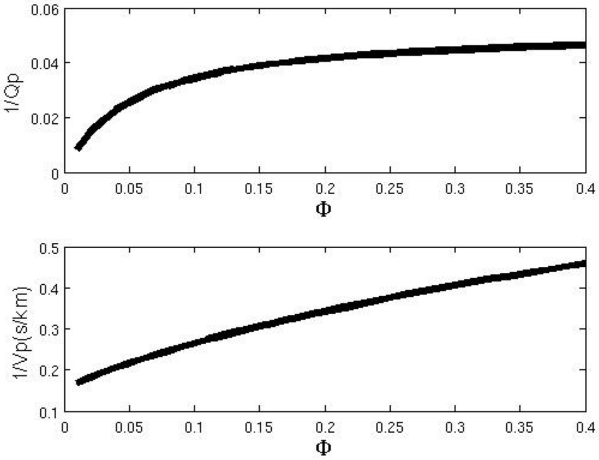

Figure 3.3: $Q_p$ (top) and $V_p$ (bottom) versus $\phi$, with $K_W = 2.4413$ GPa; $K_G = 0.0226$ GPa; $M_S = 96.6$ GPa; $\rho = 2.27$ g/cc; $\alpha_{Dry} = 0.05$, and $S_W = 0.3$. [**NR**] chap3/. P-Phi

where

$$\begin{aligned}
c_1 &= (\alpha_{Dry} + \alpha_W)(\alpha_{Dry} + \alpha_G);\\
c_2 &= S_W(\alpha_{Dry} + \alpha_F)(\alpha_{Dry} + \alpha_G) + (1 - S_W)(\alpha_{Dry} + \alpha_F)(\alpha_{Dry} + \alpha_W);\\
c_3 &= \frac{\rho}{M_S}\left(S_W(\alpha_{Dry} + \alpha_F)(\alpha_W - \alpha_G) + (\alpha_{Dry} + \alpha_W)(\alpha_G - \alpha_F)\right),
\end{aligned} \tag{3.9}$$

and

$$\begin{aligned}
\alpha_F &= \frac{K_F}{(M_S - K_F)};\\
\alpha_G &= \frac{K_G}{(M_S - K_G)};\\
\alpha_W &= \frac{K_W}{(M_S - K_W)}.
\end{aligned} \tag{3.10}$$

Equation 3.8 can also be expressed in the form of $f(Q_p)$ that $f(Q_p) = 0$, where

$$f(Q_p) = Q_p^{-1} - \frac{1}{2}\frac{c_1 V_p^{-2}}{c_2 V_p^{-2} + c_3} + \frac{1}{2}. \tag{3.11}$$

Figure 3.4 shows the relation between $1/V_p$ and $1/Q_p$ using the exact and simplified equations. The solid circles are for the exact relation using Equations 3.1 and 3.5, while the open circles are for the simplified Equation 3.8. These two curves are close to each other, especially so at small porosity. From these results, I observe that the decrease of the compressional velocity corresponds to strong attenuation, in accordance with the observation from field data with gas-related anomalies.

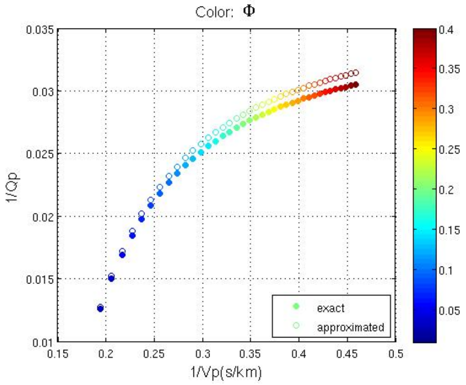

Figure 3.4: $1/V_p$ versus $1/Q_p$, with $K_W = 2.4413$ GPa; $K_G = 0.0226$ GPa; $M_S = 96.6$ GPa; $\rho = 2.27$ g/cc; $\alpha_{Dry} = 0.05$; and $S_W = 0.3$. [**NR**] chap3/. P-QV

## VALIDATING THE CLOSED-FORM SOLUTION USING WELL DATA

I use a gas-well log data to validate our theory. The black curves shown in Figure 3.5 are the measured rock properties, except for $Q_p$. The last track in Figure 3.5 shows $1/Q_p$ according to Equation 3.1 (black curve). The well has low water saturation at depths between 1.25 and 1.27 km and 1.31 and 1.32 km, indicating gas sand. I observe that both $V_p$ and $Q_p$ are small in these gas intervals.

In order to find $\alpha_{Dry}$, I first computed the dry-rock compressional modulus using the Gassmann-Mavko ($V_p$ only) fluid substitution (Mavko et al., 1995). Then I computed the same modulus but now using Equation 3.6 for varying $\alpha_{Dry}$ (Figure 3.6(a)). I found that $\alpha_{Dry} = 0.05$ gives the best fit between the moduli computed using these two different equations.

Next, I computed $Q_p$ for the gas sand using Equation 3.1 where I assume $M_\infty = M_0(1 + \Delta)$ and use Taylor expansion to reduce the high order of $\Delta$ and use $M_{Dry}$ according to Equation 3.6 for $\alpha_{Dry} = 0.05$. The resulting inverse quality factor is shown as red curve in the last track in Figure 3.5. This approximate inverse quality factor is very close to the exact solution.

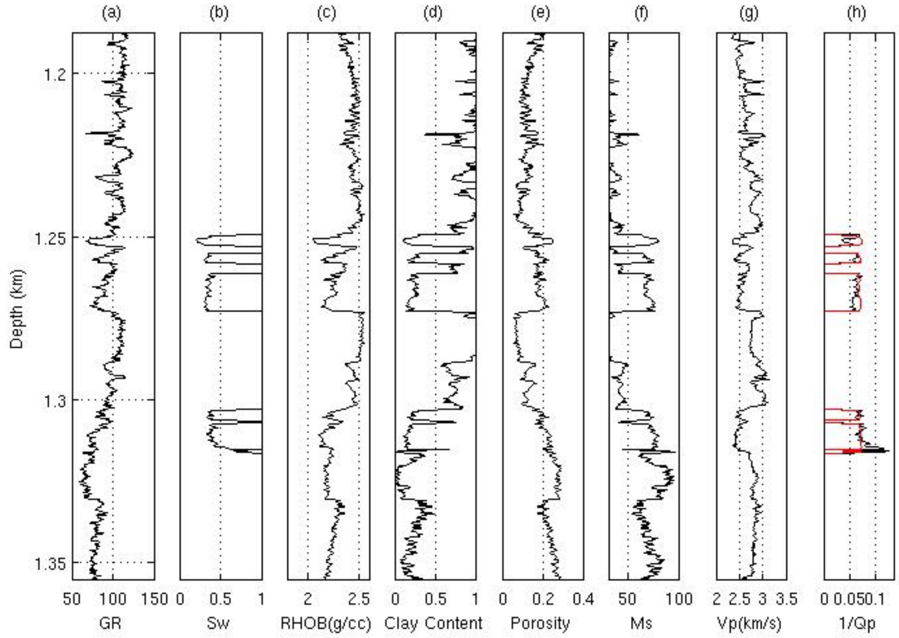

Figure 3.5: Well data used to verify our approximate relations. The curves are explained in the text. [**NR**] chap3/. P-log

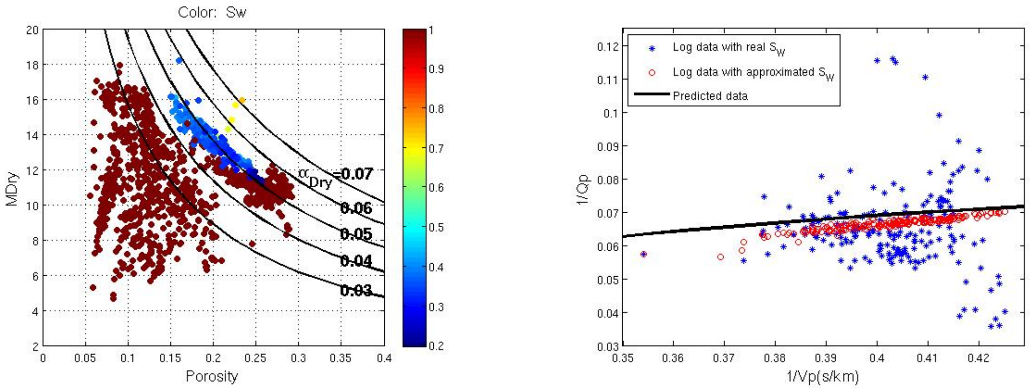

(a) (b)

Figure 3.6: (a) $M_{Dry}$ in the well (gas sand is represented by blue symbols) and constant $\alpha_{Dry}$ curves. (b) The inverse quality factor versus inverse velocity as explained in the text. [**NR**] chap3/. P-Mdry-log,P-QV-log

Figure 3.6(b) shows the resulting relation between $1/V_p$ and $1/Q_p$. The blue dots are the log data. The scatter in these data is analytically reduced by assuming constant water saturation $S_W = 0.37$ and conducting relevant fluid substitution (red dots in Figure 3.6(b)). The resulting trend (black curve) is fairly close to our approximate solution according to Equation 3.8. It only slightly overestimates the direct computation results.

## SEISMIC APPLICATION

I proposed WEMQA method in Chapter 2 that iteratively updates the $Q_p$ model and compensates the image. In this section, I apply the approximate analytical relation (Equation 3.11) to WEMQA as its model constraint to reliably invert for the $Q_p$ models with additional information. The new objective function becomes as follows:

$$J = \frac{1}{2}\sum_{\mathbf{x}} \rho(\mathbf{x}; Q) + \lambda \frac{1}{2}\sum_{\mathbf{x}} f(\mathbf{x}; Q) \tag{3.12}$$

where $\lambda$ is a scalar to balance the relative strength of the objectives.

To demonstrate its effectiveness, I first test it on a 2D synthetic example. Later, I test this method on a 2D field data from the Gulf of Mexico (GOM). CGG Services (U.S.) Inc., Houston, Texas and Shell Global Solutions International B.V. granted me permission to publish the field results in my thesis. Seismic data images provided courtesy of CGG Services (U.S.) Inc., Houston, Texas. The assumptions in both applications are that the velocity models for $Q_p$ inversion is correct.

**2D Synthetic application.** I forward modeled a synthetic seismic dataset using the $V_p$ and $Q_p$ models presented in Li et al. (2015), as shown in Figure 3.7. Li et al. (2015) built the synthetic models based on the shallow unconsolidated sand reservoir model in Wang et al. (2013). A shallow gas pocket with 70% gas saturation and low velocity and high attenuation is located in the upper part of the second layer. Its porosity and gas saturation are shown in Figure 3.8(a) and 3.8(b) respectively. The shallow shale porosity in Figure 3.8(a) is arbitrarily assumed to be very small and unrelated to the velocity model. This assumption has no impact on our study since I do not use the porosity in the shale for our $Q_p$ computations.

To generate synthetic seismic data, I employed one-way downward continuation

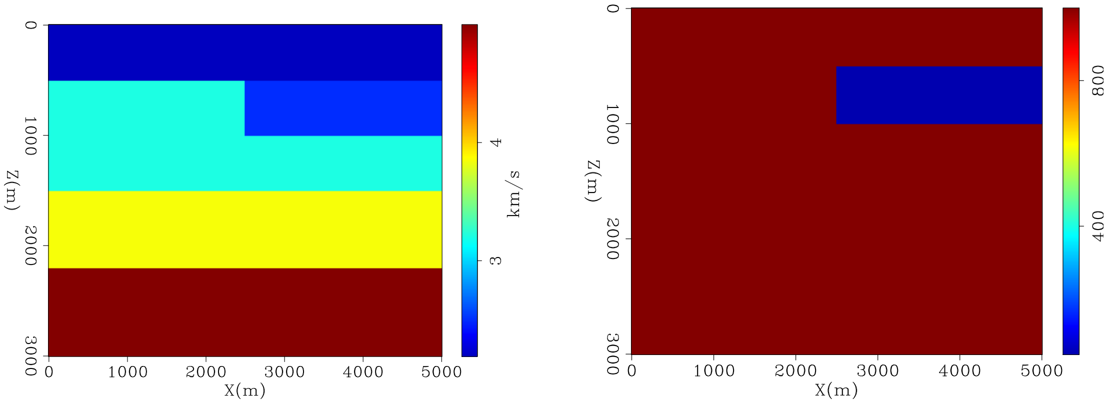

(a) (b)

Figure 3.7: (a) The true synthetic $V_p$ model. (b) $Q_p$ model. [**ER**] chap3/. layer4-vel,layer4-q

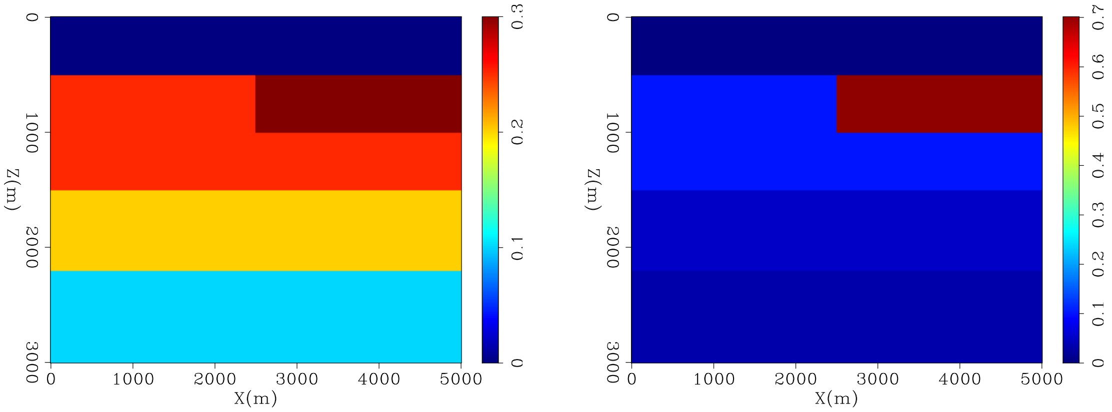

(a) (b)

Figure 3.8: (a) Porosity model. (b) Gas saturation model. [**ER**] chap3/. layer4-poro,layer4-satu

presented in Chapter 2 using $V_p$ and $Q_p$ models in Figure 3.7 with 53 sources and 801 receivers uniformly distributed on the surface. A Ricker wavelet with 20 Hz central frequency was used as the source wavelet, and the density model for this example was assumed to be spatially constant. Migration with downward propagation has the adequate ability for handling this model with little complexity.

I first inverted for the $Q_p$ model shown in Figure 3.7(b) using the objective function (Equation 2.1) in Chapter 2 with spatially constant $Q_p = 10^5$ as the initial model. The resulting $Q_p$ model (Figure 3.9(a)) highlights the area with high attenuation. However, the sparse reflectors and the limitation of this method result in low resolution and distorted shape of the resulting $Q_p$ model, especially so in the vertical direction.

To improve the inversion, I used the new objective function (Equation 3.12) presented in this chapter. If I know the rock properties at every location in the subsurface of this field, I could calculate the coefficients of $c1$, $c2$ and $c3$ for each subsurface location and estimate a $Q_p$ model using Equation 3.8. In practice, however, the rock properties in the subsurface are usually unknown. Therefore, I propose to estimate only one set of $c1$, $c2$ and $c3$ from one representative (or several) location in the field as an average value for the whole field. This set of coefficients allows us to approximate a representative relation of $Q_p$ and $V_p$ of this field using Equation 3.8, and to estimate a more accurate $Q_p$ model by regularizing the inversion workflow using this approximated relation of $Q_p$ and $V_p$. Sometimes, it is possible for us to measure the rock properties at several locations in the field by analyzing the available drilled wells. It is also possible that we have no well log data to calculate the coefficients for Equation 3.8. In this case, I have to subjectively assign a set of rock properties to the field from a reasonable analysis and interpretation from any available information related to this field. In this synthetic example, I assume a well has been drilled through the location at $x = 1,000$ m. I estimated a set of rock properties at the location of $x = 1,000$ m, $z = 1,000$ m (closed to the gas) from the well log as a representative to approximate the relation of $Q_p$ and $V_p$ of this field. These rock properties are $K_W = 2.4413$ GPa; $K_G = 0.0226$ GPa; $M_S = 96.6$ GPa; $\rho = 2.27$ g/cc; $\alpha_{Dry} = 0.05$; and $S_W = 0.1$. As a result, the coefficients for Equation 3.8 are $c1 = 0.0038$, $c2 = 0.0037$, $c3 = 2.9886 * 10^{-6} s^2/km^2$. Figure 3.9(b) is the inverted $Q_p$ model with constraint of the approximated relation in Equation 3.8. This new improved model more accurately reproduces the true model shown in Figure 3.7(b) than the inverted $Q_p$ model without constraint (Figure 3.9(a)).

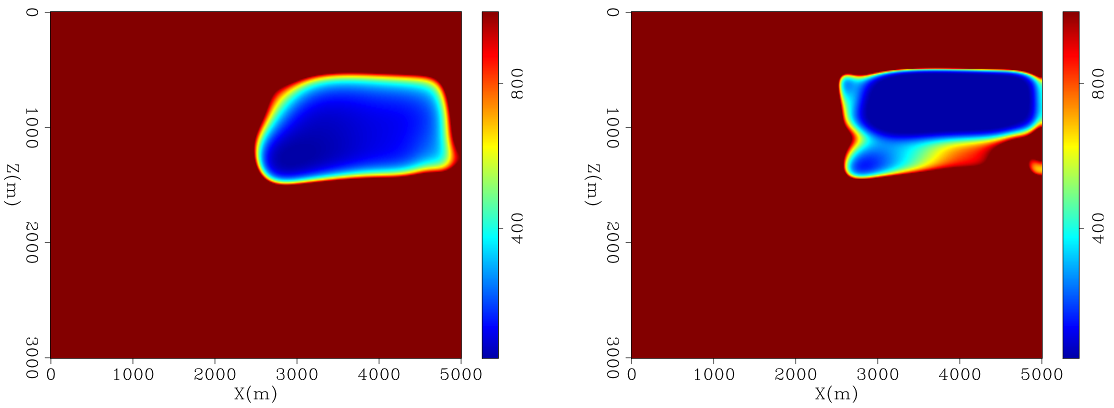

(a) (b)

Figure 3.9: (a) Inverted $Q_p$ model without constraint. (b) Inverted $Q_p$ model with constraint, with the parameters for gas sand (Equation 3.8): $c1 = 0.0038$, $c2 = 0.0037$, $c3 = 2.9886 * 10^{-6} s^2/km^2$. [**CR**] chap3/. layer4-nc-bqtv-invq,layer4-vc-bqtv-invq

Figure 3.10(a) is the migration image without knowing the correct $Q_p$ model for the gas sand. The events beneath the gas sand are attenuated as expressed by the dimming amplitude, as well as stretched and distorted wavelets. Figure 3.10(b) is the migration image compensated using the inverted $Q_p$ model as shown in Figure 3.9(a). The events beneath the gas sand in Figure 3.10(b) have brighter amplitudes and tighter wavelets due to the amplitude and frequency recovery by compensation. However, these events are still under compensation, when compared with the reference migration image in Figure 3.10(d) that is migrated using the true $Q_p$ model as shown in Figure 3.7(b). Figure 3.10(c) is the migration image compensated using the improved inverted $Q_p$ model as shown in Figure 3.9(b). The results show that compensation adequately restores both the amplitude and frequency of the events below the gas sand (the sharpness of the image), when compared with the reference migration image in Figure 3.10(d).

**2D field application.** The GOM data used in this study show a strong absorptive body in the shallow subsurface that acts to mute the deeper reflections as shown in Figure 3.11(a), where I display a zero subsurface offset image of the prestack-migrated 2D section. CGG Services (U.S.) Inc., Houston, Texas and Shell Global Solutions International B.V. granted me permission to publish the field results in my thesis. Seismic data images provided courtesy of CGG Services (U.S.) Inc., Houston, Texas. This migration was conducted without $Q_p$ compensation (assuming $Q_p = 100,000$ in

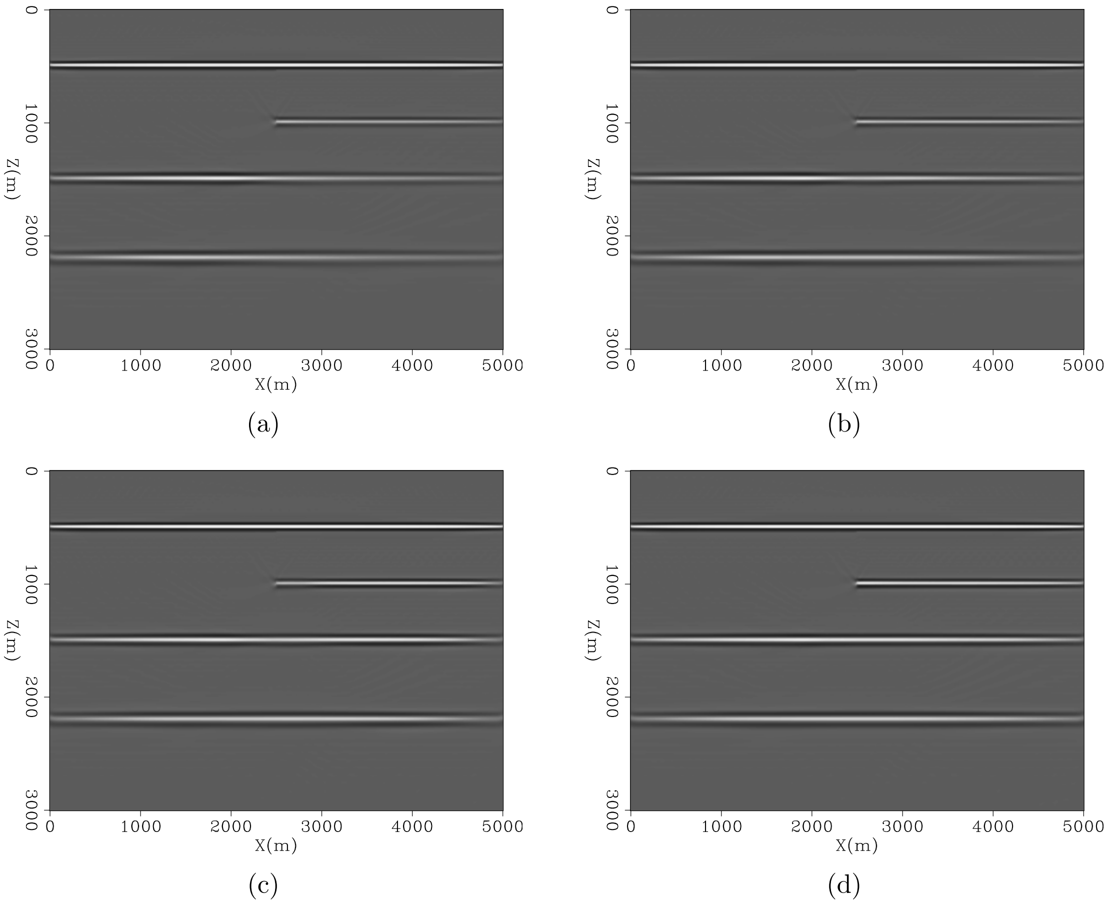

(a) (b) (c) (d)

Figure 3.10: (a) Prestack migration attenuated image. (b) Compensated image using the inverted $Q_p$ model as shown in Figure 3.9(a). (c) Compensated image using the inverted $Q_p$ model as shown in Figure 3.9(b). (d) The reference migration image using the true $Q_p$ model as shown in Figure 3.7(b). [**CR**]

chap3/. layer4-vc-bqtv-bimg,layer4-nc-bqtv-img,layer4-vc-bqtv-img,layer4-timg the entire subsurface). The bright reflectors at about $3,000$ m depth and between inline midpoint locations $2,000$ and $12,000$ m are interpreted as the absorption body that is the main cause of the wiped out image below. The main cause of this effect may be laminated sand/shale sequences with possible gas present in the sand layers. The respective interval velocity section shows fairly low $V_p$, about 1500 m/s, as shown in Figure 3.11(b).

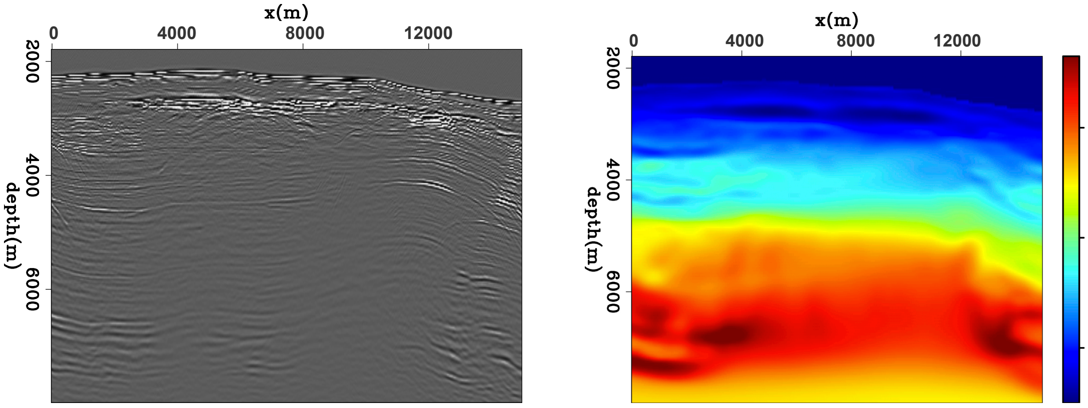

(a) (b)

Figure 3.11: (a) Zero subsurface offset image of prestack-migrated 2D section. (b) Migration velocity for the same section. Seismic data images provided courtesy of CGG Services (U.S.) Inc., Houston, Texas. [**NR**] chap3/. bw2d-nq-bimg-x0,bw2d-bvel-x0

There is a possibility of deeper reservoirs at this location that are difficult to identify due to the aforementioned seismic wave attenuation. Hence, our objective is to estimate $Q_p$ in this section and account for it in migration with $Q_p$ compensation. Specifically, I estimate $Q_p$ model using the new objective function (Equation 3.12) defined in this chapter, and compare the results with the ones obtained using the objective function (Equation 2.1) defined in Chapter 2.

The question now is how to estimate the coefficients in Equation 3.8 at this specific location and without well data available to us. I solve this problem by using the average estimated $Q_p$ (about 30) in the absorption zone from VSP data (which is also not provided except this average $Q_p$ value) and relating this $Q_p$ value to the average velocity (about $1,500$ m/s in this absorption zone) from the velocity model shown in Figure 3.11(b).

Of course, there are an infinite number of solutions for $c_1$, $c_2$, and $c_3$ from a single equation. Here I select just one of these solutions: $c_1 = 2e\text{-}3$, $c_2 = 1e\text{-}6$, and

$c_3 = 8.333e\text{-}4\ s^2/km^2$.

The result for $Q_p$ inversion without constraint is shown in Figure 3.12(a) while the results with the constraint are shown in Figure 3.12(b). Clearly, the $Q_p$ inversion section obtained with the constraint matches the absorption body in Figure 3.11(a) much better than the section obtained without the constraint. I speculate that using the former $Q_p$ model will result in better compensation of the seismic events, leading to a truer image with higher resolution, due to high frequency recovery (Figure 3.13), and better coherency, due to phase correction. The compensated seismic section using downward continuation migration (Shen et al., 2013, 2014) is shown next to the original section in Figure 3.14(a). The events shown in Figure 3.14(b) become sharper and have more balanced amplitude over space after compensation, because of their high frequency recovery. For example, the events of our interests pointed by a red arrow in Figure 3.14(b) have brighter and more balanced amplitude than those in Figure 3.14(a), which makes it easier for reservoir characterization using amplitude analysis. In addition, compensation using a correct $Q_p$ model is able to correct the distorted phased caused by attenuation. As shown by the events pointed by yellow arrows in Figure 3.14(b), the events after compensation become coherent in phase after compensation.

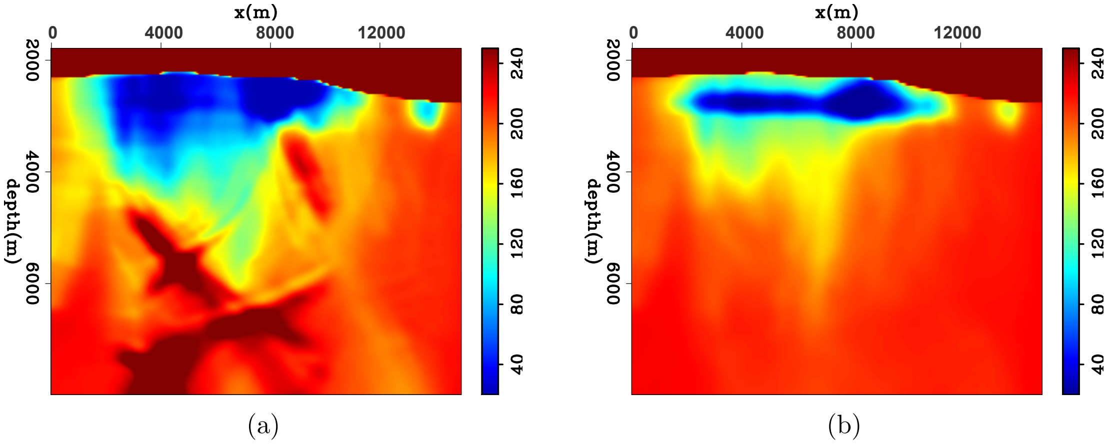

(a) (b)

Figure 3.12: (a) Inverted $Q_p$ model without constraint. (b) Inverted $Q_p$ model with constraint. Seismic data images provided courtesy of CGG Services (U.S.) Inc., Houston, Texas. [**NR**] chap3/. bw2d-nc-bq-x0,bw2d-lc-bq-x0

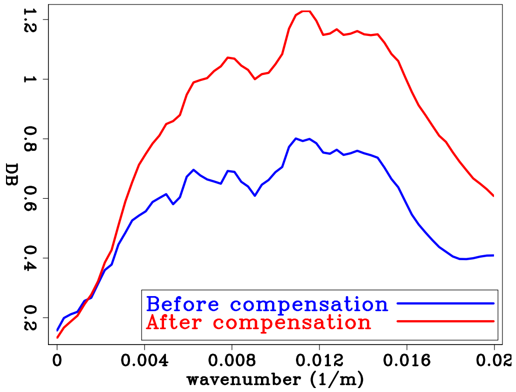

Figure 3.13: Spatial frequency spectra extracted at depth from 4, 000 m to 7, 000 m and inline points between 4, 000 m and 9, 000 m before (blue) and after (red) $Q_p$ compensation. Seismic data images provided courtesy of CGG Services (U.S.) Inc., Houston, Texas. [**NR**] chap3/. bw3d-spex

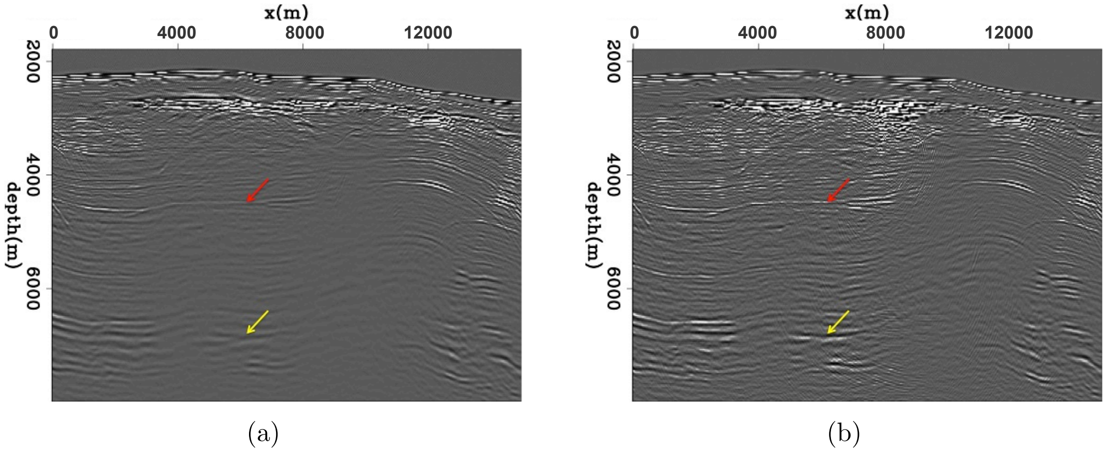

(a) (b)

Figure 3.14: (a) Inverted $Q_p$ model without constraint. (b) Inverted $Q_p$ model with constraint. Seismic data images provided courtesy of CGG Services (U.S.) Inc., Houston, Texas. [**NR**] chap3/. bw2d-nq-bimg-ann-x0,bw2d-lc-bimg-ann-x0

## DISCUSSION

In this chapter, I derived an approximate closed-form solution relating $V_p$ to $Q_p$ using rock physics modeling. This solution is validated using well data in which the elastic properties were measured and $Q_p$ was derived numerically. I applied this new $Q_p - V_p$ equation to both synthetic and field seismic data, which produced an improved $Q_p$ estimated model. I showed that this improved $Q_p$ model leads to a better seismic migration image. However, this method assumes the velocity is known and accurate. If the velocity is wrong, such regularization may even degrade the accuracy of the inversion results. To address these issues, I present a method to both update the velocity model and Q model in the later chapter.

## ACKNOWLEDGMENTS

I would like to thank CGG Services (U.S.) Inc., Houston, Texas for their permission of publishing the GOM field results. I also would like to thank Shell Global Solutions International B.V. for their permission of publishing the GOM field results. I thank Christopher Willacy and Vanessa Goh for their discussion, suggestions and help with the field data application.

# Chapter 4

# Multi-parameter inversion of velocity and Q using wave-equation migration analysis

## INTRODUCTION

In Chapter 2 I develop wave-equation migration Q analysis (WEMQA), to produce a reliable Q model. This method analyzes attenuation effects from the seismic image migrated with the current velocity and Q models. In Chapter 3 I present an approximate closed-form solution directly relating velocity to Q for compressional wave that can be used as a constraint term in WEMQA to improve the accuracy of the seismic inversion of the Q model. Both methods require highly accurate velocity models. An inaccurate velocity model used by WEMQA distorts the spectra of the migrated events and causes errors in spectral analysis for estimating the attenuation effects. In addition, the seismic inversion constrained by an inaccurate velocity model degrades the accuracy of the inverted Q model. Therefore, joint inversion of both velocity and Q models becomes mandatory if neither of these models is correct.

In this Chapter, I develop a method for multi-parameter inversion of velocity and Q models using wave-equation migration analysis. Then I test this method on a synthetic dataset to demonstrate its benefit and effectiveness. I will apply this method to the field data examples in Chapter 5.

# PROBLEM SETUP

## Simultaneous estimation of velocity and Q models

I pose the estimation problem as an optimization problem that seeks optimum velocity and Q models simultaneously by minimizing two user-defined objective functions:

$$J = J_v(v, Q) + \beta J_Q(v, Q), \tag{4.1}$$

where $\beta$ is a weighting parameter that balances two user-defined functions $J_v(v, Q)$ and $J_Q(v, Q)$, and can be changed through iterations. Both $J_v(v, Q)$ and $J_Q(v, Q)$ are functions of $v$ and $Q$, where $v$ is the current interval velocity and $Q$ is the current Q model. I define the function $J_Q(v, Q)$ as follows:

$$J_Q(v, Q) = \frac{1}{2} \sum_{\mathbf{x}} \left| \rho \left( \mathbf{x}; v, Q \right) \right|^2, \tag{4.2}$$

where $bfx$ is the spatial location. Migration with inaccurate velocity or inaccurate Q models distorts the spectra of the migrated events. The parameter $\rho$ in function $J_Q(v, Q)$ (Equation 4.2) quantifies such spectral change in a migrated seismic image and its definition and calculation are the same as described in Chapter 2.

The function $J_v(v, Q)$ defined in Equation 4.1 accounts for the kinematic changes of an image caused by an inaccurate velocity model or an inaccurate Q model. Theoretically, obtaining accurate velocity and Q models results in flat events in the subsurface angle-domain common-image gathers (ADCIGs). The objective function $J_v(v, Q)$ evaluates the flatness of ADCIGs, which constitutes one approach in the implementation of wave-equation migration velocity analysis (WEMVA) (Symes and Carazzone, 1991; Biondi and Sava, 1999; Shen et al., 2003). Symes and Carazzone (1991); Biondi and Sava (1999); Shen et al. (2003) proposed several ADCIG-based WEMVA objective functions. In the following section I show two approaches to enforce the flatness of ADCIGs.

### Stack-power maximization

The stack-power maximization (SPM) (Soubaras and Gratacos, 2004) maximizes the power of stack of the ADCIGs, as follows:

$$J_v(v,Q) = \frac{1}{2}\sum_{\gamma}\sum_{\mathbf{x}} \left|I\left(\mathbf{x},\gamma;v,Q\right)\right|^2, \tag{4.3}$$

where $\gamma$ is the reflection angle and $I\left(\mathbf{x},\gamma;v,Q\right)$ is the ADCIGs migrated using the current velocity and Q models. Theoretically, the image obtained by stacking all of the angles in ADCIGs is equivalent to the image at its zero-subsurface offset. In practice, objective function in Equation 4.3 can be computed by maximizing the image at its zero-subsurface offset as follows, which saves the computational cost and memory of computing and storing the ADCIGs.

$$J_v(v,Q) = \frac{1}{2}\sum_{\mathbf{x}} \left|I\left(\mathbf{x};v,Q\right)\right|^2, \tag{4.4}$$

where $I\left(\mathbf{x};v,Q\right)$ is the image at zero-subsurface offset.

If the current velocity has large error, the events in ADCIGs will become strongly curved, and consequently, such stacking using Equation 4.3 or Equation 4.4 suffers from cycle-skipping problem as described in Zhang and Shan (2013). Therefore, this approach only works well if the current velocity model is close to the true velocity.

### Differential semblance optimization

Differential semblance optimization (DSO) is another approach to achieve the goal of flattening the events in ADCIGs (Shen and Calandra, 2005). This method minimizes the differences between the migrated images of contiguous angles, and it overcomes the the cycle-skipping problem as illustrated in the previous work by Zhang and Shan (2013). In my study, I use the normalized DSO (Tang, 2011) as the criterion to drive the optimization. This objective function normalizes the square of the root-mean-squared (RMS) image amplitudes in the subsurface-offset **h** domain to reduce the influence of image amplitude variations caused by attenuation and uneven illumination. The normalized DSO objective function can be formulated (Tang, 2011) as follows:

$$J_v(v,Q) = \frac{1}{2}\sum_{\mathbf{x}} \frac{\sum\limits_{\mathbf{h}} \left|\mathbf{h}\right|^2 \left|I\left(\mathbf{x},\mathbf{h};v,Q\right)\right|^2}{\sum\limits_{\mathbf{h}} \left|I\left(\mathbf{x},\mathbf{h};v,Q\right)\right|^2}, \tag{4.5}$$

where $I\left(\mathbf{x},\mathbf{h}\right)$ is the migrated image with the current velocity and Q models in the subsurface-offset domain. The physical interpretation of the subsurface-offset-domain DSO is that it optimizes the models by penalizing energy at non-zero subsurface offset, taking advantage of the fact that seismic events should focus at zero-subsurface offset if migrated using accurate models. However, DSO amplifies the high-frequency in the image and can generate unwanted artifacts in the gradient (Fei and Williamson, 2010), which slows down convergence.

The **partial stack-power-maximization (PSPM)** (Zhang and Shan, 2013) is an alternative objective function that aims at mitigating both the cycle-skipping problem (as described in SPM) and the gradient artifacts (as described in DSO). This method uses a partial stacking operator to stack ADCIGs in small groups, instead of stacking ADCIGs all at once in SPM. The PSPM combines the merits of the SPM and DSO objective functions, which will be the future work of my study.

In the following synthetic applications, I will use normalized DSO as shown in Equation 4.5 as the objective function. However, computing a pre-stack seismic image with subsurface-offset of a 3D dataset requires high computing expense and memory storage. In the 3D field data application in Chapter 5, the velocity model has been already estimated by Dolphin but still needs a further update. I assume this model is sufficiently close to the true model, and I choose Equation 4.4 as the objective function to update this velocity to save the memory storage of subsurface offsets.

## Sequential estimation of velocity and Q models

Simultaneously inverting for velocity and Q using Equation 4.1 results in ambiguity between velocity and Q. Fortunately, the kinematic change caused by an inaccurate Q model is barely observed in the ADCIGs, the unflatness of the events in ADCIGs are mainly caused by an inaccurate velocity. Therefore, I approximate the function $J_v(v, Q)$ to $J_v(v)$ that only depends on velocity. To avoid the ambiguity present in the spectral distortion in function $J_Q(v, Q)$ (Equation 4.2) produced from velocity and Q, I choose $\beta$ to be small at the early iterations. In such way, the objective function using Equation 4.1 mainly updates the velocity at the beginning. After the velocity inversion has converged, I set $\beta$ to be large, so that the objective function in Equation 4.1 mainly focuses the term of $J_Q(v, Q)$ . I assume the estimated velocity after the early iterations to be close enough to the true model, and in turn, I approximate the function $J_Q(v, Q)$ to be $J_Q(Q)$ that only depends on Q. Consequently, the simultaneous estimation of velocity and Q models is equivalent to a sequential inversion, which first estimates velocity using WEMVA, then estimates Q model using WEMQA. I will apply such sequential estimation to the later numerical application of this chapter and the field data application in Chapter 5

## NUMERICAL EXAMPLE

In order to demonstrate this methodology, I use a portion of the SEAM synthetic velocity, adding two gas clouds with lower velocity than the surrounding sediments, as shown in Figure 4.1(a). The Q model (in logarithmic scale) shown in Figure 4.1(b) also includes these two gas clouds with high attenuation. I generate a 2D synthetic dataset with 56 shots with 100 m spacing, 137 receivers with 40 m spacing, and a Ricker source wavelet with 12 Hz central frequency.

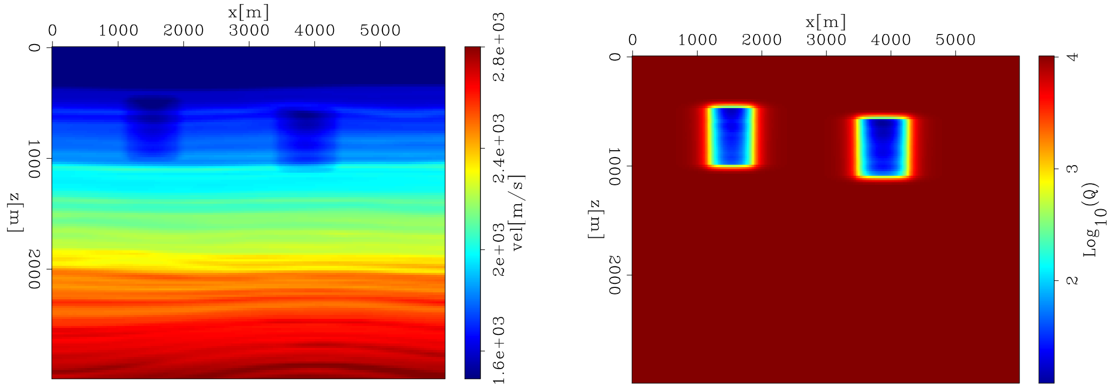

(a) (b)

Figure 4.1: True models: (a) A part of a modified SEAM velocity model with two gas clouds; (b) Q model (in logarithmic scale) with two gas clouds. [**ER**] chap4/. seam2D.vel.2gas,seam2D.Q

The first test in this example consists of inverting for the Q model with the inaccurate velocity model shown in Figure 4.2(a). The inaccurate velocity in Figure 4.2(a) has the same background velocity as that in Figure 4.1(a). However, the velocity of the left gas cloud in Figure 4.2(a) is slightly higher than the true velocity in Figure 4.1(a) and is set to be the same as the surrounding sediments. The the velocity of the right gas cloud in Figure 4.2(a) remains as the true velocity in Figure

4.1(a).

The initial model for Q inversion is a model without attenuation. Figure 4.2(b) shows the inversion results (in logarithmic scale) using WEMQA presented in Chapter 2. The results show that this Q inversion method with accurate velocity on the right part of the model, as shown in Figure 4.2(a), sufficiently recovers the location and value of the right gas cloud, as shown in Figure 4.2(b). However, in the presence of inaccurate velocity in the left part of the model, as shown in Figure 4.2(a), the method fails in retrieving the left gas cloud. The main reason for this failure is the inaccurate velocity that distorts the kinematics of the migrated structures, and subsequently degrades the accuracy of the spectra analysis for Q inversion. Therefore, multi-parameter inversion of both velocity and Q models is needed to obtain a reasonable inversion results, when the accuracy of the initial models is not enough.

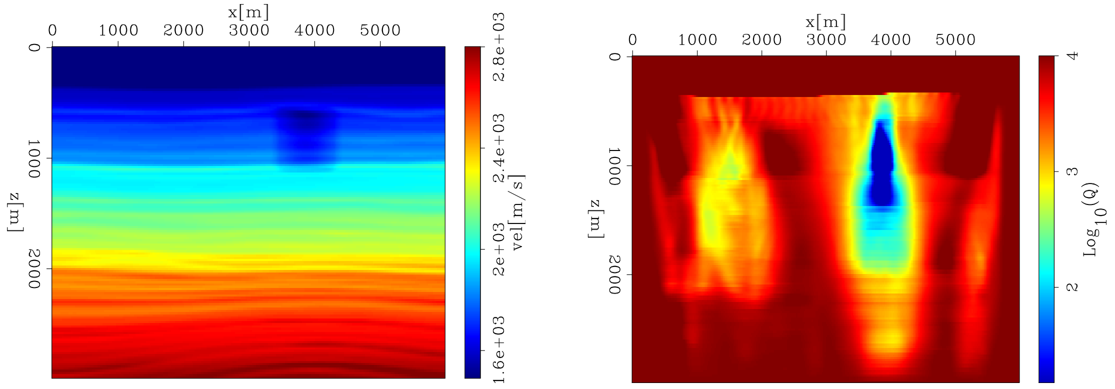

(a)

(b)

Figure 4.2: (a) Inaccurate initial velocity model for Q inversion with only one gas cloud instead of two. Initial Q is constant. (b) Inverted Q model using inaccurate velocity model in Figure 4.2(a). [**CR**] chap4/. seam2D.vel.1gas,seam2D.iQ.xvel

To sequentially invert for velocity and Q models, the initial velocity model has the same background velocity and right gas velocity, as shown in Figure 4.1(a), but without the velocity drop in the left gas cloud. The initial Q model represents no attenuation. Figure 4.3(a) is the inverted velocity model and Figure 4.3(b) is the inverted Q model. Such multi-parameter inversion successfully retrieves the locations and values of both gas clouds in velocity and Q models.

Figure 4.4(a) is the migrated image using the initial velocity and Q models. The initial velocity model has a larger velocity in the left gas cloud, which causes the events below to be pushed downward and become discontinuous, as indicated by the

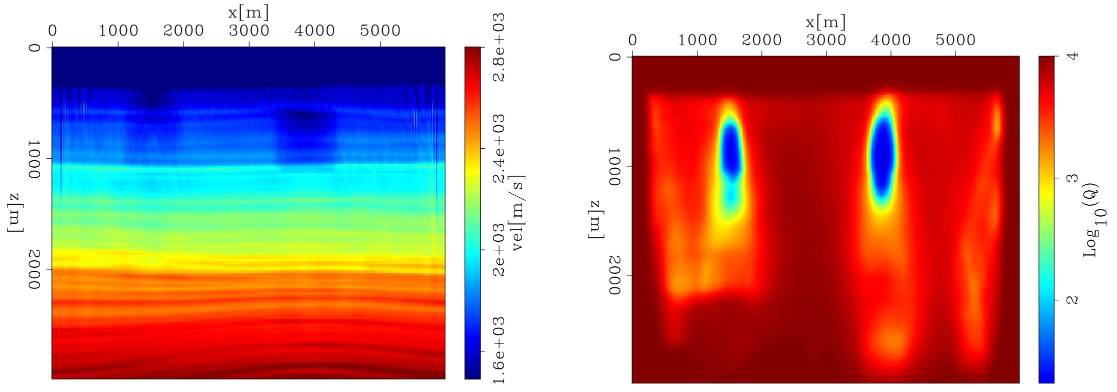

(a) (b)

Figure 4.3: Multi-parameter inversion results: (a) The inverted velocity model. Note how the gas cloud on the left has been recovered. (b) The inverted Q model. The Q value of the left gas cloud has been recovered. [**CR**] chap4/. seam2D.ivel,seam2D.iQ

yellow arrows on the left of Figure 4.4(a). Attenuation caused by these two gas clouds degrades the quality of the deep imaged structures in Figure 4.4(a) (see all the highlights), in terms of dimming the amplitudes, making the events incoherent and stretching the wavelets. Figure 4.4(b) is the migrated image using the inverted models in Figure 4.3. Migration with the improved velocity model in Figure 4.3(a) moves the events below the left gas cloud upward and makes them more coherent, as indicated by the yellow arrows on the left of Figure 4.4(b). Also, compensation with the inverted Q model shown in Figure 4.3(b) makes the events sharper and more balanced in both phase and amplitudes, as shown in Figure 4.4(b) (see all the highlights).

Figure 4.5(a) and Figure 4.5(b) are the ADCIGs extracted from the left gas cloud location (x= 1500 m) and obtained with the initial models and the inverted models in Figure 4.3, respectively. The inaccurate higher velocity causes the events to be unflattened, as shown in Figure 4.5(a). The inverted velocity model shown in Figure 4.3(a) corrects such kinematics error and flattens the events in Figure 4.5(b). In addition, migration with the inverted Q model in Figure 4.3(b) compensates for the energy loss that appears especially strong at the near angle as shown in Figure 4.5(a), and therefore makes the amplitude of the events more balanced in Figure 4.5(b).

Figure 4.5(c) and Figure 4.5(d) are the ADCIGs extracted from the right gas cloud location (x= 3800 m) and obtained with the initial models and the inverted models

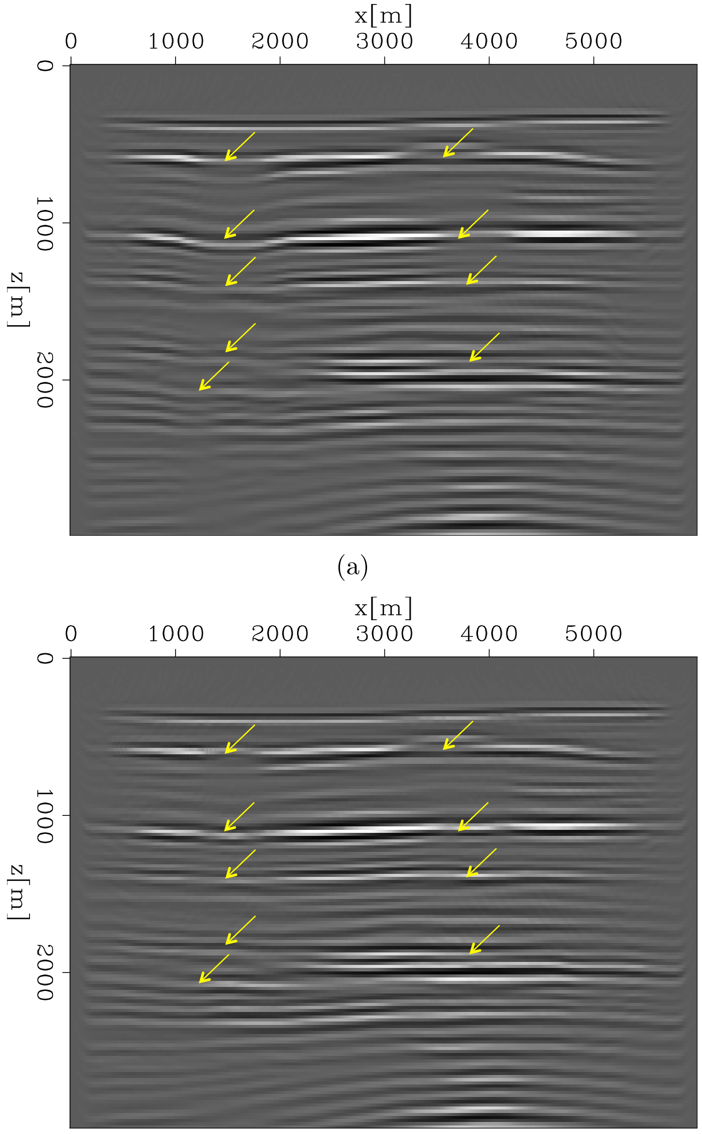

(a)

(b)

Figure 4.4: (a) The migrated image using the initial velocity and Q models; (b) The migrated image using the inverted models in Figure 4.3. The kinematics and the amplitudes under the gas cloud are corrected for by the inverted model. [**CR**] chap4/. seam2D.bimg.bvbq.ann,seam2D.img.iviq.ann

in Figure 4.3, respectively. The near angles in Figure 4.5(c) have low amplitudes, stretched wavelets and unflattened events caused by attenuation, despite the velocity used in this region is correct. Imaging with the inverted Q model in Figure 4.3(b) compensates the high frequency loss caused by attenuation, therefore, it recovers the amplitudes and sharpens the events at the near angles in Figure 4.5(d). In addition, such compensation corrects the phase distortion and velocity dispersion caused by attenuation. As a result, the events in Figure 4.5(d) become more flattened and more coherent than the events in Figure 4.5(c).

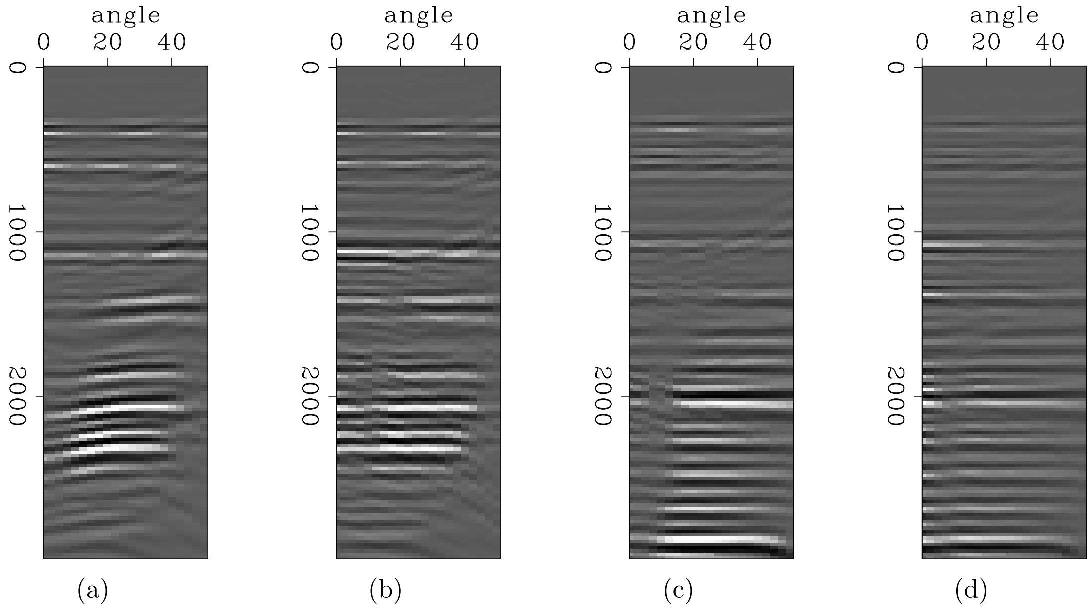

Figure 4.5: (a) The angle domain common image gathers(ADCIG) extracted from the left gas cloud location (x= 1500 m) and obtained with the initial models. The vertical axis is depth with unit of meter. (b) The angle domain common image gather(ADCIG) extracted from the left gas cloud location (x= 1500 m) and obtained with the inverted models shown in Figure 4.3. The vertical axis is depth with unit of meter. (c) The angle domain common image gathers(ADCIG) extracted from the right gas cloud location (x= 3800 m) and obtained with the initial models. The vertical axis is depth with unit of meter. (d) The angle domain common image gather(ADCIG) extracted from the right gas cloud location (x= 3800 m) and obtained with the inverted models in Figure 4.3. The vertical axis is depth with unit of meter. [**CR**]

chap4/. seam2D.bang.lgas,seam2D.iang.lgas,seam2D.bang.rgas,seam2D.iang.rgas

## CONCLUSION

I developed a multi-parameter inversion of velocity and Q models using wave-equation migration analysis. This method poses the estimation problem as an optimization problem that seeks optimum velocity and Q models by minimizing user-defined image residuals. The numerical tests on a modified SEAM model with two gas clouds demonstrate the benefit of using such multi-parameter inversion, when the existing velocity and Q models are inaccurate. The results show that this inversion method is able to retrieve both velocity and Q models, and to correct and compensate the distorted migrated image caused by inaccurate velocity and Q models.

# Chapter 5

# Field data application

The field data used in this chapter is provided courtesy of Dolphin Geophysical. The Dolphin Geophysicals (Dolphin) multi-client field data acquired in the North Sea (CNS data) used in this study has attenuation problems. The area was under the influence of salt tectonics, producing two diapirs. Dolphin interpreted a gas chimney above one diapir, and a channel above the other. The gas chimney forms a migration pathway for the gas to leak and then accumulate at the shallow position (Figure 5.2). The shallow gas gives rise to strong attenuation and low interval velocities in the the area where it is present. The channel also has low interval velocities, and is a strongly attenuating region. These complexities reduce the amplitudes and distort the phases of deeper events, and essentially create a shadow zone over the salt body and over the potential reservoir target area, thus hampering accurate reservoir interpretation. Therefore, it is important to build a velocity model as accurately as possible. It is also valuable to understand and quantify the effects of the attenuation anomalies to create an accurate laterally- and vertically- varying attenuation model.

Using the velocity model provided by Dolphin, I migrated the data. As a quality control measure I calculated angle domain common image gathers (ADCIGs). These gathers showed downward curving events, indicating that the initial velocity model was too fast. Furthermore, both the migrated image and the angle gathers show that the events below the interpreted shallow gas and channel regions are wiped out because of attenuation (Figure 5.10), which will be described in more detail later in chapter. The objective of my study is to update the provided velocity model, especially in the gas and channel regions, and invert for the Q model to recover these two anomalies. In this way, the improvements in image quality using the derived model provide greater confidence for hydrocarbon exploration.

In this chapter, I first give an overview of these field data. Second, I present my preprocessing workflow including coordinates manipulation, the removal the noise, multiples, bubbles and ghosts. Third, I apply wave-equation migration Q analysis (WEMQA) as described in Chapter 2 combined with wave-equation migration velocity analysis (WEMVA) (Symes and Carazzone, 1991; Biondi and Sava, 1999; Shen et al., 2003) to update the current velocity model and invert for the Q model to recover the Q anomalies. In the third part, I use the workflow proposed in Chapter 4 to sequentially estimate velocity and Q models. I test WEMQA with both one-way downward continuation (referred as **one-way WEMQA**) and time-domain wavefield propagation (referred as **two-way WEMQA**) on one representative 2D section of this data. Then, I apply WEMQA with one-way downward continuation to this 3D field.

## CNS DATASET OVERVIEW

The CNS data is acquired using a marine-towed streamer seismic survey in the North Sea. The data provided by Dolphin for this research are composed of 28 sail lines, which were acquired by three vessels. The streamer configurations for the survey of three vessels are similar. Figure 5.1(a) shows the streamer configuration for the survey of vessel with 10 streamers. Each streamer is 6,000 m long, and the separation between the neighboring streamers is 75 m. The source was configured as two shots in a flip-flop mode with a shot interval of 25 m. The crossline source separation was 37.5 m. The streamer depth for all the survey was 30 m, and the source depth was 6 m, as shown in Figure 5.1(b). As a result, both the receiver-side ghost notch and source-side ghost notch are able to be calculated using equation $f = c/2d$, where $f$ is the frequency of the first ghost notch, $c$ is the water velocity of 1500 m/s and $d$ is the streamer/source depth. The results show that the receiver-side ghost has its first notch at 25 Hz (blue curve in Figure 5.8), and the source-side ghost has its first ghost notch at 125 Hz.

The CNS data have strong attenuation anomalies. The depth slice provided by Dolphin in Figure 5.2 highlights the areas with the strongest gas chimneys and

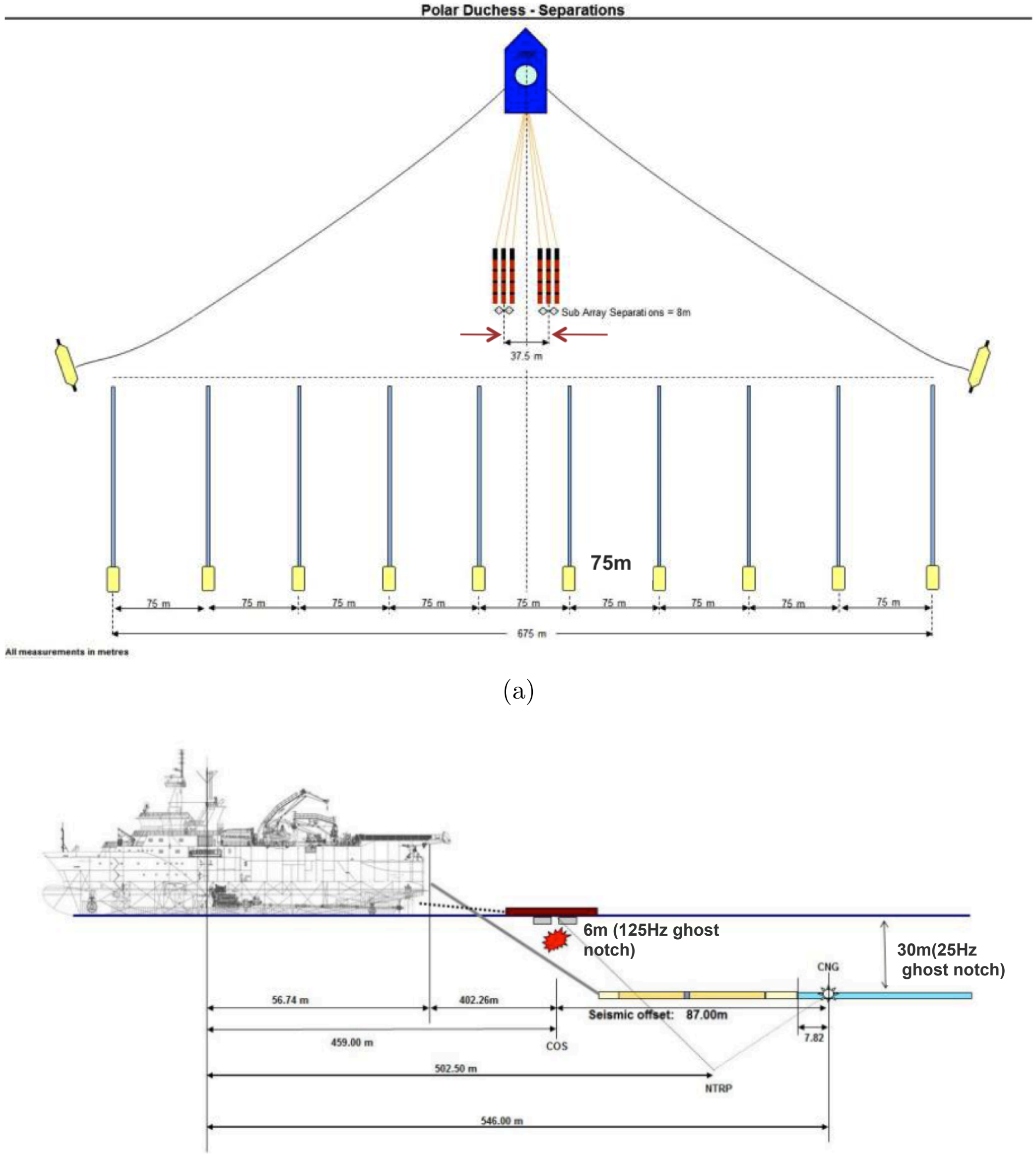

(a)

(b)

Figure 5.1: (a) The streamer configuration for the survey and (b) the boat configuration of one of the three vessels that are involved in these field data acquisition. [**NR**] chap5/. dlp-boat3,dlp-boat2

strongest channel effect. The depth slice in Figure 5.2 does not cover the entire survey, but it covers the most complex area for the study of these anomalies. According to the interpretation by Dolphin, attenuation appears stronger from gas chimneys than from the channels. Attenuation from the gas is stronger on the right dome of the slice than on the bottom left dome of the slice. The channel at the top left of the slice shows low velocities, and there might be Q anomalies with it, but it is a weaker effect than in the gas chimneys. The part of the survey provided by Dolphin for this study covers the left gas chimney and channel but does not include the anomaly on the right of the slice.

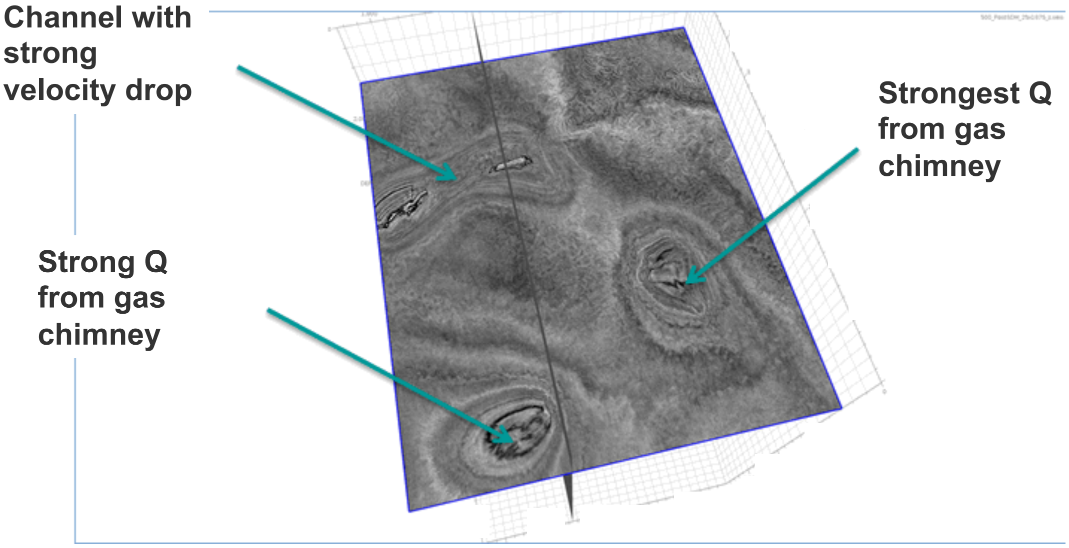

Figure 5.2: A depth slice provided by Dolphin that highlights the areas with the strongest anomalies associated to gas chimneys and channel. North is upward. [**NR**] chap5/. dlp-depth

# PREPROCESSING

## Coordinates manipulation

The original coordinates of source and receiver of CNS data provided by Dolphin are neither regularly sampled along the inline nor the crossline direction, and they are in a rotated Cartesian coordinate system. First, I shifted the origins of the coordinates and rotated the tilted coordinates to align the x–axis with the inline direction and the y–axis with the crossline direction. The rotated and shifted coordinates of source and receivers are shown in Figure 5.3. Aligning the processing grid axes with the acquisition inline and cross-line directions makes it easy to bin the seismic shot gathers to the regularly sampled data grid that I create. Then, I regularized the source and receiver grids using the parameters shown in Table 5.1, facilitating subsequent data processing.

Table 5.1: The parameters used for regularizing the grids

| Keys | number | origin [m] | spacing [m] |
|---|---|---|---|
| Receiver at crossline (Y) | 10 | -337.5 | 75 |
| Receiver at inline (X) | 240 | 50 | 25 |
| Source at crossline (Y) | 28 | 2100 | 300 |
| Source at inline (X) | 1239 | 230 | 50 |

## Denoise, Demultiple, Debubble and Deghost

This data is strongly influenced by swell waves that propagate along the interface between water and air. Such noise can be identified in the FK domain of the data. Figure 5.4(a) shows a common offset gather at offset=300 m. The vertical stripes in the common offset gather are the low-frequency noise that is generated by the swell noise. Figure 5.5(a) shows the same common offset gather as Figure 5.4(a) in the FK domain. The horizontal strip around -2 to 2 Hz frequency corresponds to the low-frequency swell noise. Therefore, I use a low-cut filter at 2 Hz to remove such noise. Figure 5.5(b) shows the common offset gather in the FK domain after filtering. The result in the temporal and spatial domain is shown in Figure 5.4(b). Notice the virtual absence of vertical strips, which means the swell noise is removed.

Beside the swell noise, these data are also contaminated by water-bottom multiples, salt-interval multiples, bubbles from the airguns, and ghost effects described in the previous section. These noises appear as copies of events, e.g. water bottom reflection, at a periodic spatial interval. I used a gapped Prediction Error Filter (PEF) (Clarebout and Fomel, 2014) to remove such repetitive patterns . As seen in 5.6(a) and 5.6(b), the gapped PEF reduces the appearance of multiples as well as bubble and ghost effects in common offset gathers.

Similarly, in Figures 5.7(a) and Figure 5.7(b) we see a reduction in bubbles, ghosts

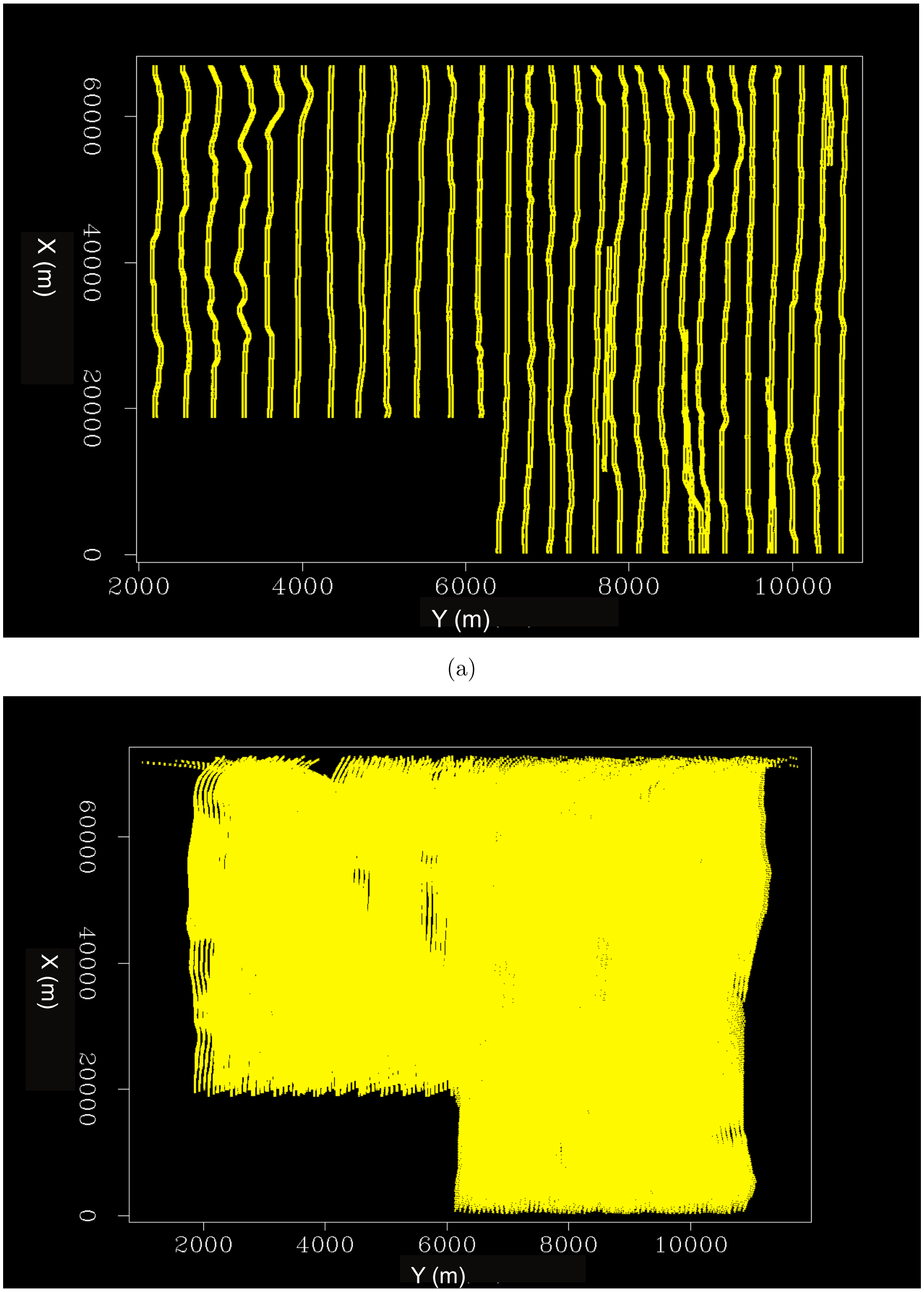

(a)

(b)

Figure 5.3: Rotated and shifted coordinates of (a) shots and (b) receivers. [**NR**] chap5/. dlp-src-rot2,dlp-rec-rot2

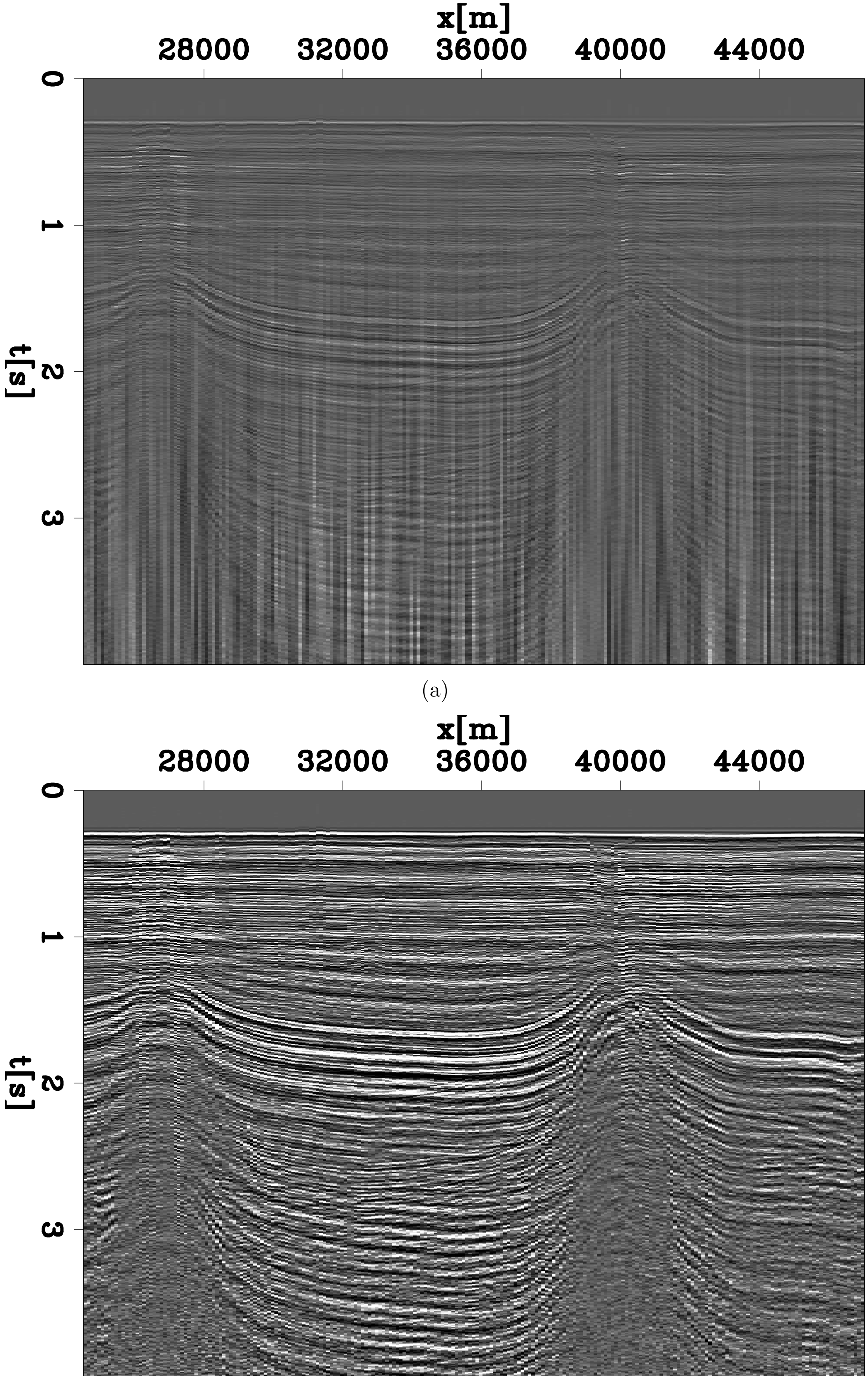

(a)

(b)

Figure 5.4: Common offset gather at offset=300 m: (a) before denoise; (b) after denoise. [**CR**] chap5/. dlp-dprc-offh,dlp-mprc-offh-fkd

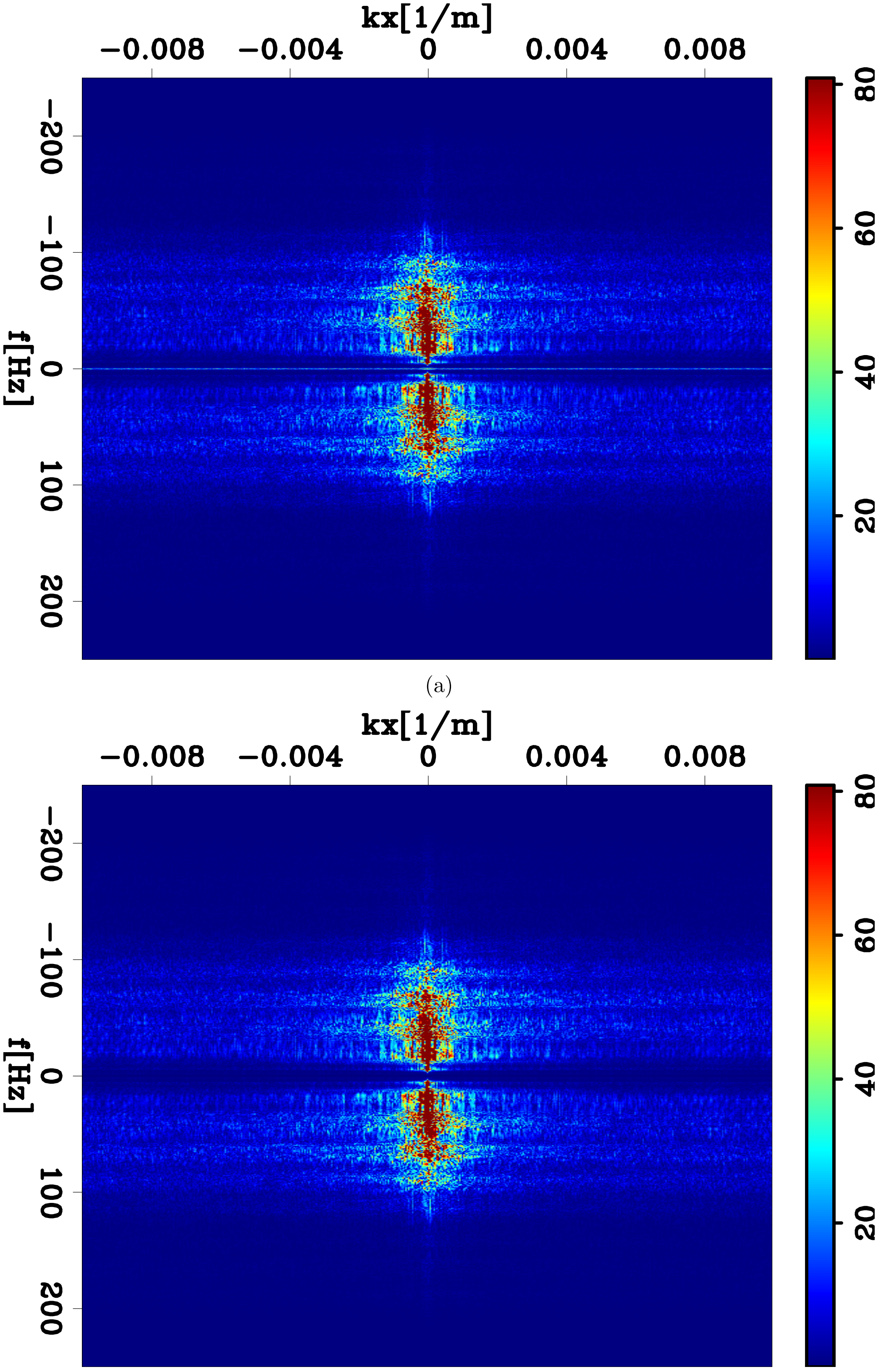

(a)

(b)

Figure 5.5: FK domain transform of the common offset gather at offset=300: (a) before low-cut filter being applied; and (b) after low-cut filter being applied. [**CR**] chap5/. dlp-mprc-offh-fkb,dlp-mprc-offh-fka

and multiples in the source gathers. The source gathers contain a repetitive event that is still not fully understood. It may be the result of a wave bouncing off the back of the vessel. Although its origins are not fully understood, the gapped PEF also reduces its appearance.

A benefit of this preprocessing is that it flattens the receiver-side ghost notch, as seen in Figure 5.8. However, one downside of using a gapped PEF is that in the process of flattening the spectrum, it also boosts high frequency noise. Because of the noisy wiggles on the spectra in Figure 5.8, I use the frequency range up to 50Hz that has a relative high signal-to-noise ratio for my later inversion.

## 2D WEMVA AND WEMQA APPLICATION

For the model building for this field study, I first focused the analysis on one representative two-dimensional (2D) section in order to develop the inversion workflow and corresponding parameter set for this particular dataset, and thus better pave the way to 3D field inversion. This is an inline 2D section with a constant crossline value of 7,500 m, which passes through the left-side gas chimney and the left channel as shown in Figure 5.2. Figure 5.9 is the 2D slice of the 3D depth interval velocity model provided by Dolphin crossline location 7,500 m. I use this as the initial velocity model for the velocity inversion. The velocity model shows a salt body with two diapirs, and a high-velocity layer above the salt body. This layer acts as a potential cap. The gas chimney can act as a migration pathway for the trapped gas that leaks and accumulates at the shallow position above the left diapir. Shallow gas regions correlate to low velocity and strong attenuation, so the velocities shown in Figure 5.9 at the shallow position above the left salt dome is slower than the surrounding areas. The area above the right salt dome also has slow velocities as shown in Figure 5.9 related to a low-velocity channel that was interpreted by Dolphin. The attenuation in the channel region is interpreted to be strong. Because Dolphin has not provided the Q model, the initial Q model for the inversion is set to be homogeneous with a value of 500 that is a typical value for the materials expected in most of the model.

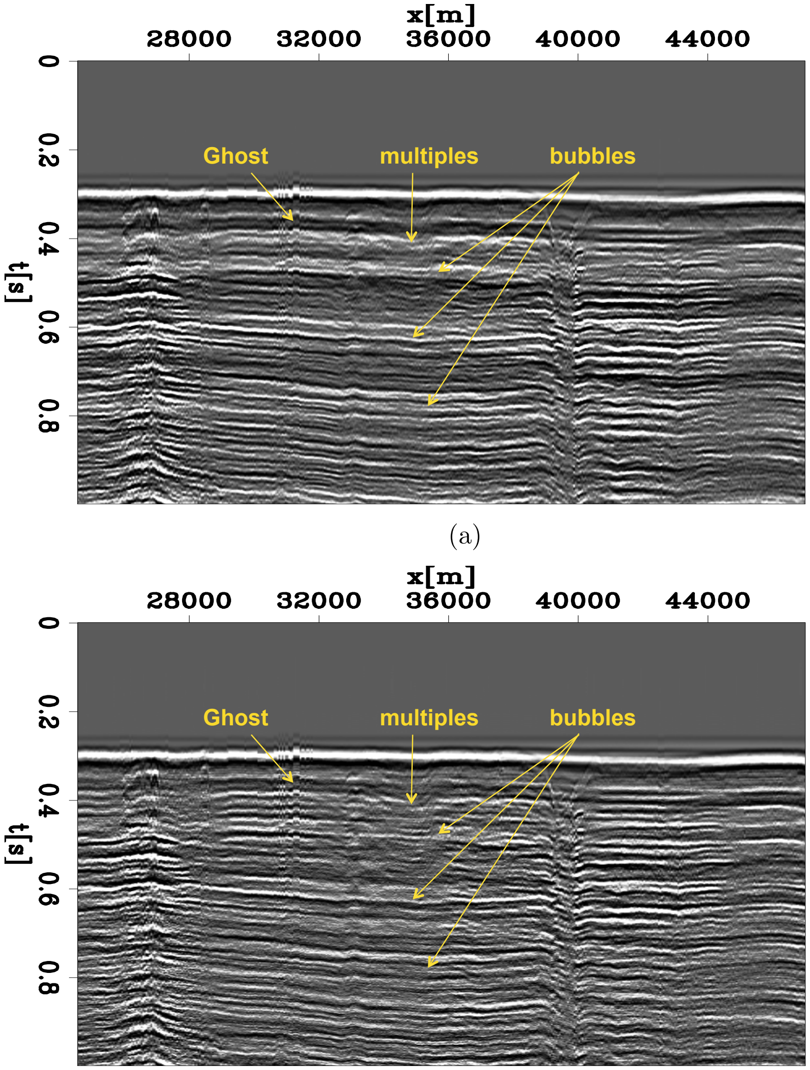

(a)

(b)

Figure 5.6: Windowed common offset gather at offset=300 m: (a) before processing with a gapped PEF; (b) after processing with a gapped PEF. The yellow arrows show the bubbles, ghosts and multiples in Figure 5.6(a). Such events, of which the locations are also indicated by yellow arrows in Figure 5.6(a), are greatly reduced. [**CR**] chap5/. dlp-mprc-offh-fkd-win2,dlp-mprc-offh-pefm3-win2

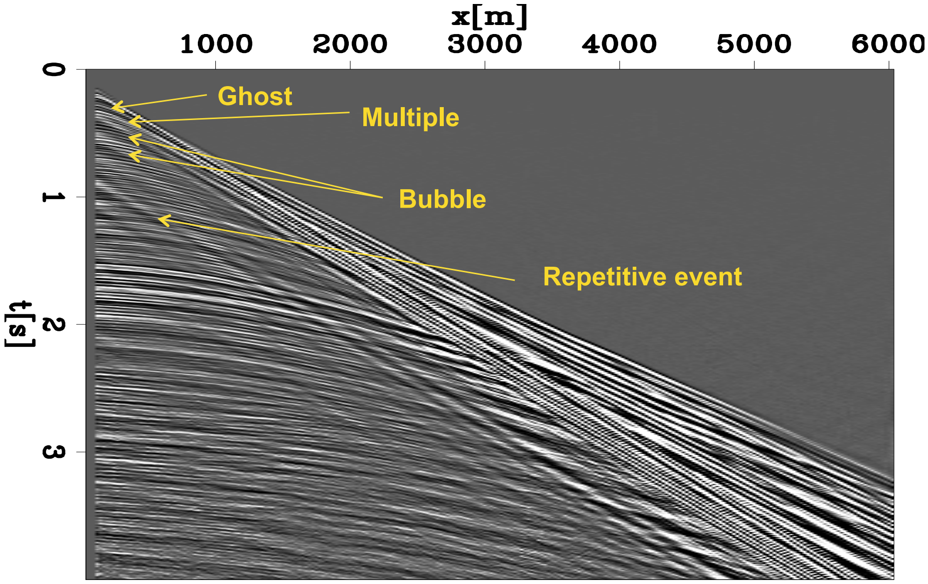

(a)

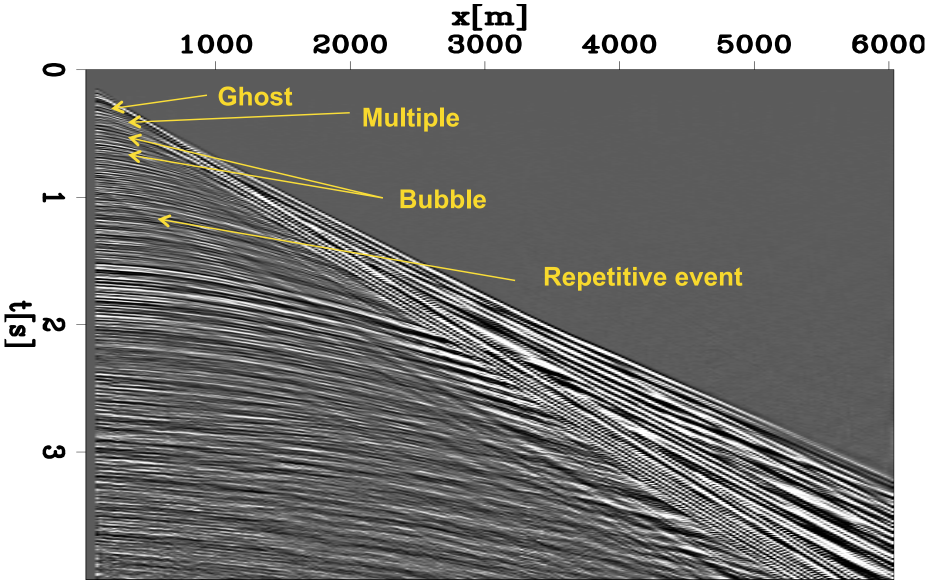

(b)

Figure 5.7: Shot gather at inline=24,580 m, crossline =7,500 m: (a) before processing with a gapped PEF; (b) after processing with a gapped PEF. Figure 5.7(a) shows the bubbles, ghosts, multiples and an unknown repetitive event that are pointed by the yellow arrows. The locations of these marked events are greatly reduced from Figure 5.7(b) after a gapped PEF being applied. [**CR**] chap5/. dlp-mprc-shte-fkd2,dlp-mprc-shte-pefm3

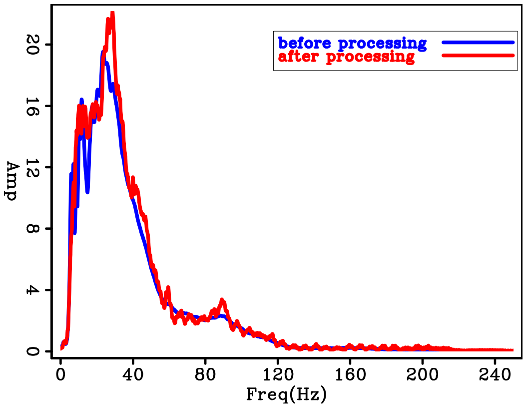

(a)

Figure 5.8: The spectra of Figure 5.7(a) and Figure 5.7(b). The first receiver-side ghost notch is flattened by the preprocessing with a gapped PEF. The noisy wiggles can be observed at the high frequencies, because PEF tries to flatten the spectra and therefore boosts the high frequency noise. [**CR**] chap5/. dlp-mprc-shte-spex

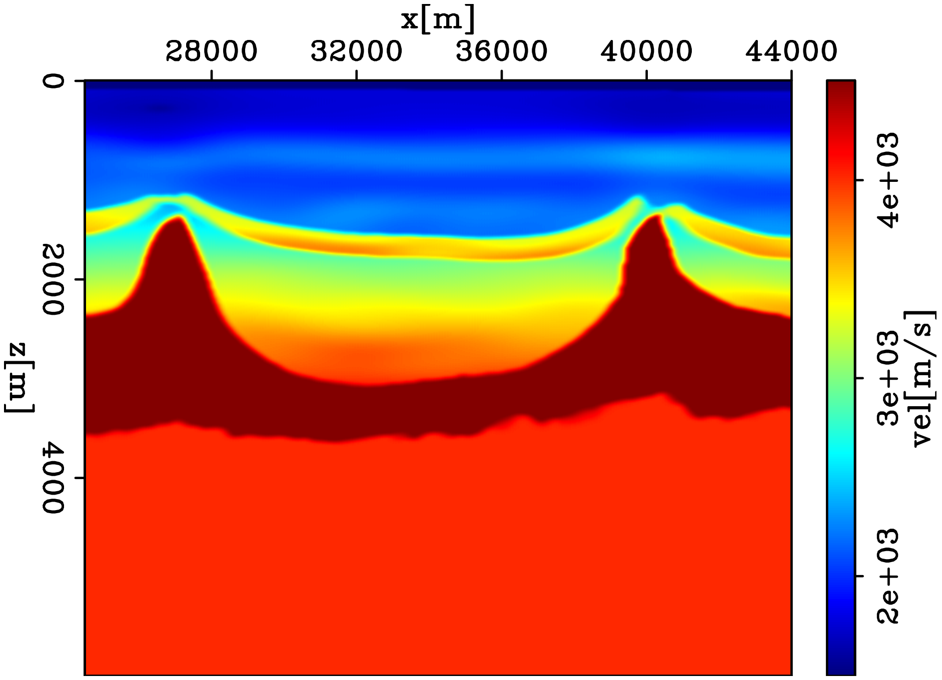

Figure 5.9: A 2D slice of the 3D depth interval velocity model provided by Dolphin at the crossline of 7500 m, which passes through the left-side gas chimney and the left channel as shown in Figure 5.2. [**CR**] chap5/. dlp2D-bqiv-post-basc-bvel-iter0

## 2D one-way WEMVA application

I first update the current velocity using WEMVA (Symes and Carazzone, 1991; Biondi and Sava, 1999; Shen et al., 2003) as described in Chapter 4 . For both migration and tomography in WEMVA I use one-way downward continuation for wavefield propagation. Figure 5.10(a) shows the migrated image using one-way wave-equation migration presented in Chapter 2 at zero subsurface offset using the initial velocity and Q model. The migration frequency range is from 0.8 Hz to 50 Hz. The image space is discretized by 25 m in X and 10 m in Z. The top of the salt body with two domes ( $x = 26,000$ m to $28,000$ m and $x = 38,000$ m to $42,000$ m) is apparent in the image. The bright spots above the left and right salt peaks correspond to the shallow gas and channel, respectively. These two regions have strong sand-shale impedance contrasts and thus their seismic reflection amplitudes are strong, which results in bright spots. Below these bright spots is a dim region caused by attenuation at the shallow gas anomaly and channel. The image is dimming at the boundary ($x < 25,000$ m and $x > 43000$ m) is obscured due to a taper in the boundary condition of the migration. Figure 5.11(a) shows 10 representative Angle Domain Common Image Gathers (ADCIGs) of this migrated image using the initial models. The events in the ADCIGs are not flat but curved down, thereby indicating the velocity is too high. Some of the down-curved events may be the residual multiples that haven't been removed.

Because the initial velocity model in Figure 5.9 has been already estimated by Dolphin, I assume this model is sufficiently close to the true model. I use stack power maximization as shown in Equation 4.4 as the objective function to update this velocity. Because this objective function and its gradient are computationally cheap to calculate, I am able to extend its use to our 3D field data workflow running on an academic computing cluster.

Figure 5.12 shows the velocity gradient of the first iteration of the inversion, in which the sign is opposite of the search direction. The gradient shows strong updates around the shallow gas and channel regions and so in the next iteration the optimization algorithm decrease the velocity. Compared to the initial velocity in Figure 5.9, the velocity model after 20 iterations shown in Figure 5.13 has slower velocities at shallow depths. The velocity difference between the updated velocity (Figure 5.13) and the initial velocity (Figure 5.9) is shown in Figure 5.14. The

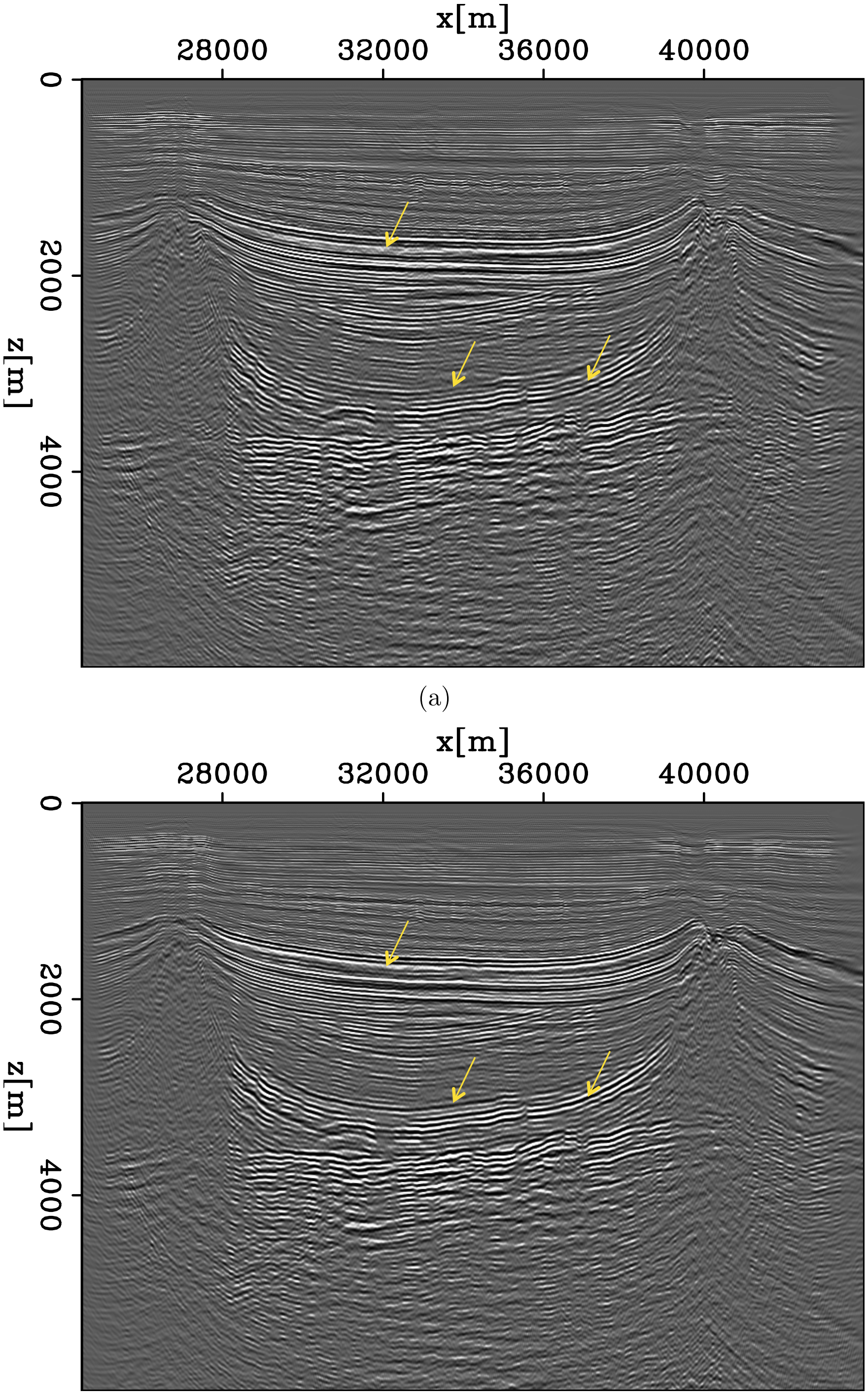

(a)

(b)

Figure 5.10: (a) The migrated image at zero subsurface offset using the initial velocity model and the initial Q model. (b) The migrated image at zero subsurface offset using the updated velocity model and the initial Q model. The events pointed to by yellow arrows become more coherent. [**CR**]
chap5/. dlp2D-bqiv-post-basc-bimg-before-ann,dlp2D-bqiv-post-basc-bimg-after-ann

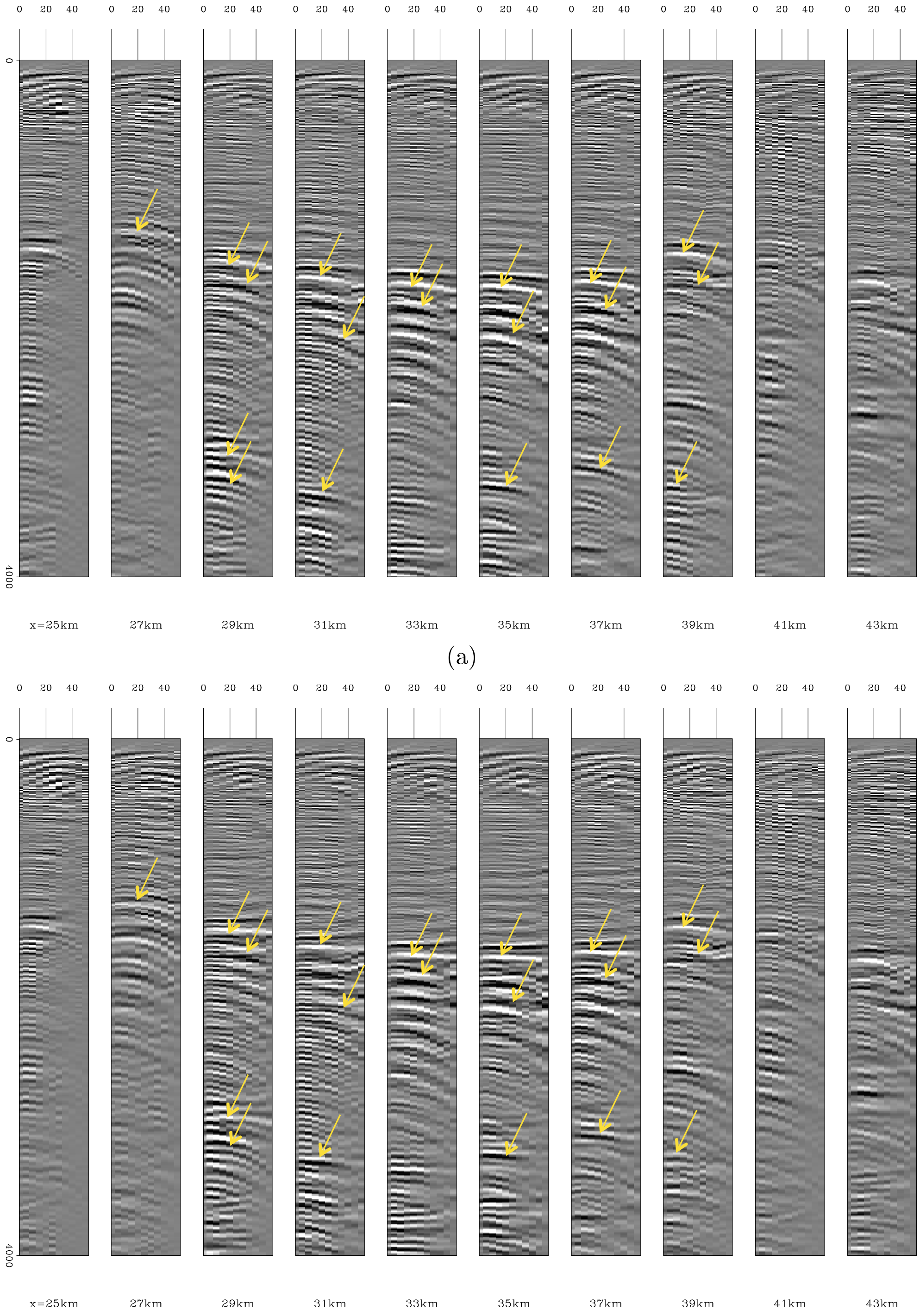

(a)

(b)

Figure 5.11: (a) The ADCIGs using the initial velocity model and the initial Q model. (b) The ADCIGs using the updated velocity model and the initial Q model. The vertical axis is depth in meters. The events pointed to by yellow arrows become flatter. **[CR]**

chap5/. dlp2D-bqiv-post-basc-bang-before-ann,dlp2D-bqiv-post-basc-bang-after-ann reduction of the shallow velocity pushes the events in the ADCIGs upward, which flattens those events. However, the residual multiples remain curved down. The velocity drops more significantly above the salt domes, as shown in Figure 5.13, corresponding to the low-velocity anomalies of shallow gas and channel.

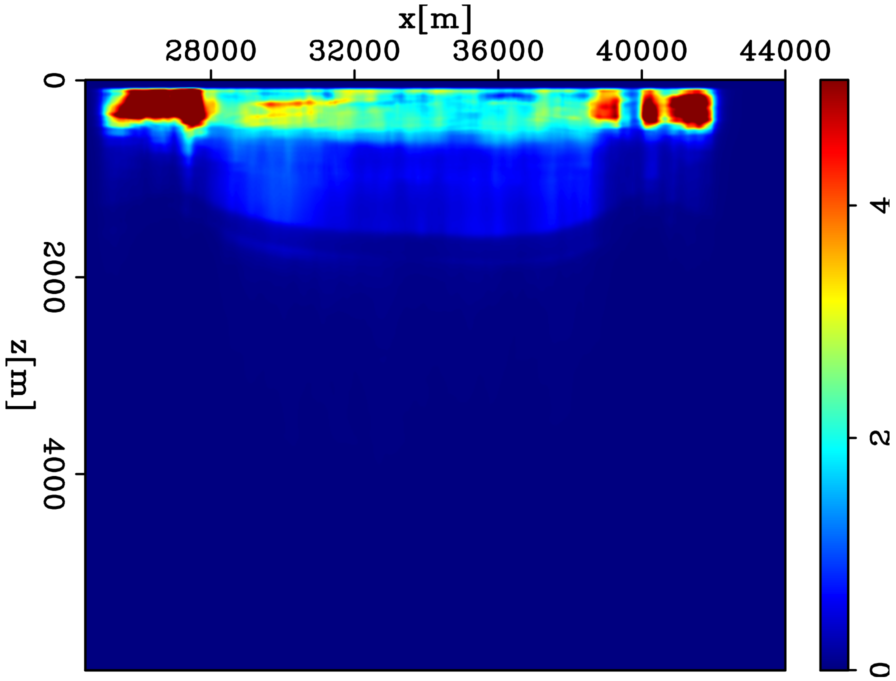

Figure 5.12: The velocity gradient of the first iteration of the inversion. [**CR**] chap5/. dlp2D-bqiv-post-basc-grdp-iter0

When I perform a migration using the updated velocity model with lower shallow velocities and the initial Q model, the events shown in Figure 5.10(b) move up. Additionally, some events (e.g. the flank of the right salt dome) become more coherent in phase after velocity updating, as indicated by the yellow arrows.

The decrease in the shallow velocity after inversion pushes the curves of the events in ADCIGs upward, and therefore flattens the gathers seen in Figure 5.11(b). I use yellow arrows to point out several flattened events as examples to illustrate the improvements. The flattening effect is noticeable above $z = 4,000$ m. A different objective function may improve the flatness deeper; however, events below the base of salt ($z > 4,000$ m) are not the target of my study, and have little (if any) impact on the estimation of the shallow gas and channel for both the velocity and Q models. Because the Q model has not yet been updated, the dimming amplitudes in the seismic image show no improvements in Figure 5.10(b) and Figure 5.11(b).

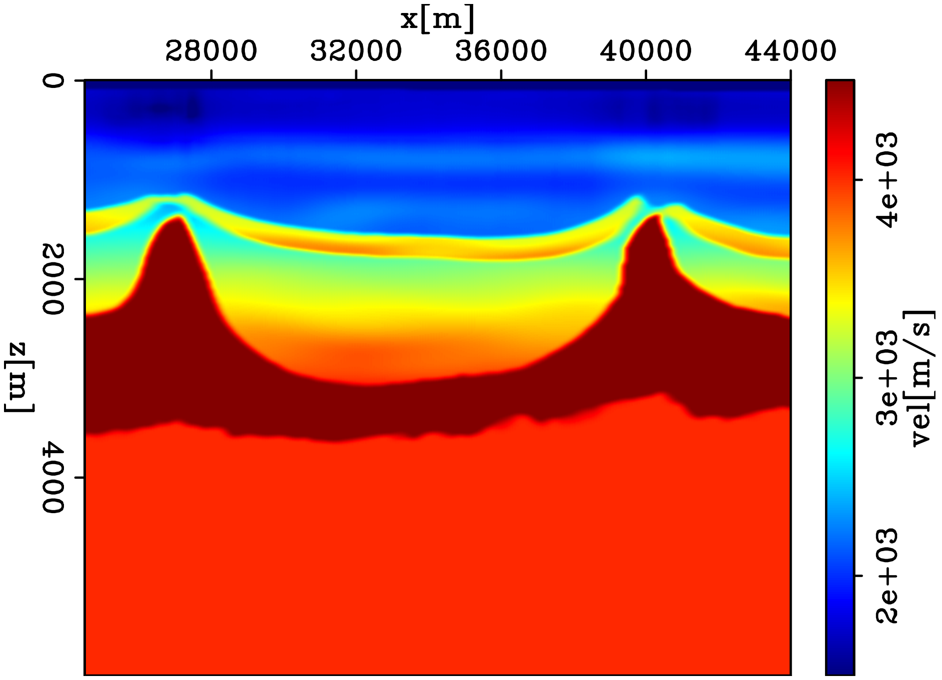

Figure 5.13: The updated velocity after 20 iterations. [**CR**] chap5/. dlp2D-bqiv-post-basc-bvel-iter20

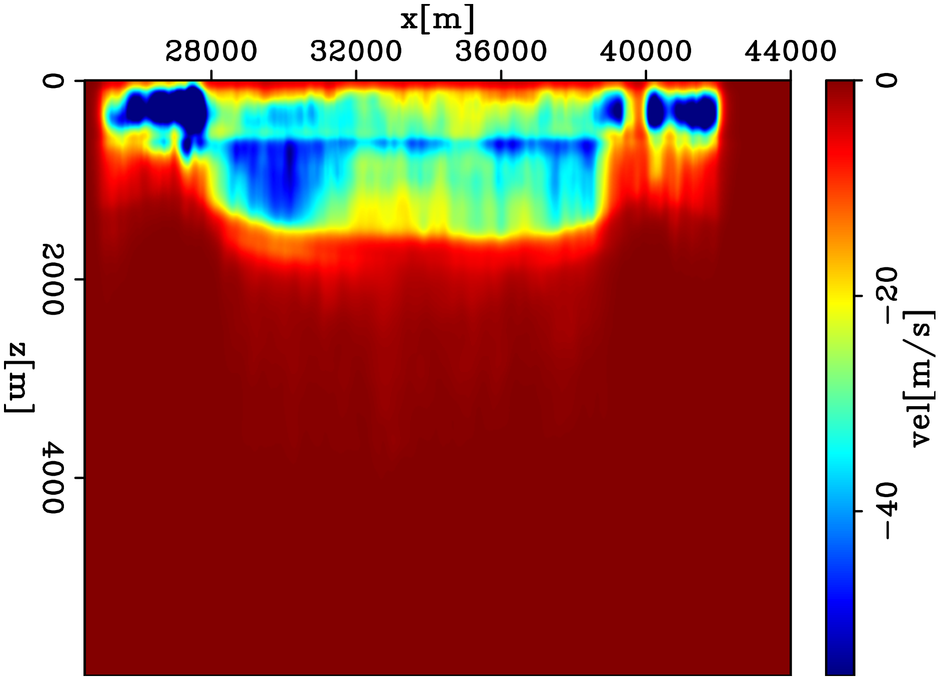

Figure 5.14: The velocity difference between the updated velocity (Figure 5.13) and the initial velocity (Figure 5.9). [**CR**] chap5/. dlp2D-bqiv-post-basc-resd

The stacking power (normalized by the stacking power in the last iteration) curve (Figure 5.15) shows fast convergence in the first few iterations. The objective function shows little increase after four iterations. However, the updated ADCIGs in Figure 5.11(b) show the events are not completely flattened yet.

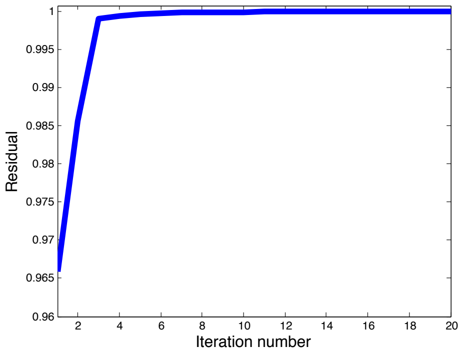

Figure 5.15: Normalized curve for the stacking power objective function. [**NR**] chap5/. dlp2D-one-fobj-V

## 2D one-way WEMQA application

In Chapter 2, I have shown that the parameter slope ($\rho$) is able to effectively quantify the attenuation effects in a seismic image. The slope can be computed from the logarithm of the spectral ratio between a measured spectra and a reference spectra (Tonn, 1991). A negative $\rho$ value means the image is undercompensated; while a positive $\rho$ value means the image is overcompensated. The larger the absolute value of $\rho$, the larger the Q effects measured from the seismic image, and the further the current Q model is from the accurate Q model – and vice versa. Therefore, the objective of this image-based Q inversion is to minimize the summation of $\rho(x; Q)$ over all image points. I have derived objective functions to measure $\rho$ from two different image domains: (1) migrated images at zero subsurface offset (referred as **stacked WEMQA**) and (2) ADCIGs (referred as **prestack WEMQA**). As described in Chapter 2, inversion using a prestack objective function is able to produce higher resolution, more accurate Q inversion results, although its computational cost is higher than inversion using a poststack objective function. In this section, I apply both the stacked and prestack WEMQA using one-way downward continuation and compare their results.

Before Q updating, the seismic image (Figure 5.25(a)) migrated using the updated velocity model and the initial Q model has only been compensated by the background Q value of 500. The image under the interpreted Q anomalies is wiped out. The migration frequency range and imaging grid are the same as in the 2D one-way WEMVA application.

To perform stacked WEMQA, I choose the trace at 33,880 m as the reference trace to compute $\rho$. This trace is far from both the shallow gas and the channel, so it is assumed to be the least affected by the attenuation that occurs at these anomalies. The window size to compute the spectra from the migrated image for $\rho$ is 500 m in Z direction and 125 m in the X direction. I have developed an automatic picker to find $k_c$, the wavenumber where the computed spectra reaches its peak. The desired wavenumber range that I choose to compute $\rho$ is $[k_c - 0.015$ 1/m, $k_c + 0.015$ 1/m$]$. The velocity stretch effect in the migrated image is also corrected before spectral analysis for $\rho$ using Equation 2.13.

By plotting the logarithm of the spectral ratio, we can distinguish attenuated regions which yield a plot with a negative slope from non-attenuated regions which result in a nearly flat plot. Figure 5.16(a) is the logarithm of the spectral ratio from the attenuated image ( Figure 5.10(b)) between the window below the left Q anomaly in which the window center is at $x = 27,500$ m, $z = 2,500$ m and the reference window in which the window center is at $x = 33,880$ m, $z = 2,500$ m. Figure 5.16(b) is the logarithm of the spectral ratio from the attenuated image (Figure 5.10(b)) between the window far from these two Q anomalies in which the window center is at $x = 34,500$ m, $z = 2,500$ m and the reference window in which the window center is at $x = 33,880$ m, $z = 2,500$ m. The wavenumber range for slope computation of these two locations is roughly within [0.005 1/m, 0.035 1/m], because the signal-to-noise level within this wavenumber range is relatively high. Within this wavenumber range and regardless of the noisy wiggles, the curve in Figure 5.16(a) decreases linearly with wavenumber with a negative slope; while the curve in Figure 5.16(b) is almost flat with its slope value approximating to 0. These two slope values indicate the chosen window below the left Q anomaly is attenuated, and the chosen window far from these two Q anomalies has almost no attenuation.

To remove the influence of noise on the spectra, I use linear least-squares regression to fit a line to the log spectral ratio curves within the selected wavenumber range.

Figure 5.17 shows the slope estimate of small windows around each point in the image in Figure 5.10(b). I clipped the positive numbers to display the attenuated region only. The slope values at certain image points of the attenuated image in Figure 5.10(b) are positive. There are two possible explanations: the chosen reference trace is not actually the least affected by attenuation, or a more sophisticated wavenumber range picking method is needed. In accordance with the observation from Figure 5.10(b), two strong attenuation regions under the salt domes are highlighted by the blue in Figure 5.17. However, the blue regions below a 4 km depth are unexpectedly distributed, possibly because of the poor image quality below the base of salt. Fortunately, this deep part of the image has little impact on the estimation of shallow Q anomalies.

The stacked WEMQA inversion yields an improved image after 20 iterations. The resulting Q model, shown on a logarithmic scale in Figure 5.18, shows two anomalies above the salt that are both shifted to the left of these two salt domes. The stacked WEMQA has the disadvantage of producing a low-resolution result, which is part of the reason for the difference between the estimated location and the interpreted location of the anomalies. In addition, the right anomaly attenuates waves more than the left one, which contradicts the initial interpretation that the gas on the left causes stronger attenuation than the right channel. The objective function (Figure 5.19) of the stack WEMQA shows that the inversion makes little progress after 13 iterations.

To perform prestack WEMQA, I choose the angle gather in which the midpoint is at 33,880 m as the reference gather to compute $\rho$, which is considered to be the least attenuated by two Q anomalies. This angle gather is compared to the rest of the angle gathers to compute the slope. The window size used to compute the spectra from the migrated image for $\rho$ has only one direction along the depth with the length of 300 m. The smaller window size aims for higher-resolution Q inversion results. The automatic picker for the desired wavenumber range is the same as in stacked WEMQA. The velocity stretch effect and angle stretch effect (Shen et al., 2015) in the ADCIGs are also corrected before spectral analysis for $\rho$ using Equation 2.13.

The ADCIGs at the first iteration of prestack WEMQA have only been compensated by the background Q value of 500. Figure 5.20 displays the slope estimate of these 9 representative ADCIGs. Every point in the angle gathers are the center of the windows for computing the slope. The strongly attenuated areas mostly show

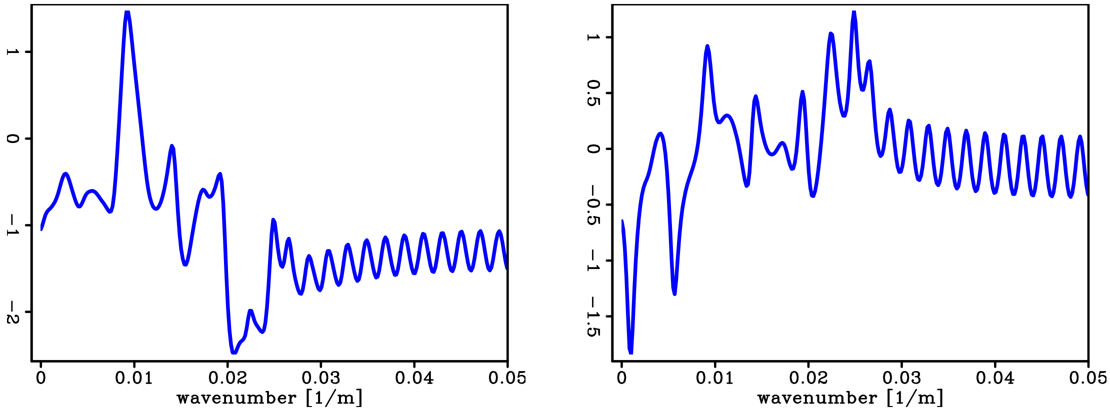

(a)

(b)

Figure 5.16: (a) The logarithm of the spectral ratio from the attenuated image ( Figure 5.25(a)) between the window below the left Q anomaly in which the window center is at $x = 27,500$ m, $z = 2,500$ m and the reference window in which the window center is at $x = 33,880$ m, $z = 2,500$ m. (b) The logarithm of the spectral ratio from the attenuated image ( Figure 5.25(a)) between the window far from these two Q anomalies in which the window center is at $x = 34,500$ m, $z = 2,500$ m and the reference window in which the window center is at $x = 33,880$ m, $z = 2,500$ m. [**CR**] chap5/. dlp2D-iqtv-post-basc-rati-att,dlp2D-iqtv-post-basc-rati-ref

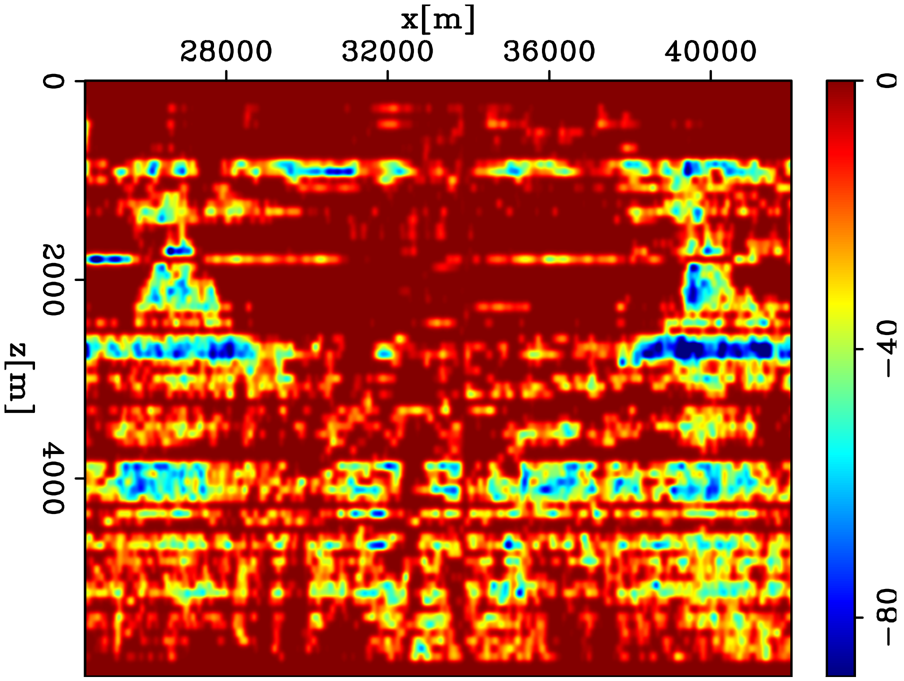

Figure 5.17: The slope estimate of the image in Figure 5.25(a) for every image point that is used as the window center. I clipped the positive numbers to display the attenuated region only. The blue color in the slope map indicates the areas strongly attenuated. [**CR**] chap5/. dlp2D-iqtv-post-basc-slopsft-iter0

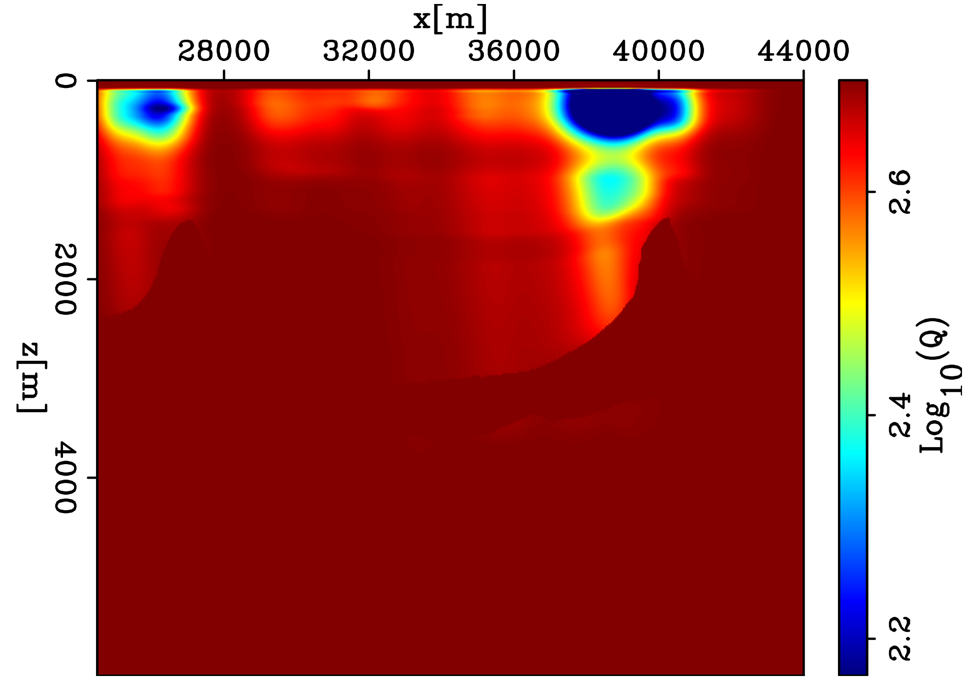

Figure 5.18: The inverted Q model displayed in logarithm scales ($\log_{10} Q$) after 20 iterations using stacked WEMQA. [**CR**] chap5/. dlp2D-iqtv-post-basc-bq-iter20

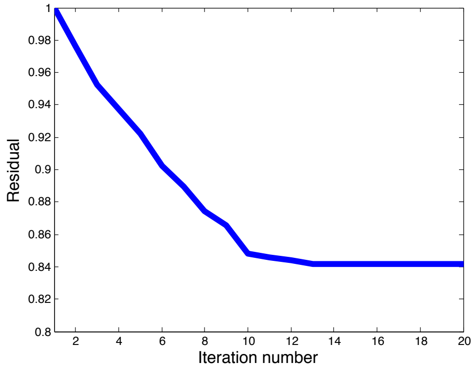

Figure 5.19: Normalized curve for the objective function of the one-way stack WEMQA. The curve is normalized by the value of the objective function at the first iteration. [**NR**] chap5/. dlp2D-one-stk-fobj-Q

up below Q anomalies ($z < 1,500$ m) and above the base of the salt ($z > 4,000$ m). Again, the image below the base of the salt ($z > 4,000$ m) has little impact on the Q inversion. Therefore, I only focus the analysis below Q anomalies ($z < 1,500$ m) and above the base of salt ($z > 4,000$ m).

With this depth range, the gathers in which the midpoint is far from the Q anomalies area (e.g., $x = 31$ km, $x = 33$ km and $x = 35$ km in Figure 5.30(a)) have little attenuated region indicated by blue. As the midpoint moves closer to the Q anomalies (e.g., $x = 25$ km, $x = 29$ km and $x = 37$ km in Figure 5.30(a)), the waves propagating at large angles pass through the Q anomalies; and therefore, the far angles at these ADCIGs are attenuated. Once the midpoint is in the anomalous area (e.g., $x = 27$ km, $x = 39$ km and $x = 41$ km in Figure 5.30(a)), their near angles are attenuated. Figure 5.21 shows the zero-angle slope estimated measured from the attenuated ADCIGs with its blue color highlighting two strong attenuated regions within the salt domes.

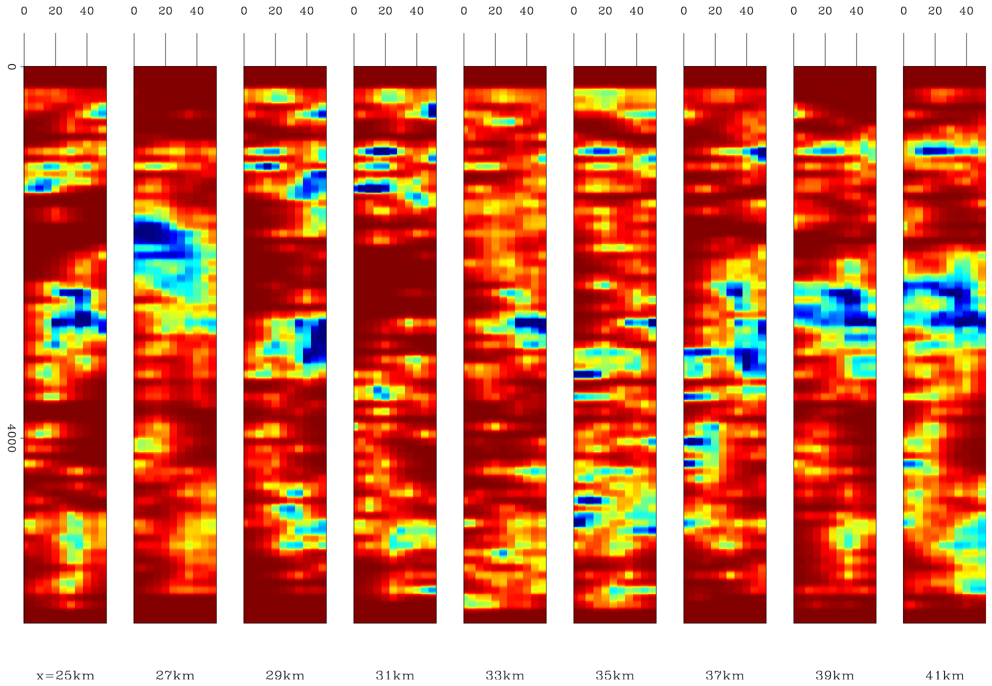

Figure 5.20: The slope estimate of the ADCIGs at the first iteration of inversion for Q model updating. The slope estimates of 9 representative ADCIGs are displayed. Every point in the angle gathers are the center of the windows for computing the slope. I clipped the positive number to display the attenuated regions only. The blue color in the slope map indicates the strongly attenuated area.The vertical axis is depth in meters. **[CR]** chap5/. dlp2D-iqtv-pre-basc-slopsft-iter0

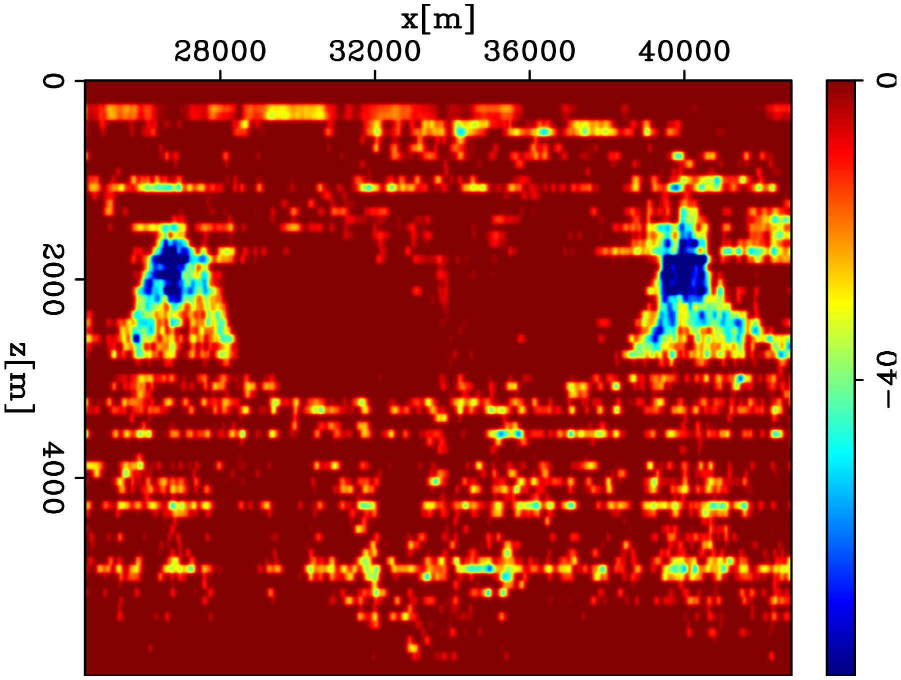

Figure 5.21: The slope estimate of the ADCIGs at the first iteration of inversion for Q model updating. The slope estimates extracted at the zero angle are displayed. [**CR**] chap5/. dlp2D-iqtv-pre-basc-slop0-iter0

Figure 5.22 shows the Q gradient at the first iteration of the inversion for Q with a prestack objective function, in which search direction has opposite polarity of the gradient. The gradient shows updates are strong around the shallow gas and channel region that exhibit the highest attenuation. Figure 5.23 is the inverted Q model displayed in logarithm scales ($\log_{10} Q$) after 20 iterations for Q inversion. The inverted Q models recover two Q anomalies. Because the prestack WEMQA produces higher resolution results, the shapes of the Q anomalies in Figure 5.23 are more compact and contained to the region where the channel and gas cloud are interpreted, when compared with the ones in Figure 5.18. This result also suggests that stacked WEMQA leads to a more accurate Q model than prestack WEMQA. The objective function (Figure 5.24) of the prestack WEMQA shows that the inversion makes little progress after 11 iterations. The residual does not drop much, because the images are mainly updated near the Q anomalies regions, as shown in Figure 5.26.

If we migrate the data with the updated velocity model and the inverted Q model after prestack WEMQA inversion, we observe that the structures at the gas and channel regions become brighter. These bright spots match the interpretation that

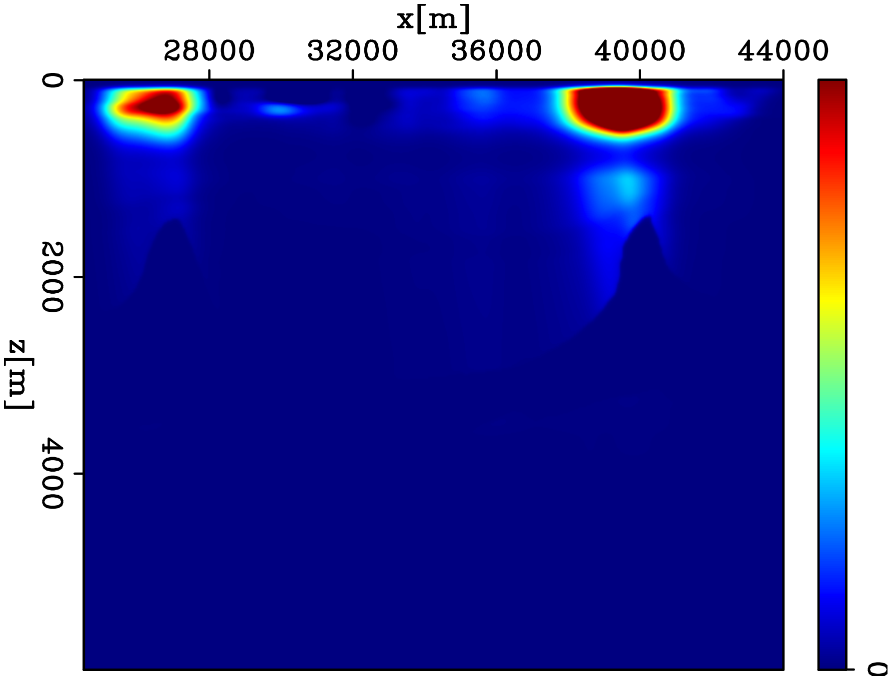

Figure 5.22: The Q gradient at the first iteration of inversion for Q model updating, in which the sign is opposite to the search direction. [**CR**] chap5/. dlp2D-iqtv-pre-basc-grdp-iter0

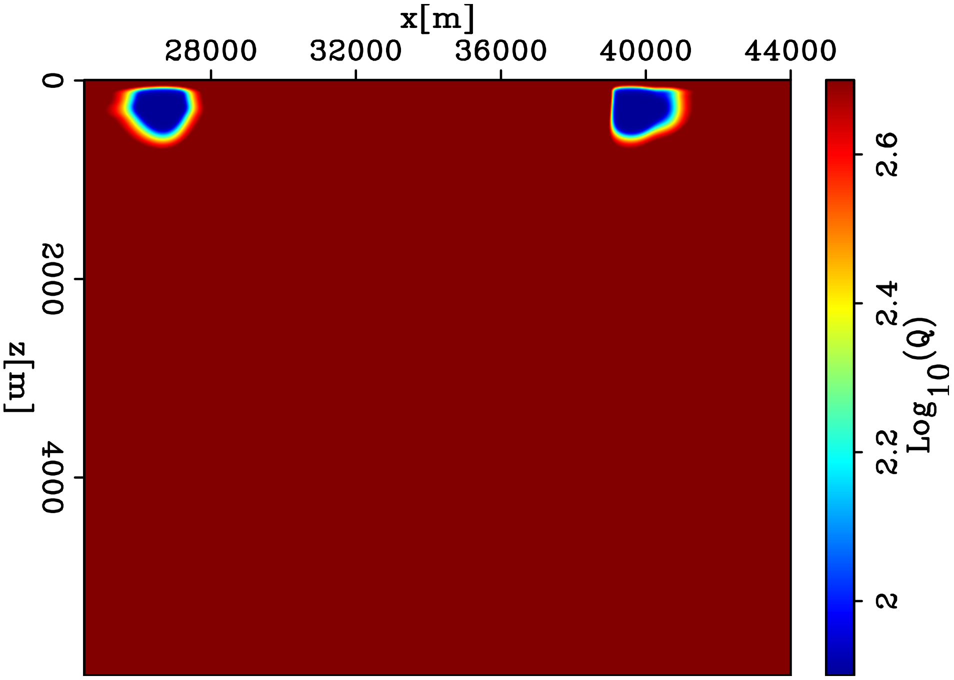

Figure 5.23: The inverted Q model displayed in a logarithmic scale ($\log_{10} Q$) after 20 iterations using prestack WEMQA. [**CR**] chap5/. dlp2D-iqtv-pre-basc-bq-iter20

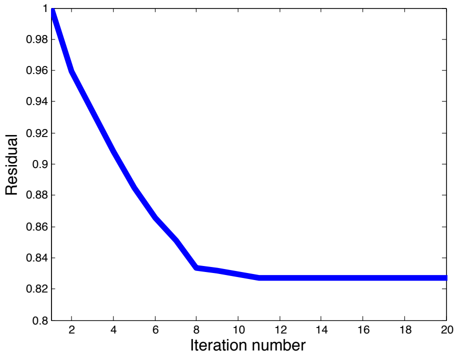

Figure 5.24: Normalized curve for the objective function of the prestack WEMQA. The curve is normalized by the value of the objective function at the first iteration. [**NR**] chap5/. dlp2D-one-fobj-Q

the strong impedance contrast makes seismic reflection amplitudes strong. The compensated image in Figure 5.25(b) shows enhanced amplitudes and higher frequency content below the Q anomalies. To take a closer examination, I zoom in on the region to the left and right of the salt domes (see the highlighted boxes in Figure 5.25) and show them in Figure 5.27 and Figure 5.28, respectively. Because more high frequency information is recovered in the compensated image, events appear sharper. Also the compensated events become more coherent because of attenuation-induced phase distortion being corrected, as highlighted by the yellow arrows. The spectra of events below the right Q anomaly, seen in Figure 5.29, shows the compensation with the inverted Q model whitens the spectra and compensates for the higher frequency loss caused by attenuation.

Figures 5.30 shows 10 representative ADCIGs of this migrated image before and after Q updating. The ADCIGs compensated by the inverted Q model have sharper, more coherent events. This improvement aides the gather picking for velocity analysis and to AVO analysis for reservoir characterization.

## 2D two-way WEMQA application

To compare two-way WEMQA to one-way WEMQA, I tested it on the same 2D section of CNS data. The two-way WEMQA method has higher computation cost and memory requirements than one-way WEMQA as described in Chapter 2. To

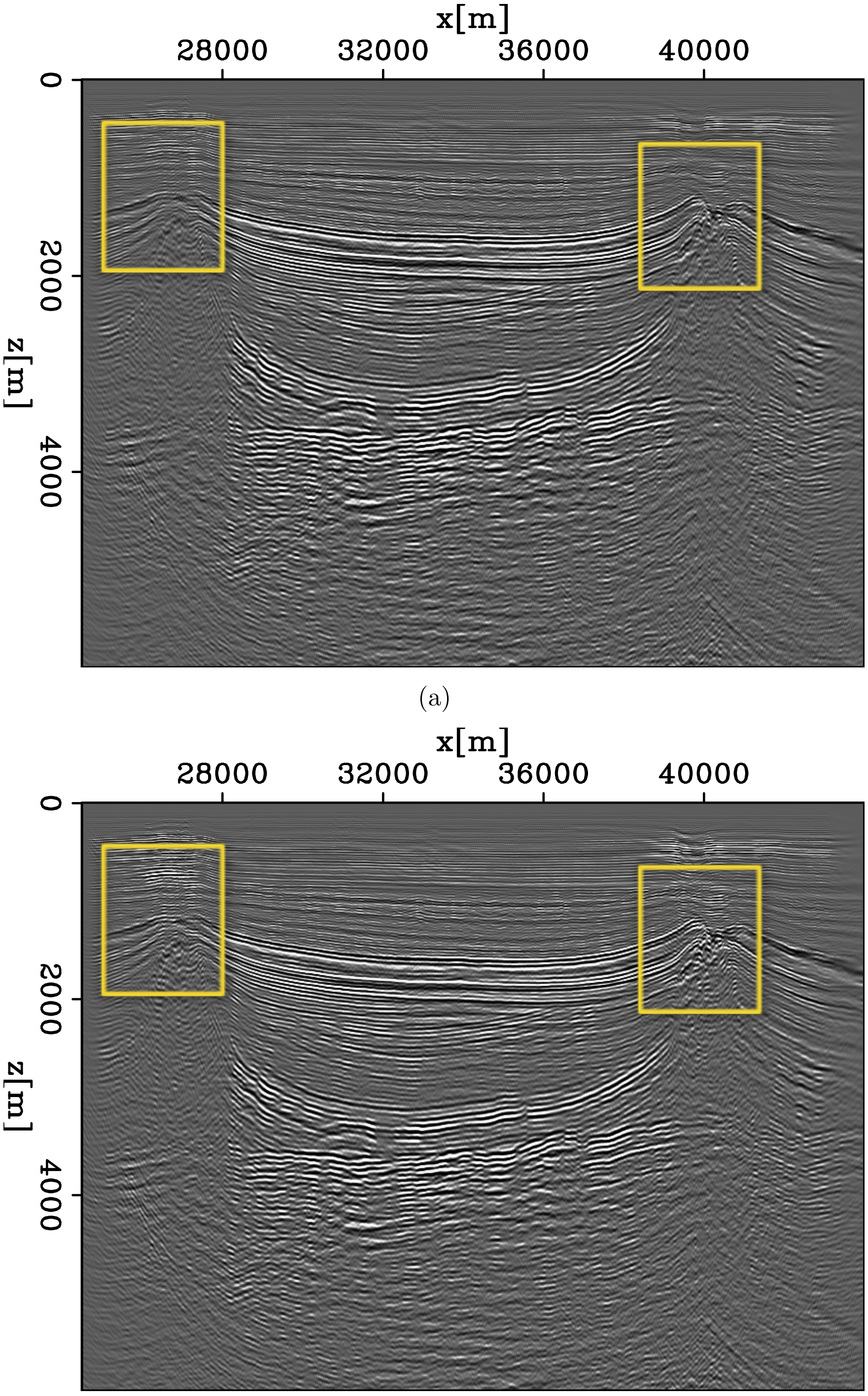

(a)

(b)

Figure 5.25: (a) The migrated image at zero subsurface offset using the updated velocity model and the initial Q model. Same as Figure 5.10(b). Replicate the figure here for a convenient comparison with Figure 5.25(b). (b) The migrated image at zero subsurface offset using the updated velocity model and the updated Q model. The yellow box highlights the zoom-in region shown in Figure 5.27 and Figure 5.28. The amplitude enhancement is much more obvious on left than on right of image. [**CR**]

chap5/. dlp2D-iqtv-pre-basc-bimg-before-ann,dlp2D-iqtv-pre-basc-bimg-after-ann

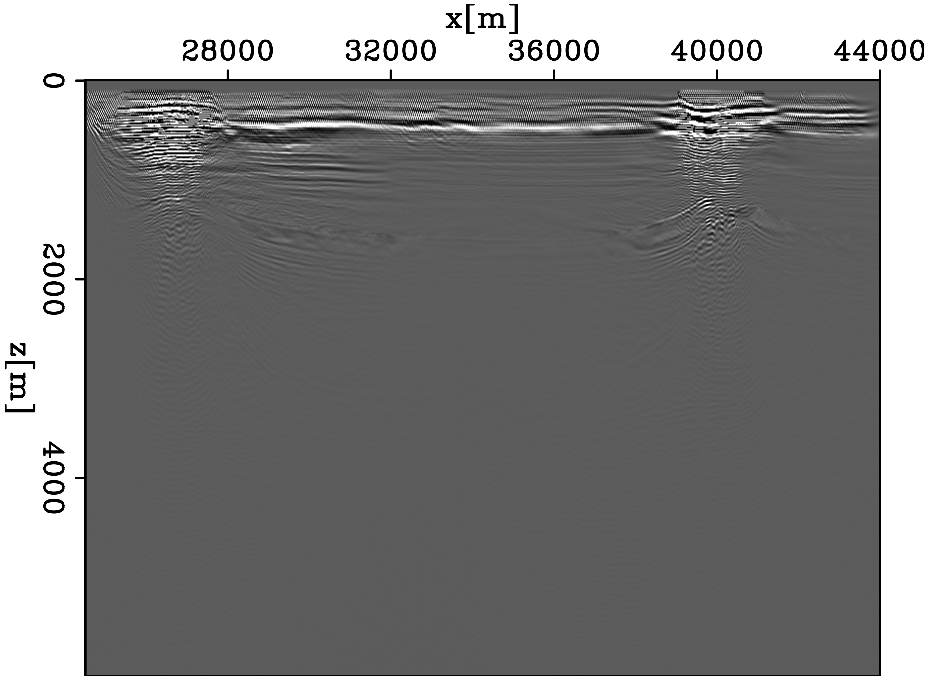

Figure 5.26: The image difference between Figure 5.25(b) and Figure 5.25(a). [**CR**]
chap5/. dlp2D-iqtv-pre-basc-resd

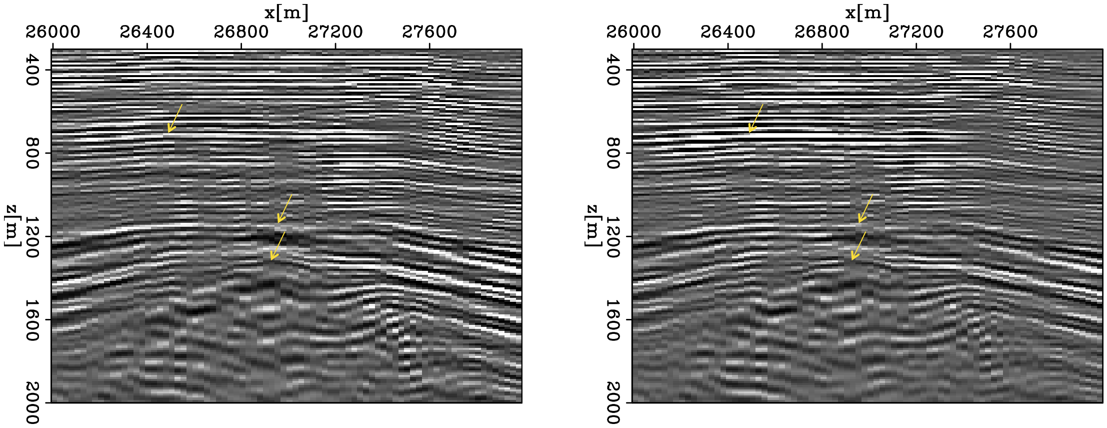

(a)

(b)

Figure 5.27: Zoomed-in region around the left side of the salt dome of (a) the attenuated image in Figure 5.25(a) and (b) the compensated image in Figure 5.25(b). The amplitudes are gained at the deeper depth using $z^2$. The events pointed to by yellow arrows become sharper and more coherent. [**CR**]
chap5/. dlp2D-iqtv-pre-basc-reg1-before-nagc-ann,dlp2D-iqtv-pre-basc-reg1-after-nagc-ann

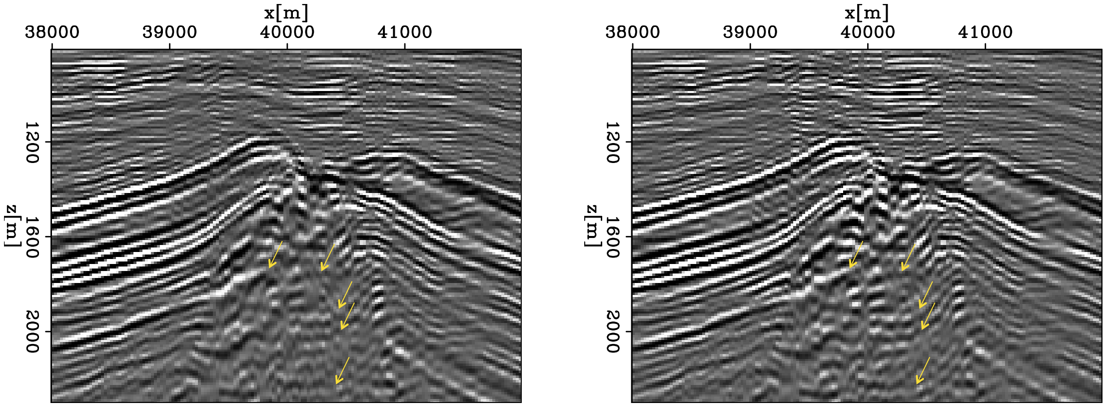

(a) (b)

Figure 5.28: Zoomed-in region around the right side of the salt dome of (a) the attenuated image in Figure 5.25(a) and (b) the compensated image in Figure 5.25(b). The amplitudes are gained at the deeper depth using $z^2$. The events pointed to by yellow arrows become sharper and more coherent. [**CR**] chap5/. dlp2D-iqtv-pre-basc-reg2-before-nagc-ann,dlp2D-iqtv-pre-basc-reg2-after-nagc-ann

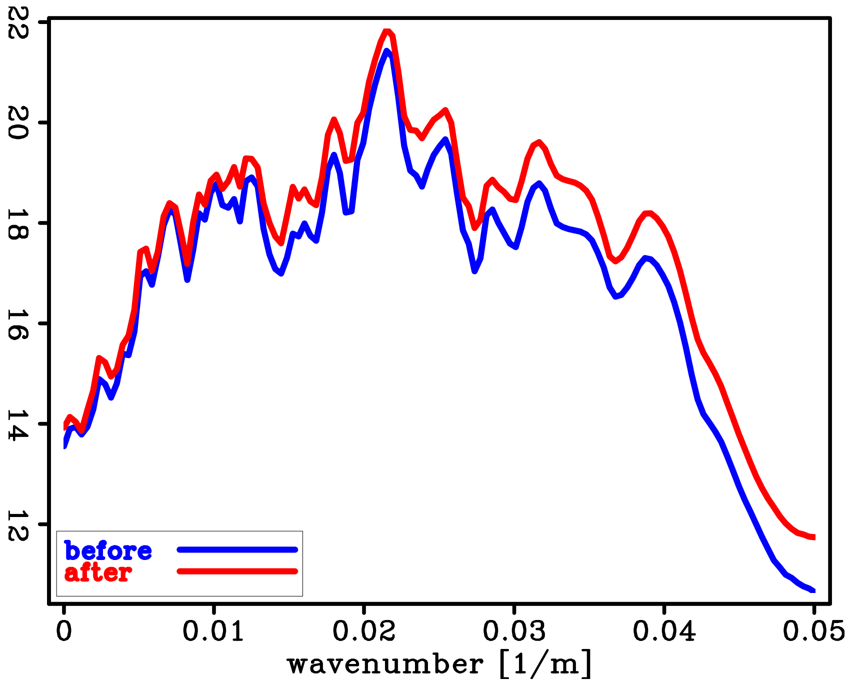

Figure 5.29: The spectra of the events below the right Q anomaly of Figure 5.25(a) in blue and Figure 5.25(b) in red. The spectra are displayed in the logarithm scale. [**CR**] chap5/. dlp2D-iqtv-pre-basc-spex

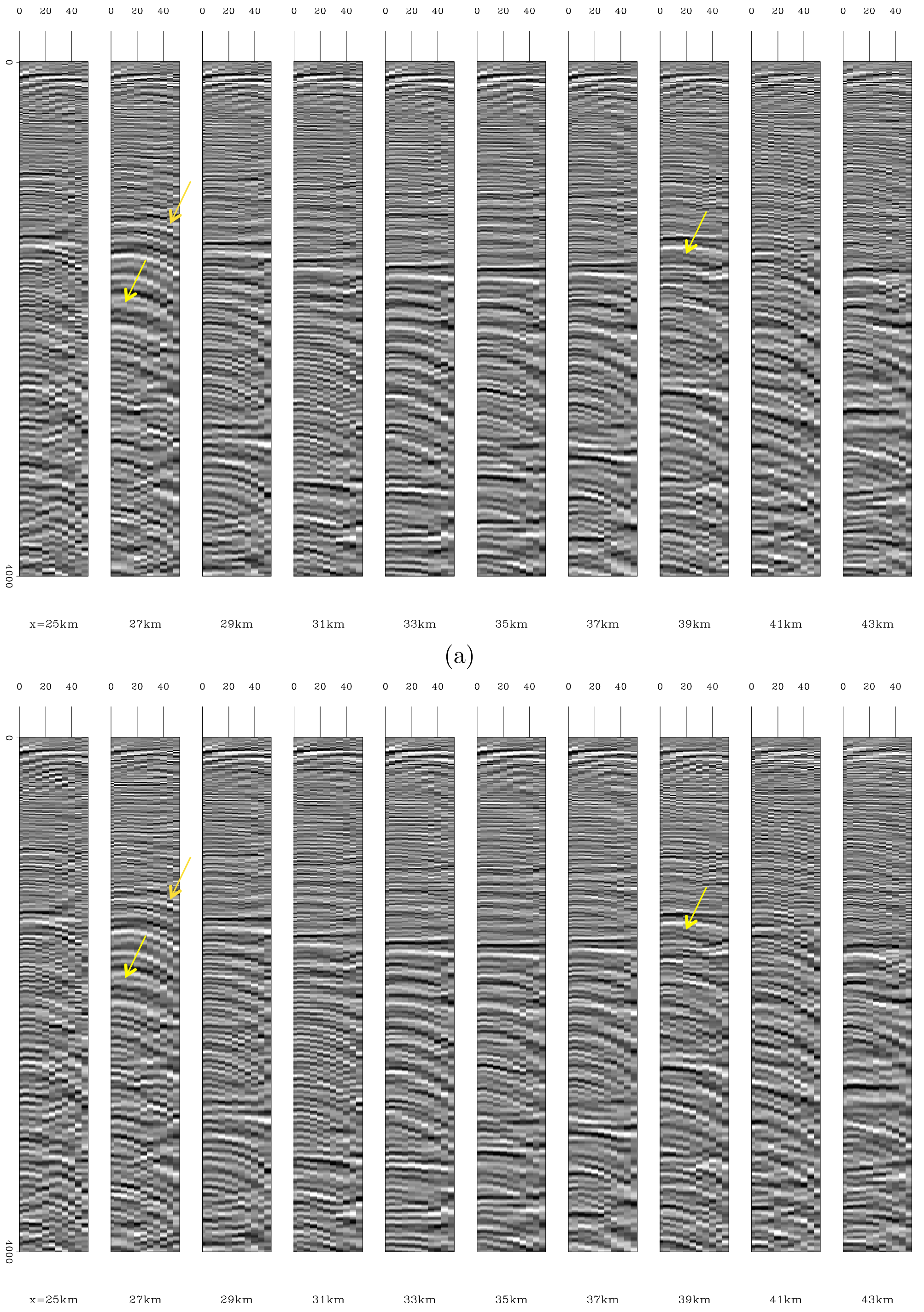

(a)

(b)

Figure 5.30: (a) The ADCIGs using the updated velocity model and the initial Q model. AGC is applied. (b) The ADCIGs using the updated velocity model and the inverted Q model. AGC is applied. The vertical axis is depth in meters. The events are sharper and more coherent. Examples are highlighted by yellow arrows. [**CR**] chap5/. dlp2D-iqtv-pre-basc-bang-before-ann,dlp2D-iqtv-pre-basc-bang-after-ann

stay within our computational resources, in this section, I only apply stacked two-way WEMQA to invert for the Q model with prior knowledge of the velocity model (Figure 5.13).

As a baseline, I migrated the data using the updated velocity model (seen in Figure 5.13) and an initial Q model with a constant value of 500 and show the image in Figure 5.35(a). Again, the migration frequency range is from 0.8 Hz to 50 Hz. The spacing of the imaging grid used is 12.5 m in X by 10 m in Z. Because the salt flank has gentle slope, the migrated image using the two-way method shows little improvement in imaging the salt when compared with the image using the one-way method. Although the image of Figure 5.35(a) is similar to Figure 5.10(a), it still has fewer migration artifacts than Figure 5.10(a). For example, the migration "smiles" below 4,000 m are reduced.

To perform two-way WEMQA, I set all the parameters for the inversion to be the same as the ones used in one-way stacked WEMQA. I choose the trace at 33,880 m as the reference trace to compute $\rho$. The window size to compute the spectra from the migrated image for $\rho$ is 500 m in Z direction and 125 m in X direction. The velocity stretch effect in the migrated image is also corrected before spectral analysis for $\rho$ using Equation 2.13.

The attenuated image shows attenuation below the Q anomaly, but almost no attenuation far from the Q anomaly, which is made apparent from the slopes of the log spectral ratio in these regions seen in Figure 5.31. Figure 5.31(a) is the logarithm of the spectral ratio from the attenuated image ( Figure 5.35(a)) between the window below the left Q anomaly in which the window center is at $x = 27,500$ m, $z = 2,500$ m and the reference window in which the window center is at $x = 33,880$ m, $z = 2,500$ m. Figure 5.31(b) is the logarithm of the spectral ratio from the attenuated image (Figure 5.35(a)) between the window far from these two Q anomalies in which the window center is at $x = 34,500$ m, $z = 2,500$ m and the reference window in which the window center is at $x = 33,880$ m, $z = 2,500$ m. The wavenumber range for slope computation of these two locations is roughly within [0.005 1/m, 0.035 1/m], becasue the signal-to-noise level within this wavenumber range is relatively high. Within this wavenumber range and regardless of the noisy wiggles, the curve in Figure 5.31(a) decreases linearly with wavenumber with a negative slope; while the curve in Figure 5.31(b) is almost flat with its slope value approximating to 0. Because the two-way

WEMQA produces a cleaner image than the one-way image, the curves are cleaner than the ones obtained by one-way method. These two slope values indicate the chosen window below the left Q anomaly is attenuated, and the chosen window far from these two Q anomalies has almost no attenuation.

Figure 5.32 shows the slope estimate of small windows around each point in the image in Figure 5.35(a). In accordance with the observation from Figure 5.17, two strong attenuation regions under the salt domes are highlighted by the blue in Figure 5.32. The two-way method produces a slightly cleaner image than the one produced by the one-way migration. The image migrated using two-way method has less high wavenumber artifacts in the attenuating regions. As a result, the attenuating regions are slightly wider than those than those produced by the one-way stacked WEMQA shown in Figure 5.17,

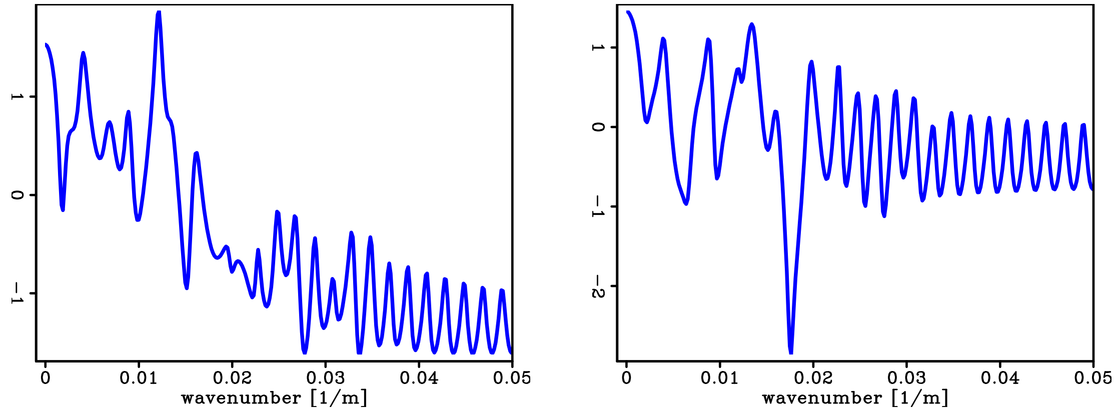

(a) (b)

Figure 5.31: (a) The logarithm of the spectral ratio from the attenuated image ( Figure 5.35(a)) between the window below the left Q anomaly in which the window center is at $x = 27,500$ m, $z = 2,500$ m and the reference window in which the window center is at $x = 33,880$ m, $z = 2,500$ m. (b) The logarithm of the spectral ratio from the attenuated image ( Figure 5.35(a)) between the window far from these two Q anomalies in which the window center is at $x = 34,500$ m, $z = 2,500$ m and the reference window in which the window center is at $x = 33,880$ m, $z = 2,500$ m. [**CR**] chap5/. dlp2D-iqtv-pre-rtm-rati-att,dlp2D-iqtv-pre-rtm-rati-ref

Figure 5.33 is the inverted Q model displayed on a logarithmic scale ($\log_{10} Q$) after 20 iterations using the two-way WEMQA inversion. The resulting Q model is similar to the one-way stacked WEMQA result (Figure 5.18). However, the inverted anomalies have larger size in Figure 5.33, because the slop map shows larger attenuated regions in Figure 5.32. The objective function (Figure 5.24) of the two-way

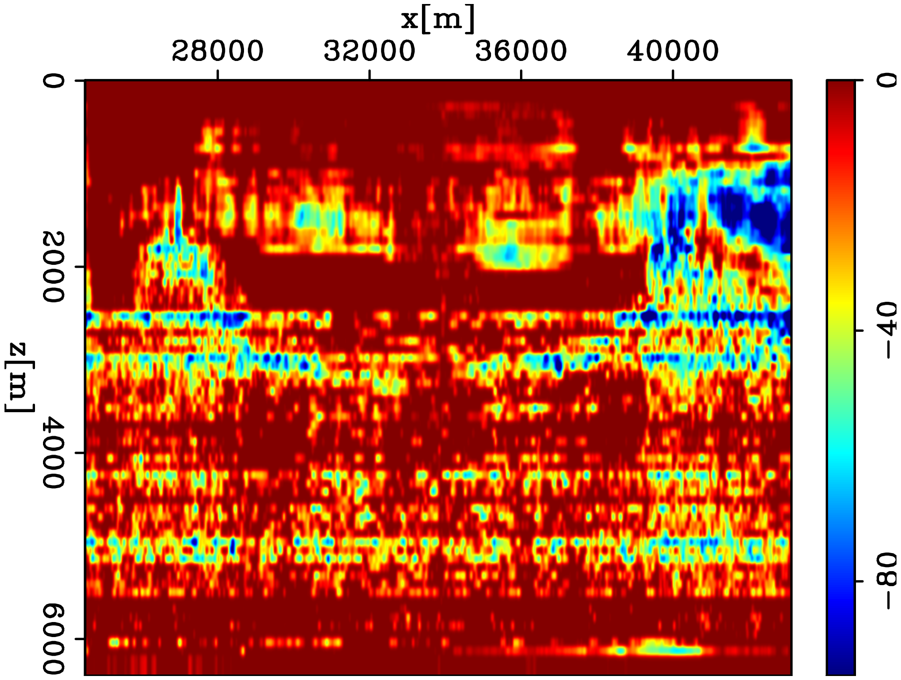

Figure 5.32: The slope estimate of the image in Figure 5.35(a) for every image point that is used as the window center. I clipped the positive numbers to display the attenuated region only. The blue color in the slope map indicates the areas strongly attenuated. [**CR**] chap5/. dlp2D-iqtv-pre-rtm-slop-iter0

WEMQA shows that the inversion is converged after 10 iterations, which is slightly faster than one-way stack WEMQA inversion.

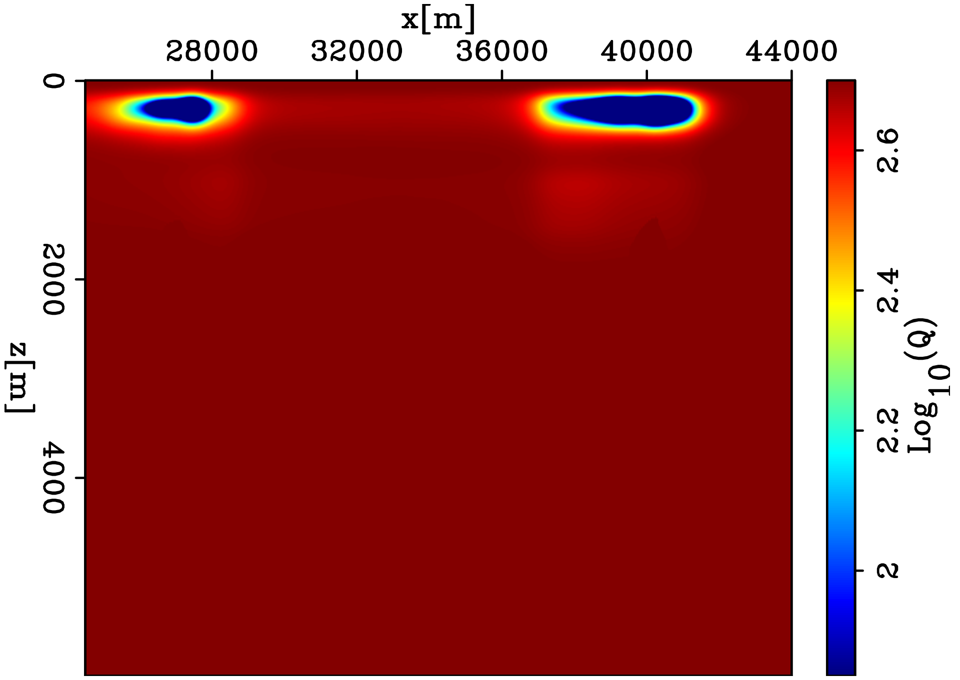

Figure 5.33: The inverted Q model displayed in logarithm scales ($\log_{10} Q$) after 20 iterations using two-way WEMQA. [**CR**] chap5/. dlp2D-iqtv-pre-rtm-bq-iter20

Figure 5.35(b) is the migrated image at zero subsurface offset using the updated velocity model (Figure 5.13) and the inverted Q model (Figure 5.33). The structures at the gas and channel regions become brighter. These bright spots match the interpretation that the strong impedance contrast makes seismic reflection amplitudes strong. The compensated image in Figure 5.35(b) shows enhanced amplitudes and higher frequency content below the Q anomalies.

## 3D WEMVA AND WEMQA APPLICATION

The inversion workflow developed on the 2D subset of the CNS dataset serves as a guide to inverting the full 3D dataset. I first update the velocity model using WEMVA. Then I invert for the Q model using one-way prestack WEMQA. I use the software `Sep_cube` developed by Stanford Exploration Project to display the 3D volume. In the following section, all the figures using `Sep_cube` display the section

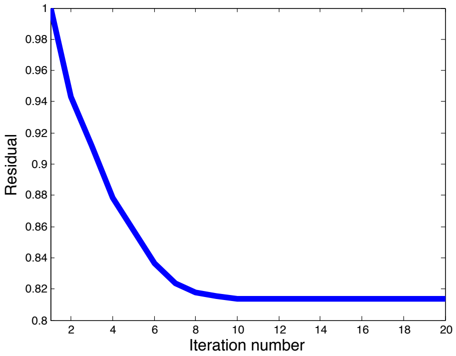

Figure 5.34: Normalized curve for the objective function of the two-way WEMQA. The curve is normalized by the value of the objective function at the first iteration. [**NR**] chap5/. dlp2D-two-fobj-Q

at a shallow depth of x=39,000 m, y=7,500 m, z=360 m. The 3D inversion workflow employs the same parameter sets as the ones used in the above 2D one-way applications.

## 3D WEMVA application

The initial velocity model for the 3D velocity inversion provided by Dolphin is shown in Figure 5.37(a). Figure 5.39(a) and Figure 5.40(a) show 3D views of the migrated images using the initial velocity model at different depth. Based on Dolphin's interpretation, the right highlighted region is the channel with lower velocity and weaker attenuation; while the left highlighted region is the shallow gas with low velocity and stronger attenuation. The shallow horizontal stripes shown in the depth slice of Figure 5.39(a) are an artifact of the acquisition footprint, particularly the sparse 300 m shot spacing. The initial velocity model shown in Figure 5.37(a) has a nearly constant velocity around the shallow channel and gas features. Figure 5.37(b) is the updated velocity model after 8 iterations. The velocity difference between the updated velocity (Figure 5.37(b)) and the initial velocity (Figure 5.37(a)) is shown in Figure 5.38. The results show noticeable velocity drops in the highlighted regions that match the interpreted gas and channel regions in Figure 5.39(a). The stacking power (normalized by the stacking power in the last iteration) curve (Figure 5.15) shows fast convergence in the first few iterations. The objective function curve shows

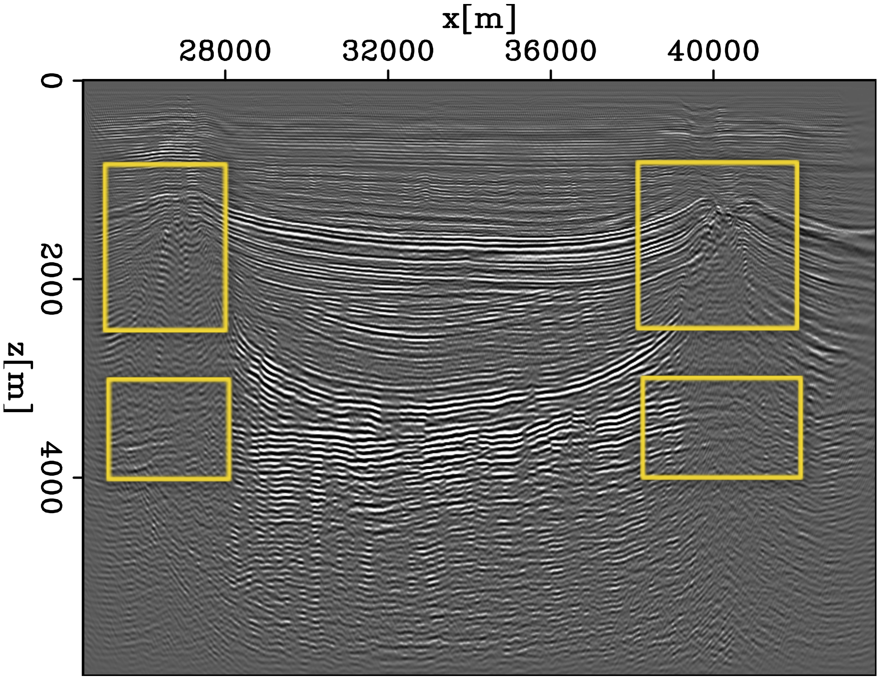

(a)

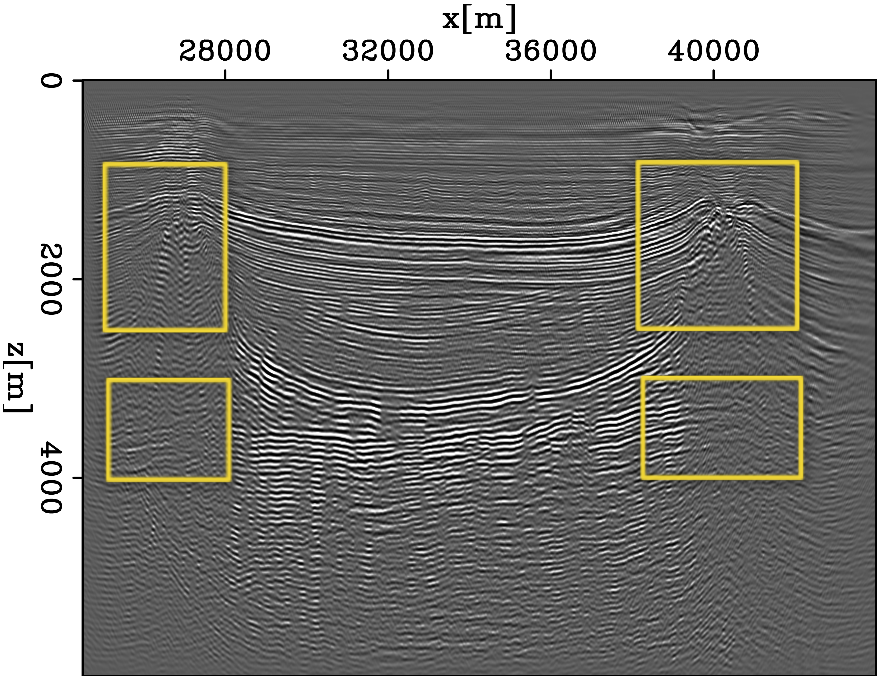

(b)

Figure 5.35: (a) The migrated image at zero subsurface offset using the updated velocity model and the initial Q model. (b) The migrated image at zero subsurface offset using the updated velocity model and the inverted Q model, as shown in Figure 5.33. The yellow box highlights the major updates. [**CR**] chap5/. dlp2D-iqtv-pre-rtm-bimg-before-ann,dlp2D-iqtv-pre-rtm-bimg-after-ann

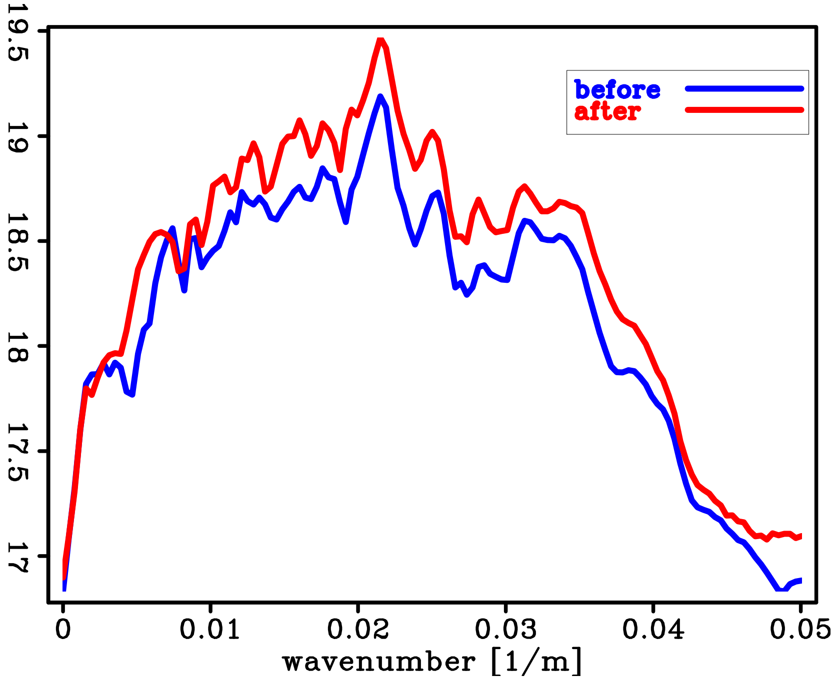

Figure 5.36: The spectra of the events below the right Q anomaly of Figure 5.35(a) in blue and Figure 5.35(b) in red. The spectra are displayed in the logarithm scale. [**CR**] chap5/. dlp2D-iqtv-pre-rtm-spex

little improvement after five iterations.

Figure 5.39(b) and Figure 5.40(b) show 3D views of the seismic image at different depth at zero subsurface offset migrated using the updated velocity model and the initial Q model. Shallow velocities in the updated model are slower than in the initial model, particularly around the two anomalies. As a result, deeper events in the migration with the updated velocity model move up. The updated velocity also improves the coherency of the events in the migrated image. For example, the left shallow gas in the depth slice of Figure 5.39(b) shows a cleaner and more coherent contour.

Figure 5.42(a) shows 10 representative ADCIGs of the image migrated using the updated velocity model and the initial Q model. The decrease in shallow velocities after inversion pushes the curvature of events in ADCIGs upwards, and therefore flattens the gathers that previously curved down.

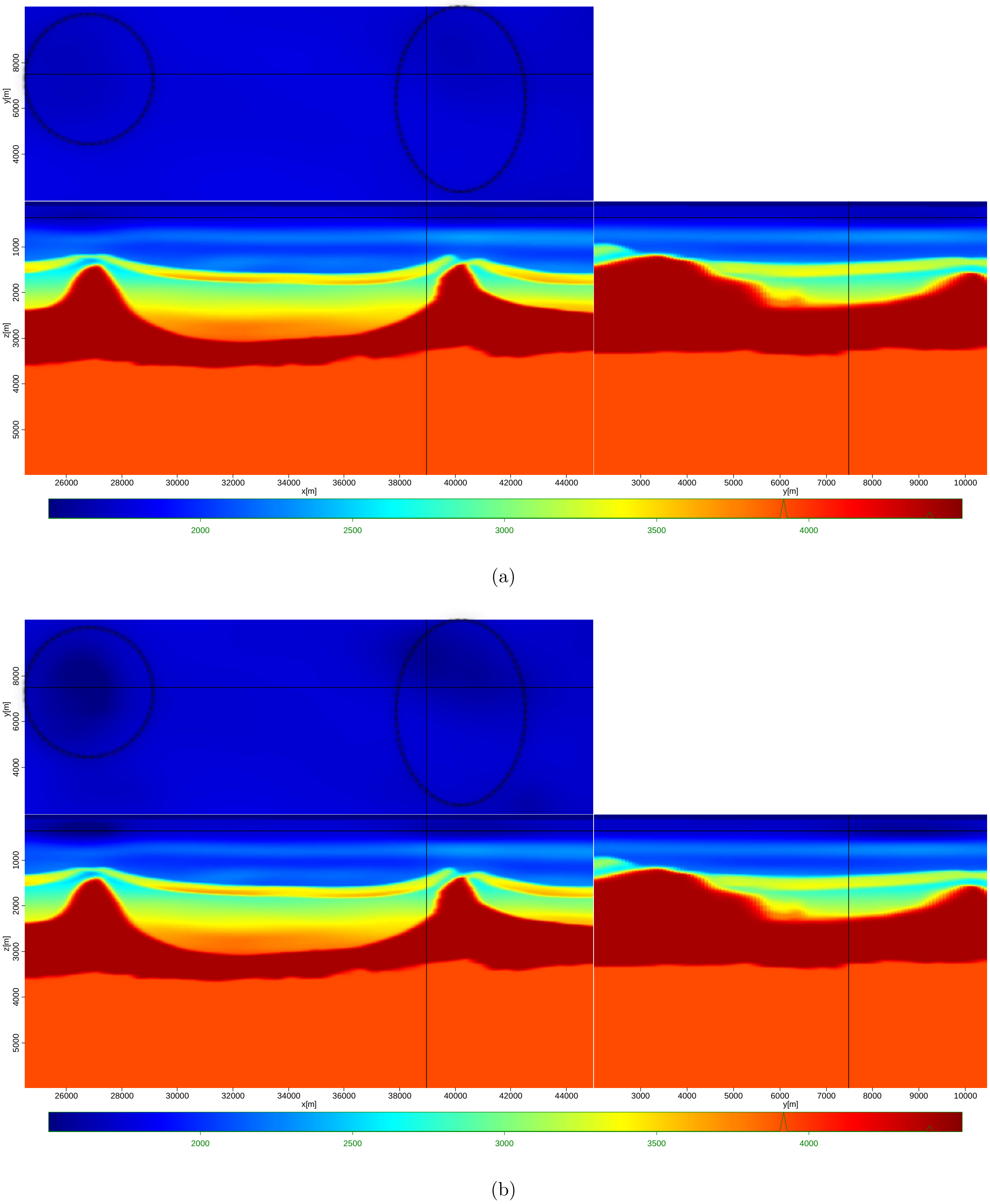

(a)

(b)

Figure 5.37: (a) The initial velocity model; (b) the updated velocity model after 8 iterations. **[CR]**

chap5/. dlp3D-bqiv-pre-basc-bvel-iter0-ann,dlp3D-bqiv-pre-basc-bvel-iter8-ann

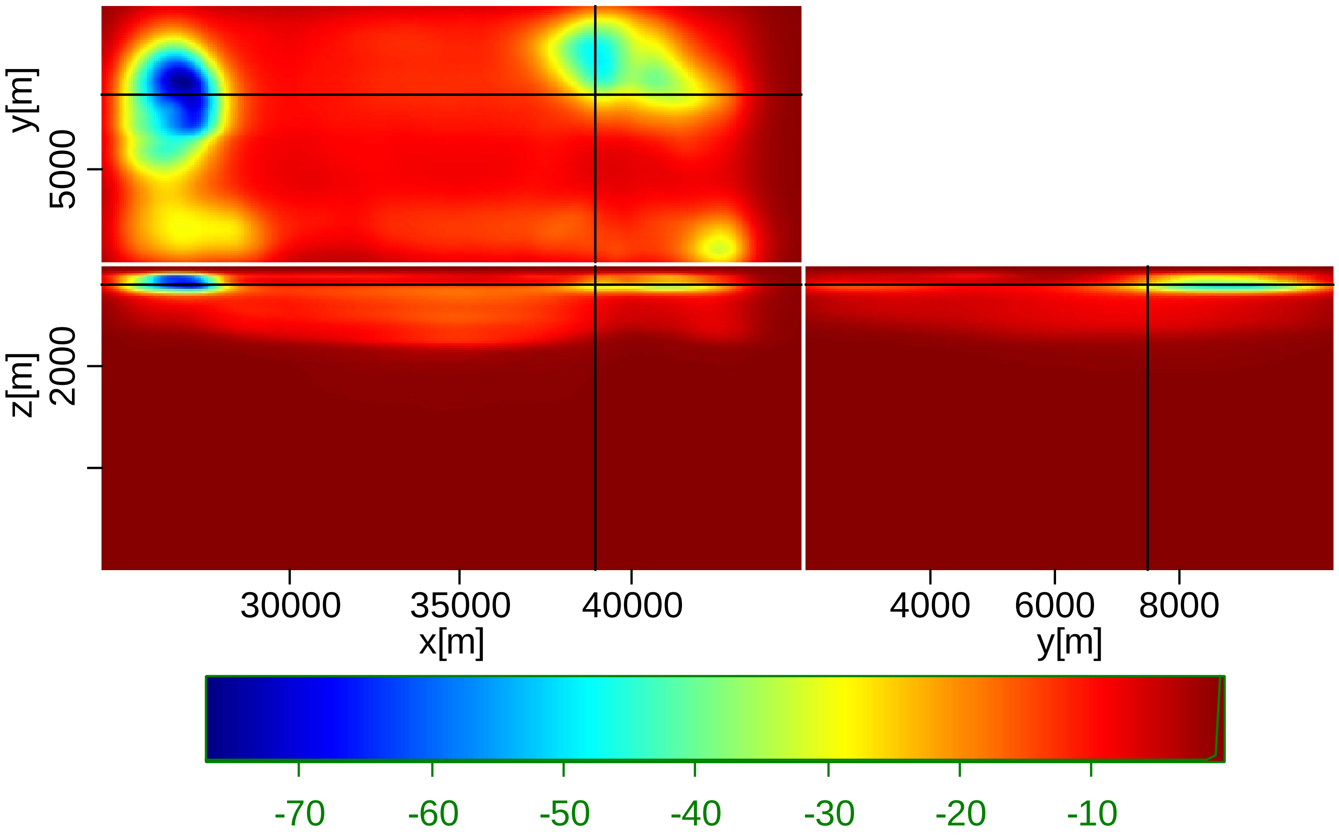

Figure 5.38: The velocity difference between the updated velocity (Figure 5.37(b)) and the initial velocity (Figure 5.37(a)). [**CR**] chap5/. dlp3D-bqiv-pre-basc-bvel-resd

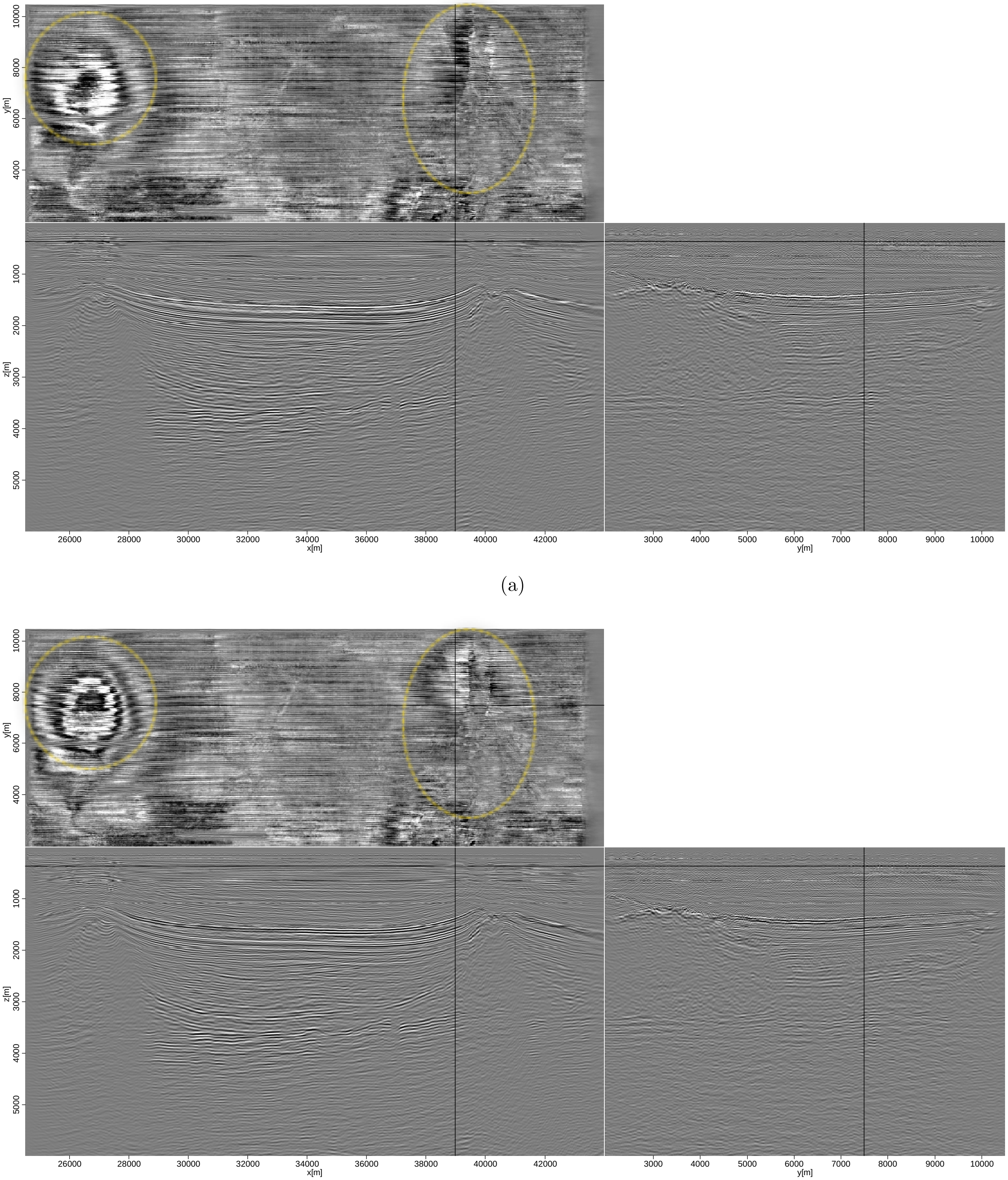

(a)

(b)

Figure 5.39: 3D view of the migrated images at shallow depth: (a) The migrated image at zero subsurface offset using the initial velocity model and the initial Q model. (b) The migrated image at zero subsurface offset using the updated velocity model and the initial Q model. I highlight two regions by two yellow circles in the depth slice. [**CR**]

chap5/ dlp3D-bqiv-pre-basc-bimg-before-ann dlp3D-bqiv-pre-basc-bimg-mid-ann

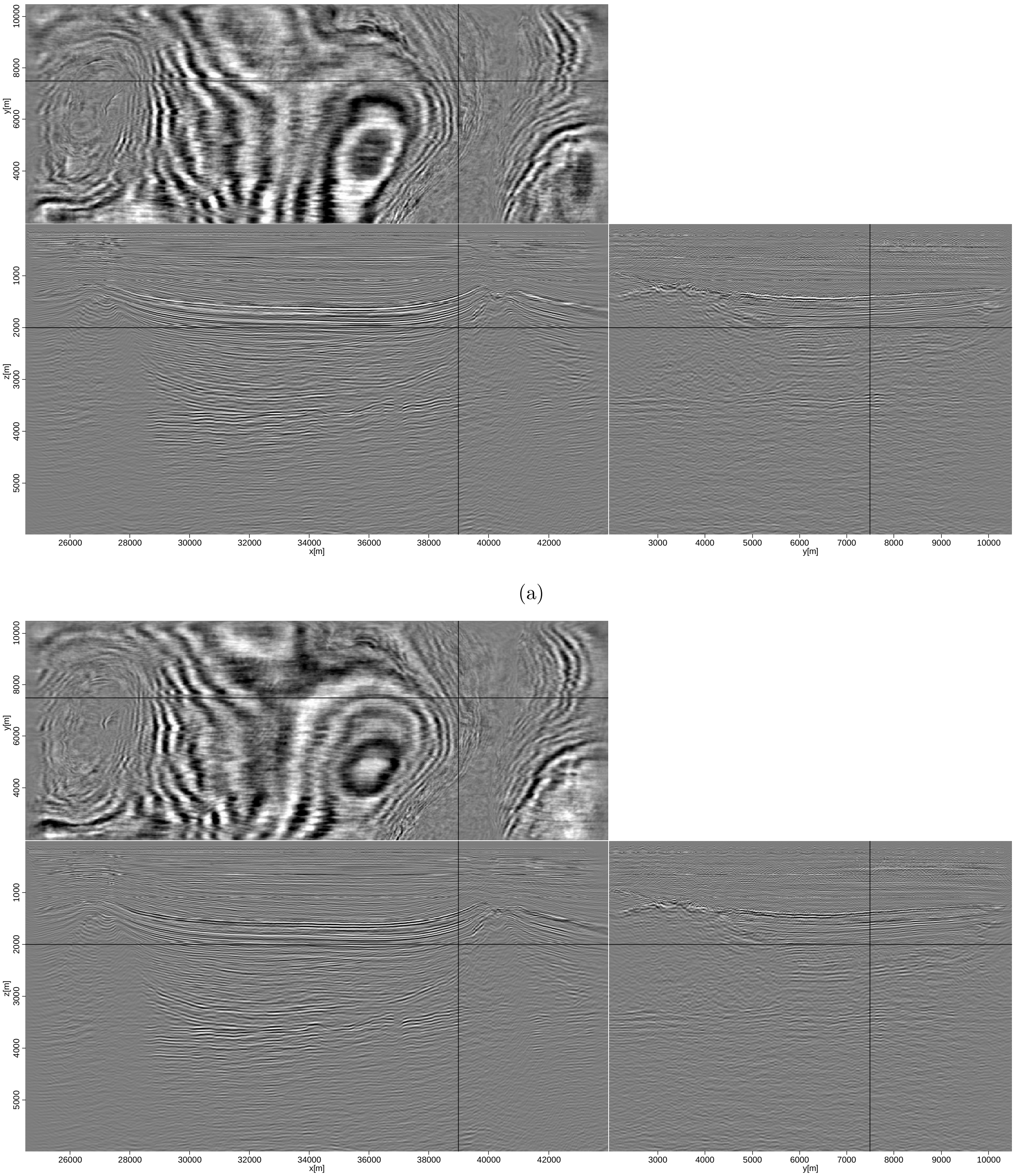

(a)

(b)

Figure 5.40: 3D view of the migrated images at deep depth:(a) The migrated image at zero subsurface offset using the initial velocity model and the initial Q model. (b) The migrated image at zero subsurface offset using the updated velocity model and the initial Q model. I highlight two regions by two yellow circles in the depth slice. [**CR**]

chap5/. dlp3D-bqiv-pre-basc-bimg-before-deep,dlp3D-bqiv-pre-basc-bimg-mid-deep

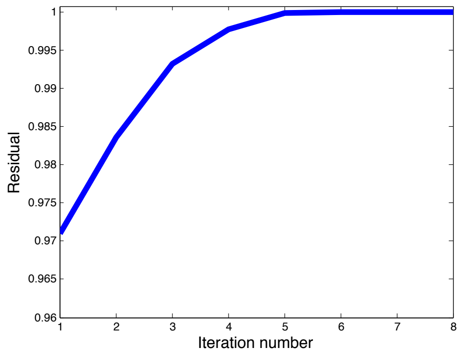

Figure 5.41: Normalized curve for the stacking power objective function. [**NR**] chap5/. dlp3D-one-fobj-V

## 3D one-way prestack WEMQA application

The initial Q model for the 3D WEMQA inversion is chosen in the same way as in the 2D workflow: homogeneous with a value of 500. To perform prestack WEMQA, I select the ADCIG with the midpoint at x=33,880 m as the reference gather, which is considered to be the least attenuated by two Q anomalies. Each ADCIG is compared with the reference ADCIG at the same crossline to compute $\rho$. The window size to compute spectra of subsets of the migrated image is 500 m in the Z direction, 125 m in the X direction and 75 m in the Y direction. The other parameters are the same as the ones used in the 2D one-way prestack WEMQA application.

Figure 5.43 is the inverted Q model displayed on a logarithmic scale ($\log_{10} Q$) after 10 iterations of the Q inversion. The inverted Q model matches the location of those recovered in Figure 5.37(b), which are in the same location as Dolphin's interpretation. Also, the attenuation of the gas is stronger than that of the channel. The objective function evaluated at iterates (Figure 5.44) of the one-way prestack WEMQA shows that the inversion converges within 9 iterations. The residual does not drop much, because the images are mainly updated near the Q anomalies regions, as shown in Figure 5.47.

When we compare the zero subsurface offset sections of the image migrated using the updated velocity model and initial Q model (shown in Figure 5.45(a) and 5.46(a)) with image migrated using updated models for both Q and velocity (shown in Figure 5.45(b) and Figure 5.46(b)), we see that using both updated models makes

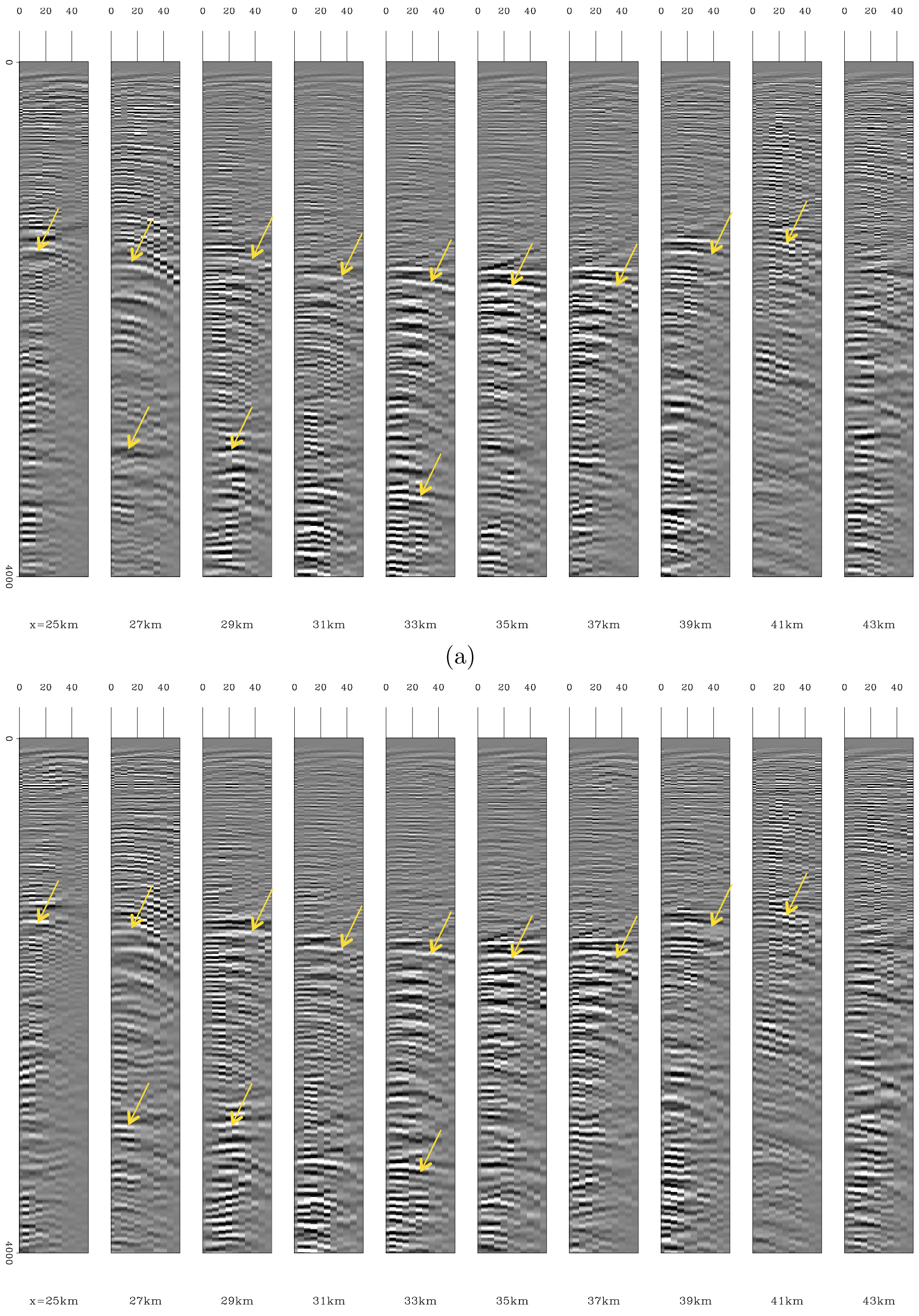

(a)

(b)

Figure 5.42: ADCIGs at the crossline=7,500 m: (a) the ADCIGs using the initial velocity model and the initial Q model. (b) The ADCIGs using the updated velocity model and the initial Q model. The vertical axis is depth in meters. The events pointed to by yellow arrows become flatter. **[CR]** chap5/. dlp3D-bqiv-pre-basc-bang-before-ann,dlp3D-bqiv-pre-basc-bang-mid-ann

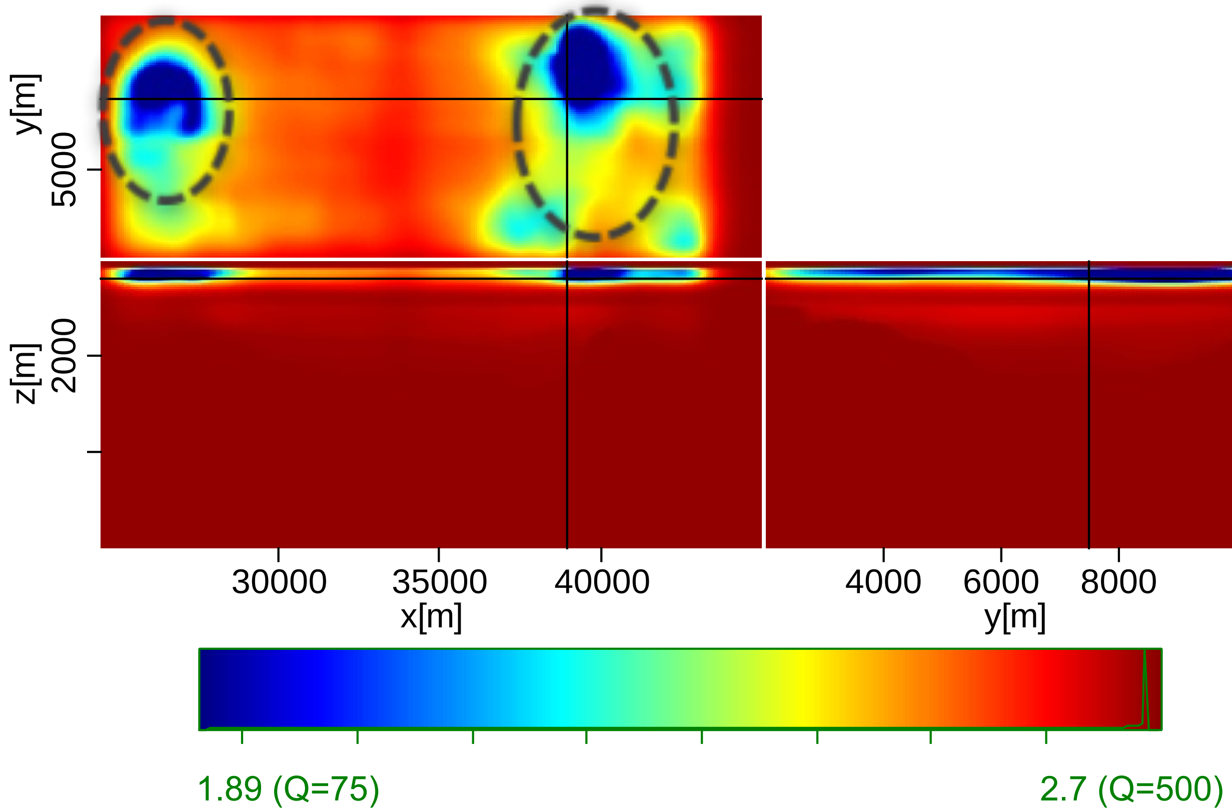

Figure 5.43: The inverted Q model displayed in logarithm scales ($\log_{10} Q$) after 10 iterations using one-way prestack WEMQA. [**CR**] chap5/. dlp3D-iqtv-pre-basc-bq-iter10-shallow

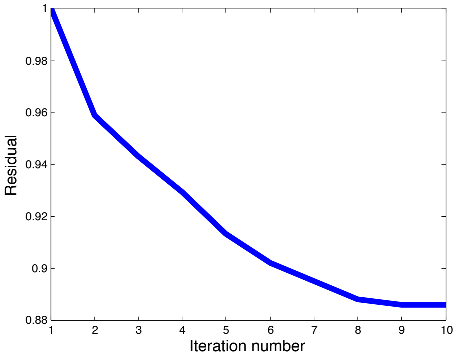

Figure 5.44: Normalized curve for the objective function of the one-way prestack WEMQA. The curve is normalized by the value of the objective function at the first iteration. [**NR**] chap5/. dlp3D-one-fobj-Q

the structures below the interpreted gas and channel regions brighter. However, the improvements are difficult to see. Therefore, I zoom in on the regions to the left and right of the salt domes at crossline = 7,500 m, and show them in Figure 5.48 and Figure 5.49, respectively. We recognize the same behavior observed in the 2D WEMQA application. Because more high frequency information is recovered in the compensated image, events appear sharper. Also the compensated events become more coherent because the attenuation-induced phase distortion is corrected. The image around the left salt dome improves more than around the right salt dome, because the inverted Q model has more attenuation around the left gas anomaly than around the right channel. The spectra of events below the right Q anomaly, seen in Figure 5.50, show that compensation with the inverted Q model whitens the spectra and compensates for the higher frequency loss caused by attenuation. Figure 5.51 shows 10 representative ADCIGs from the image migrated using the Q model before and after Q updating. The ADCIGs compensated by the inverted Q model have sharper, more coherent events. However, the improvements are not significant in ADCIGs with midpoints closer to the right channel because this area was updated less during Q inversion.

## DISCUSSION

The Dolphin multi-client field data acquired in the North Sea have attenuation and velocity problems due to shallow subsurface gas chimneys and channels which are correlated with strong attenuation and low-interval velocity. This study detects and corrects for those anomalies. The 2D and 3D results are consistent with Dolphin's interpretation. The updated velocity shows regions around the gas and channel features. The inverted Q model detects the shape and location of the gas and channel areas. The inversion results show that prestack WEMQA builds a higher resolution Q model than stacked WEMQA. Two-way WEMQA produces a slightly cleaner image, consequently, it achieves faster convergence than one-way WEMQA. These observations match the theory described in Chapter 2.

Although the improvement is small, using the inverted Q models in seismic migrations makes seismic events below the anomalies clearly visible, with improved frequency content and phase coherency. The angle gathers migrated using the updated velocity model and the inverted Q model are flatter, and higher resolution.

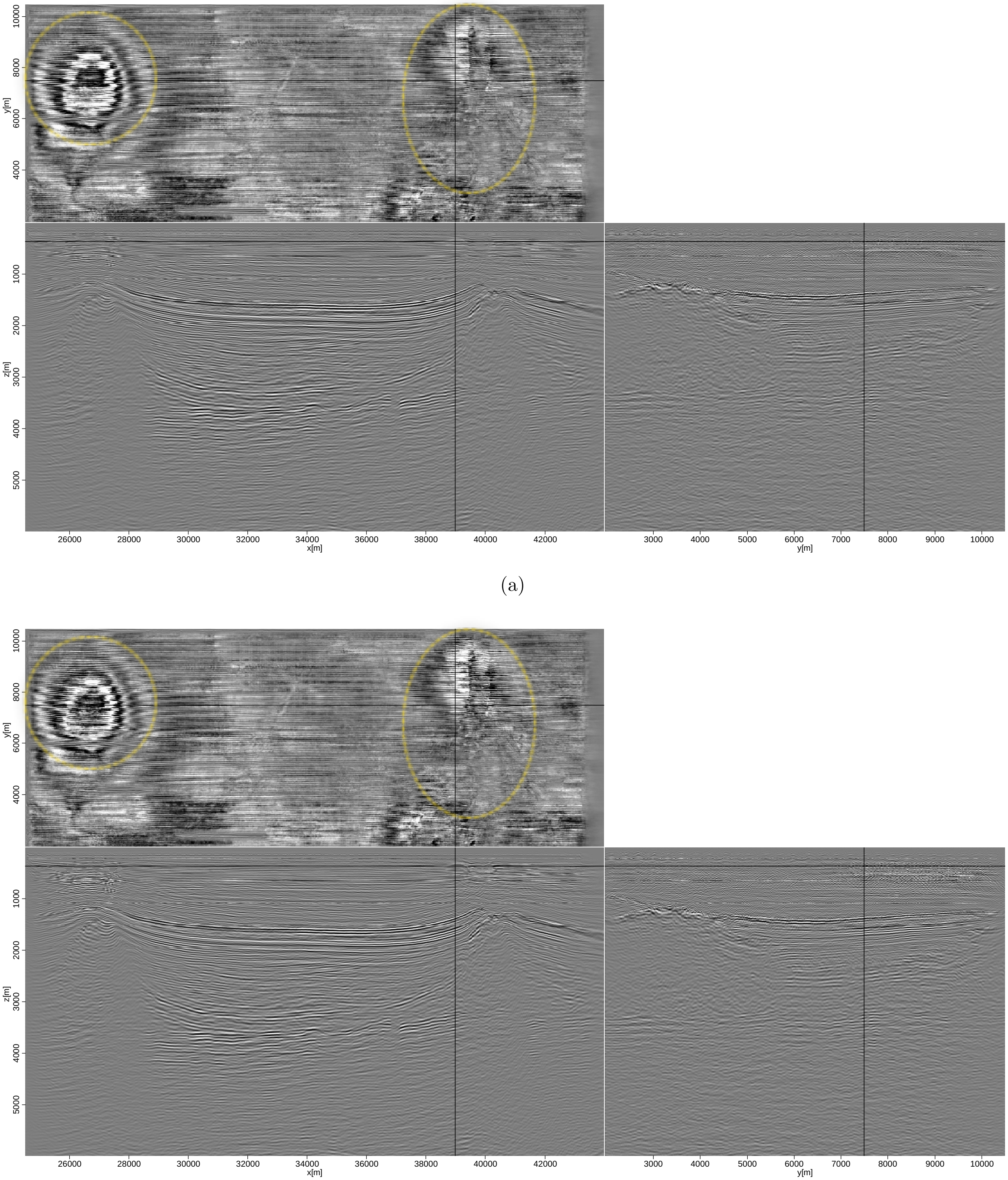

(a)

(b)

Figure 5.45: 3D views of the migrated images at shallow depth: (a) The migrated image at zero subsurface offset using the updated velocity model and the initial Q model. Same as Figure 5.39(b). Replicate the figure here for a convenient comparison with Figure 5.45(b). (b) The migrated image at zero subsurface offset using the updated velocity model and the updated Q model. [**CR**]

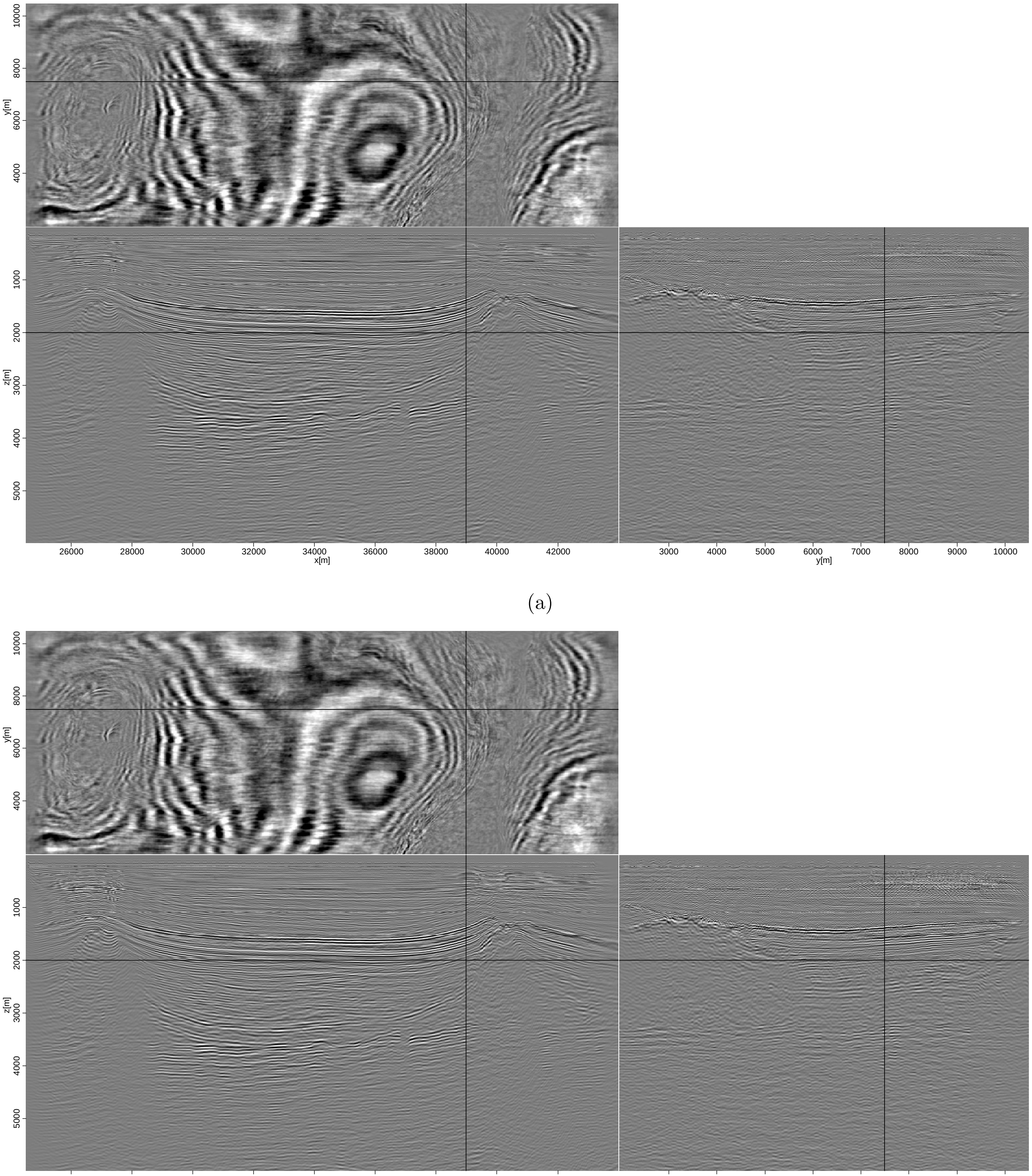

(a)

(b)

Figure 5.46: 3D views of the migrated images at deep depth: (a) The migrated image at zero subsurface offset using the updated velocity model and the initial Q model. Same as Figure 5.39(b). Replicate the figure here for a convenient comparison with Figure 5.46(b). (b) The migrated image at zero subsurface offset using the updated velocity model and the updated Q model. [**CR**] chap5/. dlp3D-bqiv-pre-basc-bimg-mid2-deep,dlp3D-bqiv-pre-basc-bimg-after-deep

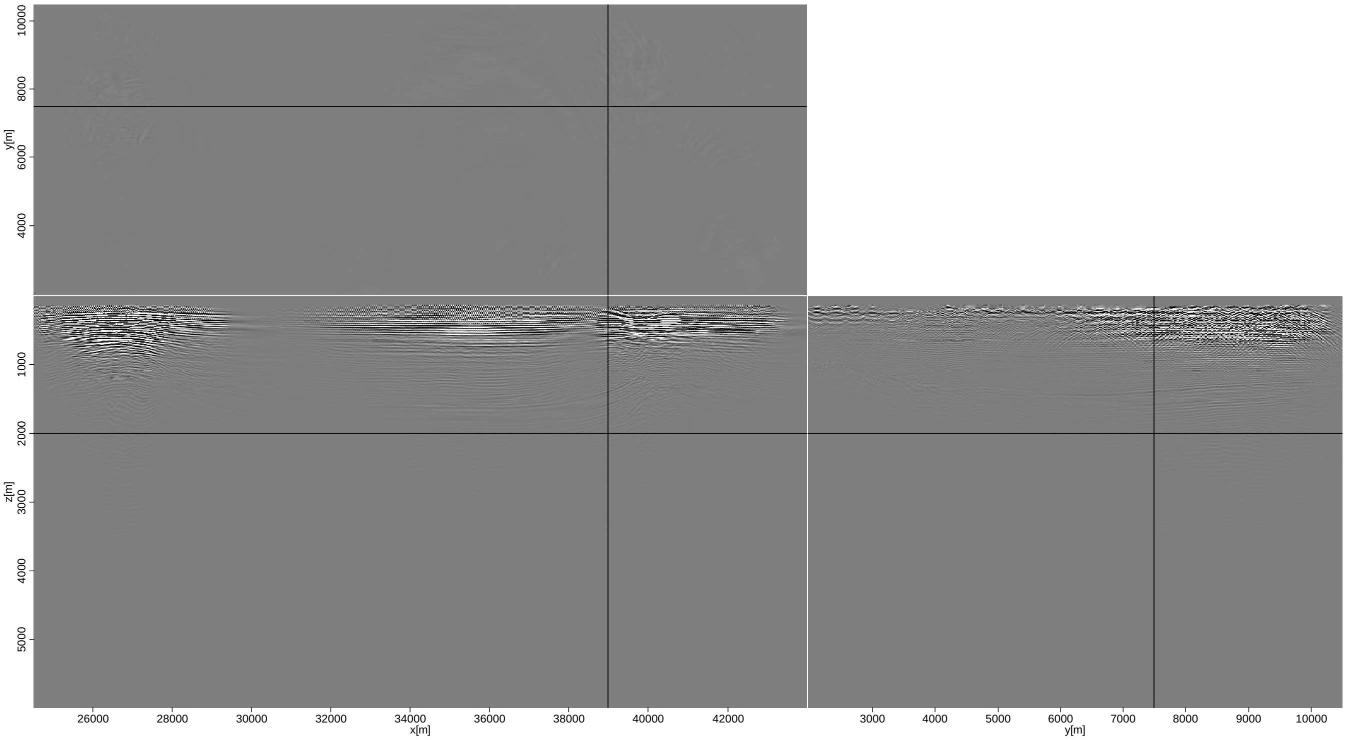

Figure 5.47: The image difference between Figure 5.45(b) and Figure 5.45(a). [**CR**]
chap5/. dlp3D-bqiv-pre-basc-bimg-resd

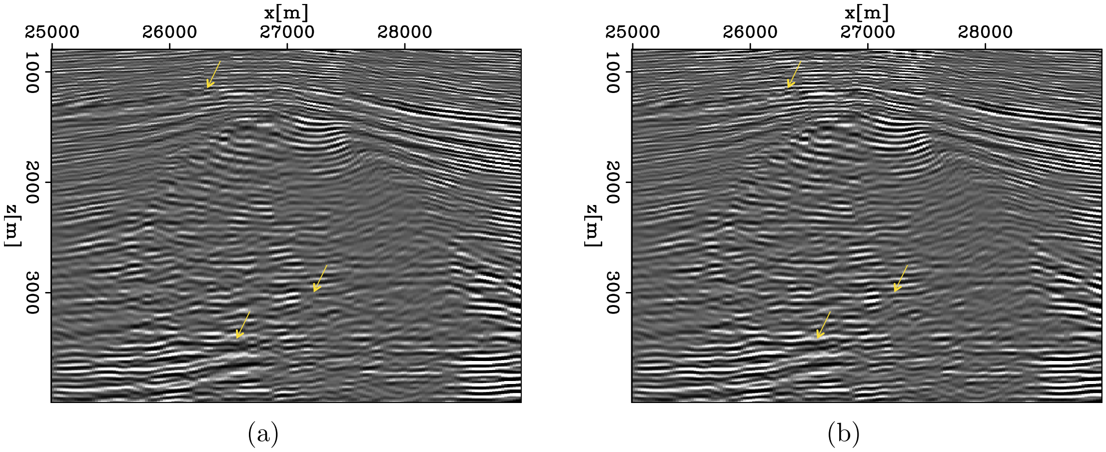

(a)

(b)

Figure 5.48: Zoomed-in region around the left side of the salt dome of (a) the attenuated image and (b) the compensated image. The amplitudes are gained at the deeper depth using $z^3$. The events pointed to by yellow arrows become sharper and more coherent. [**CR**]
chap5/. dlp3D-bqiv-pre-basc-reg1-before-7500-nagc-ann,dlp3D-bqiv-pre-basc-reg1-after-7500-nagc-ann

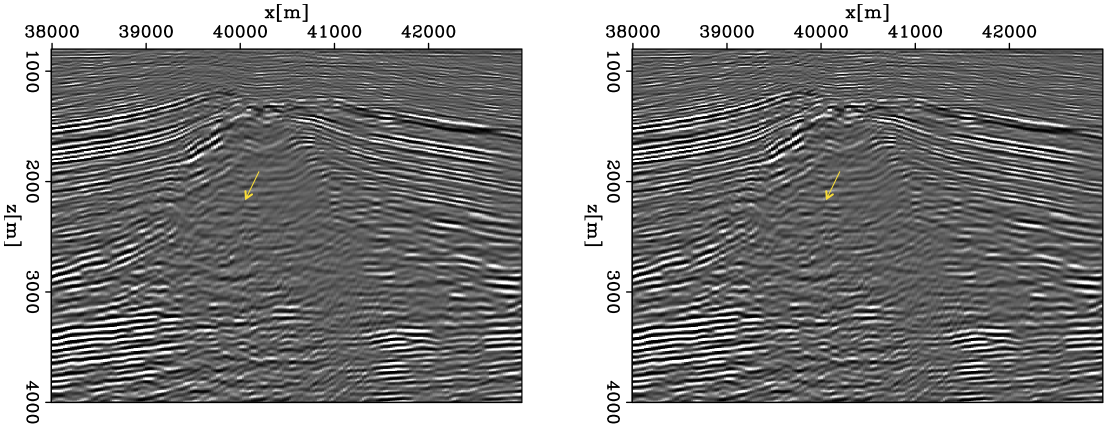

(a)

(b)

Figure 5.49: Zoomed-in region around the right side of the salt dome of (a) the attenuated image and (b) the compensated image. The amplitudes are gained at the deeper depth using $z^3$. The events pointed to by yellow arrows become sharper and more coherent. [**CR**] chap5/. dlp3D-bqiv-pre-basc-reg2-before-7500-nagc-ann,dlp3D-bqiv-pre-basc-reg2-after-7500-nagc-an

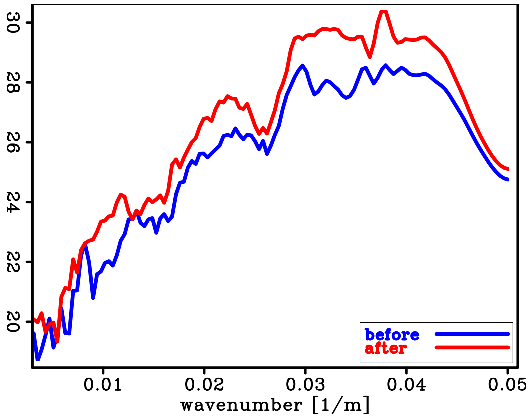

Figure 5.50: The spectra of the events below the right Q anomaly before Q compensation in blue and after Q compensation in red. The spectra are displayed in the logarithm scale. [**CR**] chap5/. dlp3D-bqiv-spex

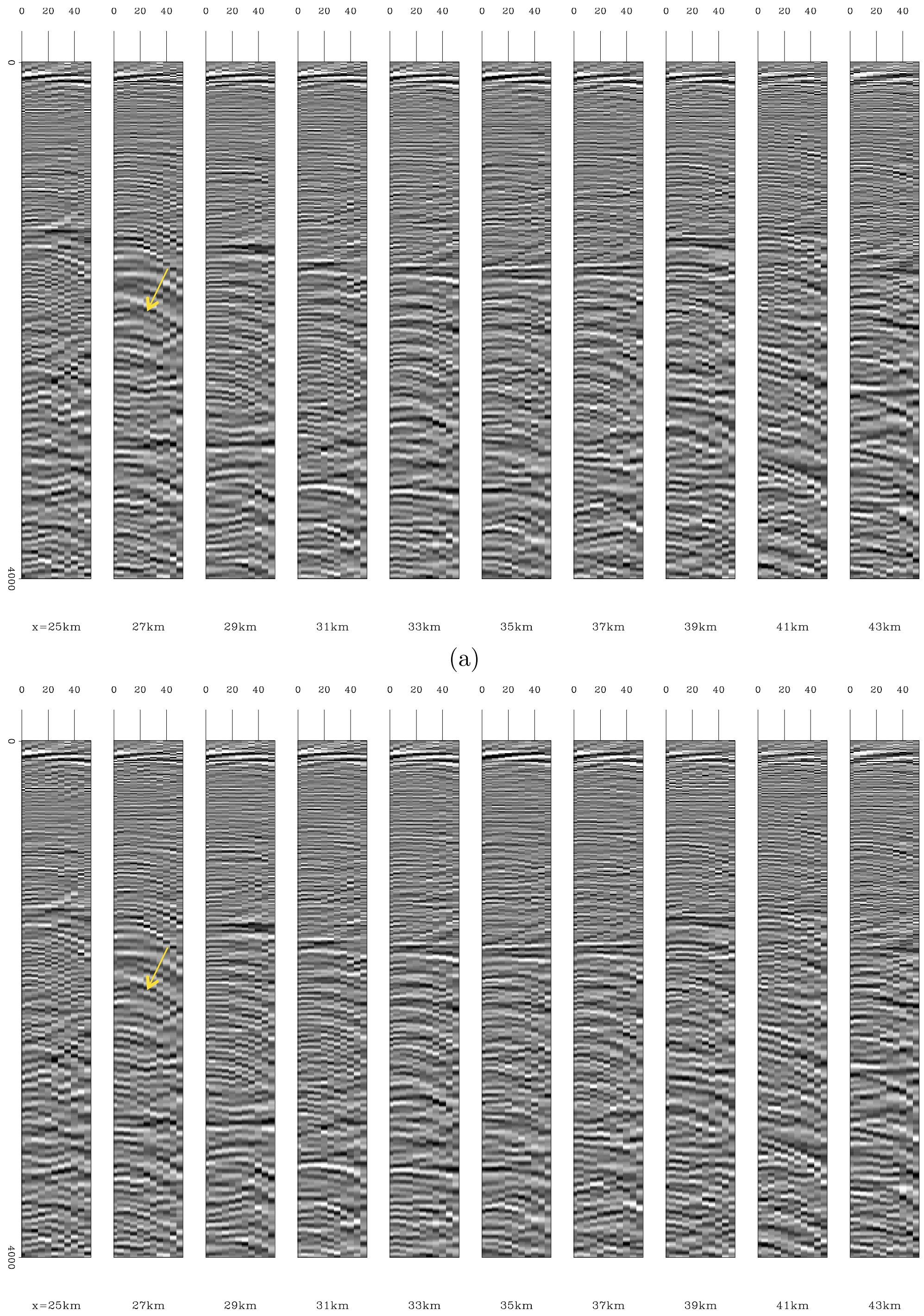

(a)

(b)

Figure 5.51: (a) The ADCIGs using the updated velocity model and the initial Q model. AGC is applied. (b) The ADCIGs using the updated velocity model and the inverted Q model. AGC is applied. The vertical axis is depth in meters. The events pointed by yellow arrows have higher resolution. [**CR**] chap5/. dlp3D-bqiv-pre-basc-bang-mid2-ann,dlp3D-bqiv-pre-basc-bang-after-ann

These improvements in image quality provide greater confidence for hydrocarbon exploration.

There are limitations to this method. In this application, the events in ADCIGs after velocity updating are not perfectly flattened. One possible reason is that stack power maximization is prone to cycle-skipping. That risk still exists, although I assume the initial velocity is close to the true one. The inaccuracy in the velocity model also reduces the reliability of the inverted Q model.

## ACKNOWLEDGMENTS

I would like to thank Dolphin Geophysical for providing these SHarp seismic data (CNS seismic data).

# Chapter 6

# Conclusions

I present an inversion-based method to build Q models that satisfies seismic data and rock physics constraints. In order to achieve this goal, I developed three key novel algorithms for Q model building.

First, I developed a new method, wave-equation migration Q analysis (WEMQA), to estimate Q models from migrated images by a wave-equation tomographic operator. I introduced an objective function that requires computing a migrated image with Q compensation. I also derived the gradient of the objective. I developed both the Q migration and the Q tomographic operator using frequency-domain and time-domain visco-acoustic wave equations. Its numerical synthetic examples show that it works well for models with gentle horizontal variation in the geological structure and for Q anomalies with simple shapes.

Second, I derived an approximate closed-form solution relating the compressional velocity to compressional quality factor using rock physics modeling. This solution is validated using well data in which the elastic properties were measured and Q was derived numerically. I applied this new relation between compressional velocity and compressional Q to both synthetic and field seismic data, which produced an improved Q estimated model. I showed that this improved Q model leads to a better seismic migration image.

Third, I developed a multi-parameter inversion of velocity and Q models using wave-equation migration analysis. This method poses the estimation problem as an optimization problem that seeks optimum velocity and Q models by minimizing user-defined image residuals. The numerical tests on a modified SEAM model with two gas clouds demonstrate the benefit of using such multi-parameter inversion, when the existing velocity and Q models are inaccurate. The results show that this inversion method is able to retrieve both velocity and Q models, and to correct and compensate the distorted migrated image caused by inaccurate velocity and Q models.

Finally, I applied this joint inversion of velocity and Q models to the 3D Dolphin's multi-client field data acquired in the North Sea, which has attenuation and velocity problems. Gas chimneys and channels exist in the subsurface with strong attenuation and low-interval velocity. The updated velocity shows low velocity zone in the gas and the channel area. The inverted Q model represents the shape and the location of the gas and the channel regions, which matches Dolphin's interpretation. Consequently, the migration with the updated velocity model and the estimated Q anomalies flattens the events in the subsurface angle gathers, enhances the damped amplitudes and the frequency content of the migrated events, corrects the distorted phase of the migrated events and makes them more coherent.

# Appendix A

# Spectral ratio method for migrated events

Tonn (1991) developed a spectral ratio method to measure the effect of Q on the recorded seismic data. This method assumes Q is constant over frequency. Letting the amplitude spectrum of an incident wave be $S(f)$, and the response of the attenuating medium be $GH(f)$, the amplitude spectrum of the outgoing wave $R(f)$ can be approximated as

$$R(f) = GH(f)S(f), \tag{A.1}$$

where the factor $G$ includes geometrical spreading, instrument response, source/receiver coupling, radiation pattern, and reflection/transmission coefficients, and $H(f)$ describes the attenuation effect on the amplitude. Constant Q model assumes that attenuation is linearly proportional to frequency, that is, the response $H(f)$ can be expressed as

$$H(f) = \exp\left(-f \int_{\text{ray}} \frac{\pi}{Q_1 v_{\text{int}}} dl\right), \tag{A.2}$$

where the integral is taken along the raypath, $v_{\text{int}}$ is the interval velocity and $Q_1$ is the interval Q model of the attenuating medium.

Assuming that the outgoing wave travels through an attenuation medium of $G_1H_1(f)$ with its quality factor being $Q_1$, and thus with its spectrum $R_1(f) = G_1H_1(f)S(f)$; while another wave generated from the same source propagates in a different path without attenuation with a response of $R_2(f) = G_2H_2(f)S(f)$, where $H_2(f) = 1$ because $1/Q = 0$. This non-attenuated spectrum is also referred as a reference spectrum, which can be derived from source signature, waver reflection or a non-attenuating trace of the data in a practical case. A ratio between $R_1(f)$ and $R_2(f)$ removes the frequency-dependent common factor $S(f)$, and preserves the attenuation response $H_1(f)$, as shown by the following equation,

$$\ln[R_1(f)/R_2(f)] = \rho f + \ln[G_1/G_2], \tag{A.3}$$

where

$$\rho = \left( - \int_{\text{ray}} \frac{\pi}{Q_1 v_{\text{int}}} dl \right), \tag{A.4}$$

Note that the absolute scaling of these two waveform comes out in the intercept term in Equation A.3. Therefore, this method automatically removes the effect of the frequency-independent factor, such as geometrical spreading, instrument response, source/receiver coupling, radiation pattern, and reflection/transmission coefficients. In addition, Equation A.3 shows that the logarithmic ratio of $R_1(f)$ and $R_2(f)$ is linearly related to their frequency $f$, and that their linear relation is represented by a slope value $\rho$. This parameter $\rho$ integrates Q along the ray path as shown in Equation A.4 and hence indicates the intensity of attenuation in the medium. Theoretically, a strong attenuation results into a large negative value of $\rho$; while a non-attenuating medium gives $\rho = 0$. Therefore, the parameter $\rho$ is a representative of the amplitudes loss of a wave caused by attenuation on its spectra, and hence is able to effectively indicates the intensity of the attenuation in the medium.

To extend this method to measuring the effect of Q on the migrated images, I consider two migrated images: one image, $I_1$, is migrated with Q compensation model, $Q_1$; the other image, $I_2$, is migrated using the same recorded data and same compensation methods but with a different Q model, $Q_2$. The model $Q_2$ equals the Q model of the actual attenuating media, but does not equal $Q_1$. The recorded data are attenuated with its atenuation response being

$$H(f) = \exp \left( -f \int_{\text{ray}} \frac{\pi}{Q_2 v_{\text{int}}} dl \right). \tag{A.5}$$

I define $\mathbf{k}$ as the local wavenumber of a migrated event, and $|\mathbf{k}| = 2\pi f / v_{\text{int}}$. At the same image location, I define the spectrum of a migrated event in $I_1$ as $R_1(')$ and the spectrum of a migrated event in the image of $I_2$ as the reference spectra $R_2(\mathbf{k})$. $R_1(\mathbf{k})$

includes a term $H_1(\mathbf{k})$ that represents the attenuation effect on the image amplitude, where

$$H_1(k) = \exp\left(-\int_{\text{ray}} \frac{|\mathbf{k}|}{2}(\frac{1}{Q_2} - \frac{1}{Q_1})dl\right). \tag{A.6}$$

Because the attenuation effects in the image $I_2$ has been fully corrected by the correct $Q_2$ model, its attenuation effects $H_2(\mathbf{k}) = \mathbf{1}$. As illustrated in Chapter 2, I map the spectra from the $\mathbf{k}$ domain to $\mathbf{k}'$ by $|\mathbf{k}'| = |\mathbf{k}|v_{\text{int}}/v_{\text{ref}}$:

$$H_1(k') = \exp\left(-|\mathbf{k}'|\int_{\text{ray}} \frac{v_{\text{ref}}}{2v_{\text{int}}}dl(\frac{1}{Q_2} - \frac{1}{Q_1})\right). \tag{A.7}$$

Same as the spectral ratio method in the data domain (Tonn, 1991), the ratio between $R_1(k)$ and $R_2(k)$ removes the frequency-dependent common factor and preserves the attenuation effect term as follows:

$$\ln[R_1(\mathbf{k}')/R_2(\mathbf{k}')] = \rho|\mathbf{k}'| + G_0, \tag{A.8}$$

where $G_0 = \ln[G_1/G_2]$, and

$$\rho = \int \frac{v_{\text{ref}}}{2v_{\text{int}}}(\frac{1}{Q_1} - \frac{1}{Q_2})dl, \tag{A.9}$$

where the integral is taken along the wave-path.

# Appendix B

# Image perturbation

The objective function of WEMQA method is formulated in Equation 2.1, which is replicated as follows:

$$J = \frac{1}{2} \sum_{\mathbf{x}} \left| \rho \left( \mathbf{x}; Q \right) \right|^2 \tag{B.1}$$

where $\mathbf{x}$ is each a spatial location in the image space, and $Q$ is the current model for quality factor.

The gradients of the objective defined in Equation 2.1 is the first derivative of this objective function with respect to each point in the Q model. The resulting Q gradient is

$$\left( \frac{\partial J}{\partial Q} \right)^* = \sum_{\mathbf{x}} \left( \frac{\partial \rho}{\partial Q} \right)^* \rho = \sum_{\mathbf{x}} \left( \frac{\partial \rho}{\partial I} \frac{\partial I}{\partial Q} \right)^* \rho = \sum_{\mathbf{x}} \left( \frac{\partial I}{\partial Q} \right)^* \left( \frac{\partial \rho}{\partial I} \right)^* \rho, \tag{B.2}$$

where $^*$ means adjoint, and both $I$ and $\rho$ are the function of the current Q model. Equation B.2 has a clear physical interpretation and mathematically explains that two terms are required to to derive the Q gradient. The term $\left(\frac{\partial \rho}{\partial I}\right)^* \rho$ is known as the image perturbation ($\Delta I$), and reflects the difference between the target image and the reference image. Such differences are only caused by attenuation. The term $\left(\frac{\partial I}{\partial Q}\right)$, known as the wave-equation tomographic operator, and its adjoint $\left(\frac{\partial I}{\partial Q}\right)^*$ back projects the image perturbation to a perturbation in the interval Q model. In this appendix, I will focus on deriving the image perturbation ($\Delta I$).

The parameter $\rho$ is computed from the spectra of windowed migrated events. I define `F` as the windowed Fourier transform operator that extracts the migrated events from seismic image $I$ using individual windows and transforms the events from depth domain to $F(\mathbf{k})$ in the local wavenumber domain $\mathbf{k}$. Note that windowed Fourier transform is a linear operator. I express $F(\mathbf{k})$ in polar form:

$$\mathtt{F}I(\mathbf{x},\mathbf{x}';Q) = F(\mathbf{k},\mathbf{x}';Q) = |F(\mathbf{k},\mathbf{x}';Q)|\exp(i\Phi(\mathbf{k},\mathbf{x}';Q)), \tag{B.3}$$

where $\mathbf{x}'$ is the spatial location of the window center and $\mathbf{x}$ is the spatial location in the windowed region. I use the notation $R_1(\mathbf{k},\mathbf{x}';Q)$ to represent $|F(\mathbf{k},\mathbf{x}';Q)|$ that is the spectra of $F(\mathbf{k},\mathbf{x}';Q)$, and I use the notation $p_1(\mathbf{k},\mathbf{x}';Q)$ to represent $\exp(i\Phi(\mathbf{k},\mathbf{x}';Q))$ where $\Phi(\mathbf{k},\mathbf{x}';Q)$ is the phase angle. In this following, I will use $(\mathbf{k})$ to represent $(\mathbf{k},\mathbf{x}';Q)$. Because $p_1(\mathbf{k})\,p_1(\mathbf{k})^* = \exp(i\Phi(\mathbf{k}))\exp(-i\Phi(\mathbf{k})) = 1$, the spectrum $R_1(\mathbf{k})$ becomes

$$R_1(\mathbf{k}) = p_1(\mathbf{k},x';Q)^*\,\mathtt{F}I(\mathbf{x},\mathbf{x}';Q). \tag{B.4}$$

Parameter $\rho$ formulated in Equation 2.15 can be rewritten as follows:

$$\rho = \frac{\ln(R_1(\mathbf{k}')/R_2(\mathbf{k}')) - G_0}{|\mathbf{k}'|} = \frac{\ln(R_1(\mathbf{k}')) - \ln(R_2(\mathbf{k}')) - G_0}{|\mathbf{k}'|}. \tag{B.5}$$

where $\mathbf{k}'$ is the reference wavenumber defined in Chapter 2. I define a operator $\mathtt{Z}$ to map the spectra $R_1(\mathbf{k})$ in the $\mathbf{k_z}$ domain to the spectra $R_1(\mathbf{k}')$ in the reference wavenumber $\mathbf{k}'$ domain using Equation 2.13. $R_1(\mathbf{k}')$ is the spectrum of the migrated events without a correct Q compensation, and $R_2(\mathbf{k}')$ is the spectrum of the migrated events with a correct Q compensation. The term $G_0$ is constant and independent of Q. Therefore, the derivative of $\rho$ (Equation B.5) with respect to Q removes the term of $\ln R_2(\mathbf{k}')$ and $G_0$ as follows:

$$\left(\frac{\partial\rho}{\partial Q}\right)^* = \left(\frac{1}{|\mathbf{k}'|}\frac{\partial(\ln(R_1(\mathbf{k}')))}{\partial Q}\right)^* = \left(\frac{1}{|\mathbf{k}'|}\frac{1}{R_1(\mathbf{k}')}\frac{\partial(R_1(\mathbf{k}'))}{\partial Q}\right)^*. \tag{B.6}$$

Substituting Equation B.4 into Equation B.6 and based on the chain rule, Equation B.6 becomes

$$
\begin{aligned}
\left(\frac{\partial \rho}{\partial Q}\right)^{*} &= \left(\frac{1}{|\mathbf{k}'|}\frac{1}{R_1(\mathbf{k}')}\frac{\partial\left(R_1(\mathbf{k}')\right)}{\partial\left(R_1(\mathbf{k})\right)}\frac{\partial\left(R_1(\mathbf{k})\right)}{\partial Q}\right)^{*} \\
&= \left(\frac{1}{|\mathbf{k}'|}\frac{1}{R_1(\mathbf{k}')}\mathtt{Z}\frac{p_1(\mathbf{k})^{*}\,\mathtt{F}\partial I}{\partial Q}\right)^{*} \\
&= \left(\frac{\partial I}{\partial Q}\right)^{*}\mathtt{F}^{*}\left(p_1(\mathbf{k})\,\mathtt{Z}^{*}\frac{1}{R_1(\mathbf{k}')}\frac{1}{|\mathbf{k}'|}\right) \qquad .
\end{aligned}
\tag{B.7}
$$

where the Q effects on the phase of the migrated events are assumed to be negligible. Therefore, the Q gradient in Equation B.2 can be derived as follows,

$$
\begin{aligned}
\left(\frac{\partial J}{\partial Q}\right)^{*} &= \sum_{\mathbf{x}}\left(\frac{\partial \rho}{\partial Q}\right)^{*}\rho \\
&= \sum_{\mathbf{x}}\left(\frac{\partial I}{\partial Q}\right)^{*}\mathtt{F}^{*}\left(p_1(\mathbf{k})\,\mathtt{Z}^{*}\frac{1}{R_1(\mathbf{k}')}\frac{1}{|\mathbf{k}'|}\right)\rho,
\end{aligned}
\tag{B.8}
$$

and the image perturbation becomes as follows, which is same as the one in Equation 2.17:

$$
\Delta \mathrm{I} = \mathtt{F}^{*}\left(p_1(\mathbf{k})\,\mathtt{Z}^{*}\frac{1}{R_1(\mathbf{k}')}\frac{1}{|\mathbf{k}'|}\right)\rho. \tag{B.9}
$$

# Appendix C

# Wave-equation Q tomographic operator

To derive the tomographic projector, I start with the image condition as following:

$$I(\mathbf{x},\mathbf{h}) = \sum_{\omega,\mathbf{x}_s,\mathbf{x}_r} G^*(\mathbf{x}-\mathbf{h},\mathbf{x}_s,\omega)G^*(\mathbf{x}+\mathbf{h},\mathbf{x}_r,\omega)d(\mathbf{x}_r,\mathbf{x}_s,\omega), \tag{C.1}$$

where $G$ is the Green's function, the impulse response of the wave equation; $\mathbf{x}$ is the Green's functions' coordinate $d$ is the surface recorded data; $\mathbf{x}_s$, $\mathbf{x}_r$ are the source and receiver coordinates; $I$ is the image; $\mathbf{h}$ is the subsurface offset and $\omega$ is frequency.

The derivative of the image with respect to the Q model can be derived as the sum of the attenuation-induced perturbed source wavefield multiplied by the background receiver wavefield and the attenuation-induced perturbed receiver wavefield multiplied by the background source wavefield:

$$\begin{aligned}\frac{\partial I\left(\mathbf{x},\mathbf{h}\right)}{\partial Q\left(\mathbf{y}\right)}|_{Q_0} &= \sum_{\omega,\mathbf{x_s},\mathbf{x_r}} \left(\frac{\partial G\left(\mathbf{x}-\mathbf{h},\mathbf{x_s},\omega;Q_0\right)}{\Delta Q\left(\mathbf{y}\right)}\right)^* G^*\left(\mathbf{x}+\mathbf{h},\mathbf{x_r},\omega;Q_0\right) d\left(\mathbf{x_r},\mathbf{x_s},\omega\right) \\ &+ \sum_{\omega,\mathbf{x_s},\mathbf{x_r}} G^*\left(\mathbf{x}-\mathbf{h},\mathbf{x_s},\omega;Q_0\right)\left(\frac{\partial G\left(\mathbf{x}+\mathbf{h},\mathbf{x_r},\omega;Q_0\right)}{\Delta Q\left(\mathbf{y}\right)}\right)^* d\left(\mathbf{x_r},\mathbf{x_s},\omega\right),\end{aligned} \tag{C.2}$$

where $\mathbf{x}$ is the Green's functions' spatial coordinate, $\mathbf{y}$ is the Q model's spatial coordinates.

**One-way Green's function and its derivative with respect to a Q model.** The Green's function of the one-way visco-acoustic wave equation is expressed as follows:

$$\begin{cases} \left(\frac{\partial}{\partial z} + ik_z\right) G(\mathbf{x}, \mathbf{x}_s, \omega) = 0 \\ G(x, y, z = 0, \mathbf{x}_s, \omega) = \delta(\mathbf{x} - \mathbf{x}_s) \end{cases}, \tag{C.3}$$

and

$$\begin{cases} \left(\frac{\partial}{\partial z} - ik_z\right) G(\mathbf{x}, \mathbf{x}_r, \omega) = 0 \\ G(x, y, z = 0, \mathbf{x}_r, \omega) = \delta(\mathbf{x} - \mathbf{x}_r) \end{cases}, \tag{C.4}$$

where $G(\mathbf{x}, \mathbf{x}_s, \omega)$ is the source side Green's function at the image point $\mathbf{x}$ with the source located at $\mathbf{x}_s$; $G(\mathbf{x}, \mathbf{x}_r, \omega)$ is the receiver side Green's function at the image point $\mathbf{x}$ with the data recorded at $\mathbf{x}_r$; and $k_z$ is the vertical wavenumber in Equation 2.4.

If I perturb the Q model as $Q = Q_0 + \Delta Q$, the Green function in Equation C.3 becomes as follows,

$$\left(\frac{\partial}{\partial z} + ik_z + \Delta Q \frac{\partial ik_z}{\partial Q} |_{Q_0}\right) \left(G\left(\mathbf{x}, \mathbf{x_s}, \omega; Q_0\right) + \Delta G\left(\mathbf{x}, \mathbf{x_s}, \omega\right)\right) = 0. \tag{C.5}$$

Subtracting Equation C.3 from Equation C.5 and applying Born's approximation give the following equation,

$$\left(\frac{\partial}{\partial z} + ik_z\right) \Delta G\left(\mathbf{x}, \mathbf{x_s}, \omega\right) + \Delta Q \frac{\partial ik_z}{\partial Q} |_{Q_0} G\left(\mathbf{x}, \mathbf{x_s}, \omega; Q_0\right) = 0, \tag{C.6}$$

which enables me to find the derivative of the Green's function with respect to Q as shown in the following:

$$\frac{\partial G\left(\mathbf{x}, \mathbf{x_s}, \omega; Q_0\right)}{\partial Q\left(\mathbf{y}\right)} = -\frac{i\partial k_z}{\partial Q} |_{Q_0} G\left(\mathbf{y}, \mathbf{x_s}, \omega; Q_0\right) G\left(\mathbf{x}, \mathbf{y}, \omega; Q_0\right). \tag{C.7}$$

I follow the same steps for the receiver side Green's function in Equation C.4 to obtain:

$$\frac{\partial G\left(\mathbf{x}, \mathbf{x_r}, \omega; Q_0\right)}{\partial Q\left(\mathbf{y}\right)} = \frac{i\partial k_z}{\partial Q} |_{Q_0} G\left(\mathbf{y}, \mathbf{x_r}, \omega; Q_0\right) G\left(\mathbf{x}, \mathbf{y}, \omega; Q_0\right) \tag{C.8}$$

To derive the derivative of $k_z$ with respect to $Q$, I apply chain rule to get

$$\frac{\partial k_z}{\partial Q} = \frac{\partial k_z}{\partial \tilde{s}} \frac{\partial \tilde{s}}{\partial Q}, \tag{C.9}$$

where the following equations are derived based on Equation 2.4 and Equation 2.2.

$$\begin{aligned} \frac{\partial k_z}{\partial \tilde{s}} &= \frac{\omega^2 \tilde{s}}{\sqrt{(\omega\tilde{s})^2 - |\mathbf{k}|^2}} = \frac{\omega}{\sqrt{1 - \frac{|\mathbf{k}|^2}{\omega^2 \tilde{s}^2}}} & , \\ \frac{\partial \tilde{s}}{\partial Q} &= s_{\omega r} \frac{1}{\pi Q^2} \ln(\omega/\omega_r) \left(1 + \frac{i}{2Q}\right) + s_{\omega r} \left(1 - \frac{1}{\pi Q} \ln(\omega/\omega_r)\right) \left(-\frac{i}{2Q^2}\right). \end{aligned} \tag{C.10}$$

Therefore, the derivative of $k_z$ with respect to $Q$ can be simplified as

$$\frac{\partial k_z}{\partial Q} = \frac{\omega}{\sqrt{1 - \frac{|\mathbf{k}|^2}{\omega^2 \tilde{s}^2}}} \frac{-s_{\omega r}}{Q^2} \left(\frac{i}{2} - \frac{i}{\pi Q} \ln(\omega/\omega_r) - \frac{1}{\pi} \ln(\omega/\omega_r)\right). \tag{C.11}$$

**Two-way Green's function and its derivative with respect to a Q model.**

The Green's function in the two-way visco acoustic wave equation is expressed as follows:

$$\begin{cases} \left(\eta \mathbf{L} + \tau \mathbf{H} \frac{d}{dt} - v^{-2} \frac{\partial^2}{\partial t^2}\right) G(\mathbf{x}, \mathbf{x}_s, \omega) = 0 \\ G(x, y, z = 0, \mathbf{x}_s, \omega) = \delta(\mathbf{x} - \mathbf{x}_s) \end{cases}, \tag{C.12}$$

and

$$\begin{cases} \left(\eta \mathbf{L} + \tau \mathbf{H} \frac{d}{dt} - v^{-2} \frac{\partial^2}{\partial t^2}\right) G(\mathbf{x}, \mathbf{x}_r, \omega) = 0 \\ G(x, y, z = 0, \mathbf{x}_r, \omega) = \delta(\mathbf{x} - \mathbf{x}_r) \end{cases}. \tag{C.13}$$

If I perturb the Q model as $Q = Q_0 + \Delta Q$, the Green function in Equation C.12 becomes as follows,

$$\left(\eta \mathbf{L} + \Delta Q \frac{\partial \eta \mathbf{L}}{\partial Q} |_{Q_0} + \tau \mathbf{H} \frac{d}{dt} + \Delta Q \frac{\partial \tau \mathbf{H}}{\partial Q} |_{Q_0} \frac{d}{dt} - v^{-2} \frac{\partial^2}{\partial t^2}\right) \left(G\left(\mathbf{x}, \mathbf{x_s}, \omega; Q_0\right) + \Delta G\left(\mathbf{x}, \mathbf{x_s}, \omega\right)\right) = 0. \tag{C.14}$$

Subtracting Equation C.12 from Equation C.14 and applying Born's approximation give the following equation

$$\left(\eta \mathbf{L} + \tau \mathbf{H} \frac{d}{dt} - v^{-2} \frac{\partial^2}{\partial t^2}\right) \Delta G\left(\mathbf{x}, \mathbf{x_s}\right) + \left(\Delta Q \frac{\partial \eta \mathbf{L}}{\partial Q} |_{Q_0} + \Delta Q \frac{\partial \tau \mathbf{H}}{\partial Q} |_{Q_0} \frac{d}{dt}\right) G\left(\mathbf{x}, \mathbf{x_s}; Q_0\right) = 0, \tag{C.15}$$

which enables me to find the derivative of the Green's function with respect to Q as shown in the following:

$$\frac{\partial G\left(\mathbf{x}, \mathbf{x_s}, \omega; Q_0\right)}{\partial Q\left(\mathbf{y}\right)} = -\left(\frac{\partial \eta \mathbf{L}}{\partial Q} |_{Q_0} + \frac{\partial \tau \mathbf{H}}{\partial Q} |_{Q_0} \frac{d}{dt}\right) G\left(\mathbf{y}, \mathbf{x_s}, \omega; Q_0\right) G\left(\mathbf{x}, \mathbf{y}, \omega; Q_0\right), \tag{C.16}$$

To simply Equation C.16, I define $\mathbf{A} = \frac{\partial \eta \mathbf{L}}{\partial Q} |_{Q_0}$ and $\mathbf{B} = \frac{\partial \tau \mathbf{H}}{\partial Q} |_{Q_0}$. I follow the same steps for the receiver side Green's function in Equation C.13 to obtain:

$$\frac{\partial G\left(\mathbf{x}, \mathbf{x_r}, \omega; Q_0\right)}{\partial Q\left(\mathbf{y}\right)} = -\mathbf{A} G\left(\mathbf{y}, \mathbf{x_r}, \omega; Q_0\right) G\left(\mathbf{x}, \mathbf{y}, \omega; Q_0\right) - \mathbf{B} \frac{d}{dt} G\left(\mathbf{y}, \mathbf{x_r}, \omega; Q_0\right) G\left(\mathbf{x}, \mathbf{y}, \omega; Q_0\right). \tag{C.17}$$

Zhu et al. (2014); Zhu and Harris (2014) derived that the fractional laplacian $\mathbf{H} = \left(-\nabla^2\right)^{\gamma+1/2}$, and $\mathbf{L} = \left(-\nabla^2\right)^{\gamma+1}$, where the variable $\gamma$ is defined as $\gamma = 1/\pi \tan^{-1}\left(1/Q\right)$. Zhu et al. (2014); Zhu and Harris (2014) also showed that the absorption and dispersion coefficients $\eta = -v^{2\gamma}\omega_r^{-2\gamma} \cos \pi\gamma$ and $\tau = -v^{2\gamma-1}\omega_r^{-2\gamma} \sin \pi\gamma$. Therefore, the derivation of $\mathbf{A}$ and $\mathbf{B}$ are shown as follows:

$$\begin{aligned} \mathbf{A} = \frac{\partial \eta \mathbf{L}}{\partial Q} = \frac{\partial \eta}{\partial Q} \mathbf{L} + \eta \frac{\partial \mathbf{L}}{\partial Q} &= -\frac{\left(2\eta \ln v - 2\eta \ln \omega_0 - \pi v \tau\right) \mathbf{L} + \eta \mathbf{L} \ln\left(-\nabla^2\right)}{\pi\left(Q^2+1\right)}, \\ \mathbf{B} = \frac{\partial \tau \mathbf{H}}{\partial Q} = \frac{\partial \tau}{\partial Q} \mathbf{H} + \tau \frac{\partial \mathbf{H}}{\partial Q} &= -\frac{\left(2\tau \ln v - 2\tau \ln \omega_0 + \pi v^{-1} \eta\right) \mathbf{H} + \tau \mathbf{H} \ln\left(-\nabla^2\right)}{\pi\left(Q^2+1\right)}. \end{aligned} \tag{C.18}$$

# Bibliography

Aki, K. and P. G. Richards, 1990, Quantitative seismology: Theory and methods.

Best, A. I., C. MaCann, and J. Sothcott, 1994, The relationships between the velocities, attenuations, and petrophysical properties of reservoir sedimentary rocks: Geophysical Prospecting, **42**, 151–178.

Billette, F. and S. Brandsberg-Dahl, 2005, The 2004 BP velocity benchmark: 67th Conference and Exhibition, EAGE, Extended Abstracts, B035.

Biondi, B. and P. Sava, 1999, Wave-equation migration velocity analysis: 69th Annual International Meeting, SEG, Expanded Abstracts, **18**, 17231726.

Biondi, B. and W. W. Symes, 2004, Angle-domain common image gathers for migration velocity analysis by wavefield continuation imaging: GEOPHYSICS, **69**, 12831298.

Biondi, B. and T. Tisserant, 2004, 3D angle-domain common-image gathers for migration velocity analysis: Geophysical Prospecting, **52**, 575–591.

Biondi, B. L., 2006, 3-D seismic imaging.

Brzostowski, M. A. and G. A. McMechan, 1992, 3-D tomographic imaging of near-surface seismic velocity and attenuation: Geophysics, **57**, 396–403.

Cavalca, M., R. P. Fletcher, and M. Riedel, 2013, Q-compensation in complex media – ray-based and wavefield extrapolation approaches: 83rd Annual International Meeting, SEG, Expanded Abstracts, 3831–3835.

Clapp, R. G. and B. Biondi, 2000, Tau domain migration velocity analysis using angle crp gathers and geologic constraints: 70th Annual International Meeting, SEG, Expanded Abstracts, **19**, 926929.

Clarebout, J. and S. Fomel, 2014, Geophysical image estimation by example.

Clark, R. A., P. M. Benson, A. J. Carter, and C. A. G. Moreno, 2009, Anisotropic P-wave attenuation measured from a multi-azimuth surface seismic reflection survey: Geophysical Prospecting, **57**, 835–845.

Clark, R. A., A. J. Carter, P. C. Nevill, and P. M. Benson, 2001, Attenuation measurements from surface seismic data Azimuthal variation and time-lapse case studies: 63rd Conference and Technical Exhibition, EAGE, Extended Abstracts, L–28.

Dasgupta, R. and R. A. Clark, 1998, Estimation of Q from surface seismic reflection data: Geophysics, **63**, 2120–2128.

Dvorkin, J., M. A. Gutierrez, and D. Grana, April 2014, Seismic reflections of rock properties: Cambridge University Press.

Dvorkin, J. and A. Nur, 1996, Elasticity of highporosity sandstones: Theory for two North Sea data sets: Geophysics, **61**, 1363–1370.

Fei, W. and P. Williamson, 2010, On the gradient artifacts in migration velocity analysis based on differential semblance optimization: 80th Annual International Meeting, SEG, Expanded Abstracts, **29**, 40714076.

Fornberg, B., 1975, On a fourier method for the integration of hyperbolic equations: SIAM Journal on Numerical Analysis, **12**, 509–528.

Futterman, W. I., 1962, Dispersive body waves: Journal of Geophysical Research, **67**, 5279–5291.

Gabor, D., 1946, Theory of communication. part 1: The analysis of information: Electrical Engineers - Part III: Radio and Communication Engineering, Journal of the Institution of, **93**, 429–441.

Gassmann, F., 1951, Uber die elastizitat poroser medien: Vierteljahrsschrift der Naturforschenden Gesellschaft in Zrich, **96**, 1–23.

Gazdag, J. and P. Sguazzero, 1984, Migration of seismic data by phase shift plus interpolation: GEOPHYSICS, **49**, 124–131.

Geertsma, J. and D. C. Smit, 1961, Some aspects of elastics wave propagation in fluid-saturated porous solids: Geophysics, **26(2)**, 169–181.

Gottlieb, D. and S. Orszag, 1977, Numerical analysis of spectral methods: Society for Industrial and Applied Mathematics.

He, Y. and J. Cai, 2012, Q tomography towards true amplitude image and improve sub-karst image: **521**, 1–5.

Israeli, M. and S. A. Orszag, 1981, Approximation of radiation boundary conditions: Journal of Computational Physics, **41**.

Kessinger, W., 1992, Extended split-step fourier migration: 62nd Annual Internat. Mtg., Society of Exploration Geophysicists, Expanded Abstracts, 917–920.

Kjartansson, E., 1979, Constant Q wave propagation and attenuation: Journal of

Geophysical Research, **84**, 4737–4748.

Kolsky, H., 1953, Stress waves in solids: Oxford, Clarendon.

Kreiss, H.-o. and J. Oliger, 1972, Comparison of accurate methods for the integration of hyperbolic equations: Tellus, **24**, 199–215.

Leaney, W. S., 1999, Walkaway Q inversion: 69th Annual International Meeting, SEG, Expanded Abstracts, 1311–1314.

Leggett, M., N. R. Goulty, and J. E. Kragh, 1992, Study of traveltime and amplitude time-lapse tomography using physical model data: Abstracts of 54th EAEG Meeting, 248–249.

Li, Y., Y. Shen, and P. Kang, 2015, Integration of seismic and fluid-flow data: a two-way road linked by rock physics: EAGE – 77th EAGE Conference and Exhibition.

Macrides, C. G. and E. R. Kanasewich, 1987, Seismic attenuation and Poisson's ratios in oil sands from crosshole measurements: Journal of the Canadian Society of Exploration Geophysicists, **23**, 46–55.

Mateeva, A., 2003, Thin horizontal layering as a stratigraphic filter in absorption estimation and seismic deconvolution: PhD thesis, Colorado School of Mines.

Maultzsch, S., M. Chapman, E. Liu, and X. Y. Li, 2007, Modelling and analysis of attenuation anisotropy in multi-azimuth VSP data from the clair field: Geophysical Prospecting, **55**, 627–642.

Mavko, G., C. Chan, and T. Mukerji, 1995, Fluid substitution: Estimating changes in VP without knowing VS: GEOPHYSICS, **60**, 1750–1755.

Mavko, G., T. Mukerji, and J. Dvorkin, 2009, The rock physics handbook: Cambridge University Press.

McDonal, F. J., F. A. Angona, R. L. Mills, R. L. Sengbush, R. G. VAN Nostrand, and J. E. White, 1958, Attenuation of shear and compressional waves in pierre shale: Geophysical Prospecting, **6**, 404–407.

Muller, T. M., B. Gurevich, and M. Lebedev, 2010, Seismic wave attenuation and dispersion resulting from wave-induced flow in porous rocks  A review: Geophysics, **75**, A147–A164.

Orszag, S. A., 1972, Comparison of pseudospectral and spectral approximation: Studies in Applied Mathematics, **51**, 253–259.

Plessix, R. E., 2006, Estimation of velocity and attenuation coefficient maps from crosswell seismic data: Geophysics, **71**, S235–S240.

Polak, E., R. G., 1969, Note sur la convergence de mthodes de directions conjugues:

ESAIM: Mathematical Modelling and Numerical Analysis - Modlisation Mathmatique et Analyse Numrique, **3**, 35–43.

Quan, Y. and J. M. Harris, 1997, Seismic attenuation tomography using the frequency shift method: Geophysics, **62**, 895–905.

Raymer, L. L., E. R. Hunt, and J. S. Gardner, 1980, An improved sonic transit time-to-porosity transform: Society of Petrophysicists and Well-Log Analysts, **January**, no. 1.

Reine, C., R. A. Clark, and M. van der Baan, 2012a, Robust prestack Q-determination using surface seismic data: Part 1 Method and synthetic examples: Geophysics, **77**, R45–R56.

———, 2012b, Robust prestack Q-determination using surface seismic data: Part 2 3D case study: Geophysics, **77**, B1–B10.

Rickett, J., 2006, Integrated estimation of interval-attenuation profiles: Geophysics, **71**, A19–A23.

———, 2007, Estimating attenuation and the relative information content of amplitude and phase spectra: Geophysics, **72**, R19–R27.

Ristow, D. and T. Ruhl, 1994, Fourier finite difference migration: GEOPHYSICS, **59**, 1882–1893.

Sava, P. and B. Biondi, 2004, Wave-equation migration velocity analysis-i: Theory: Geophysical Prospecting, **52**, 593606.

Sava, P., B. Biondi, and S. Fomel, 2005, Amplitude-preserved common image gathers by wave-equation migration, 296–299.

Sava, P. C. and S. Fomel, 2003, Angle-domain common-image gathers by wavefield continuation methods: Geophysics, **68**, 1065–1074.

Shen, P., W. W. Symes, and C. C. Stolk, 2003, Differential semblance velocity analysis by wave-equation migration: SEG Technical Program Expanded Abstracts 2013, 21322135.

Shen, P., W. W. S. S. M. A. H. and H. Calandra, 2005, Differential semblance velocity analysis via shot profile migration: 75th Annual International Meeting, SEG, Expanded Abstracts, **24**, 22492252.

Shen, Y., B. Biondi, and R. Clapp, 2015, Wave-equation based Q tomography from angle-domain common image gathers, 4334–4338.

Shen, Y., B. Biondi, R. Clapp, and D. Nichols, 2013, Wave-equation migration Q analysis (WEMQA): EAGE Workshop on Seismic Attenuation Extended Abstract.

———, 2014, Wave-equation migration Q analysis (WEMQA): SEG Technical Program Expanded Abstracts.

Shen, Y. and J. Dvorkin, 2015, Using rock physics to improve qp quantification in seismic data, abstract S23B–2698.

———, 2016, Using rock physics to improve qp quantification in seismic data, 3895–3899.

Shen*, Y., C. Willacy, and V. Goh, 2015, Image-based Q tomography using wavefield continuation in the presence of strong attenuation anomalies: A case study in gulf of mexico.

Shen, Y. and T. Zhu, 2015, Image-based Q tomography using reverse time Q migration, 3694–3698.

Soubaras, R. and B. Gratacos, 2004, Velocity model building by semblance maximization of modulated-shot gathers: GEOPHYSICS, **72**, U67U73.

Stoffa, P. L., J. T. Fokkema, R. M. de Luna Freire, and W. P. Kessinger, 1990, Splitstep fourier migration: GEOPHYSICS, **55**, 410–421.

Symes, W. W. and J. J. Carazzone, 1991, Velocity inversion by differential semblance optimization: GEOPHYSICS, **50**, 654663.

Tang, Y., 2011, Imaging and velocity analysis by target-oriented wavefield inversion: PhD thesis, PhD thesis, Stanford University.

Tonn, R., 1991, The determination of seismic quality factor Q from VSP data: A comparison of different computational techniques: Geophysical Prospecting, **45**, 87–109.

Valenciano, A. A., N. Chemingui, D. Whitmore, and S. Brandsberg-Dahl, 2011, Wave equation migration with attenuation and anisotropy compensation: 2011 Annual Meeting, SEG, Expanded Abstracts, 232–236.

Wang, Y., S. Chen, L. Wang, and X. Li, 2013, Modeling and analysis of seismic wave dispersion based on the rock physics model: J. Geophys. Eng., **10**.

Winkler, K. W. and A. Nur, 1982, Seismic attenuation: Effects of pore fluids and frictional sliding: Geophysics, **47**, 1–15.

Zener, C., 1948, Elasticity and anelasticity of metals: Chicago, IL, University of Chicago Press.

Zhang, Y. and G. Shan, 2013, Wave-equation migration velocity analysis using partial stack-power maximization, 4847–4852.

Zhou, J., X. Wu, K. H. Teng, Y. Xie, F. Lefeuvre, I. Anstey, and L. Sirgue, 2014, FWI-guided Q tomography and Q-PSDM for imaging in the presence of complex gas clouds, a case study from offshore Malaysia: **136**, 536–540.

Zhu, T. and J. Harris, 2014, Modeling acoustic wave propagation in heterogeneous attenuating media using decoupled fractional Laplacians: Geophysics, **79**, no. 3, T105–T116.

Zhu, T., J. Harris, and B. Biondi, 2014, Q-compensated reverse-time migration: Geophysics, **79**, no. 3, S77–S87.

Zucca, J. J., L. J. Hutchings, and P. W. Kasameyer, 1994, Seismic velocity and attenuation structure of the geysers geothermal field, california: Geothermics, **23**, 111–126.